UNIVERSITY OF SOUTHAMPTON

A Study of a Correlation Spectroscopy Gas Detection Method

by

Paul Chambers

A thesis submitted in partial fulfillment for the
degree of Doctor of Philosophy

in the
Faculty of Engineering, Science and Mathematics
Optoelectronics Research Centre

October 2005

UNIVERSITY OF SOUTHAMPTON

ABSTRACT

FACULTY OF ENGINEERING, SCIENCE AND MATHEMATICS
OPTOELECTRONICS RESEARCH CENTRE

Doctor of Philosophy

by Paul Chambers

The study of an optical correlation spectroscopy gas detection system is presented in this thesis. The correlation spectroscopy method uses a sample of reference gas as a filter to identify the concentration of the target gas in a measurement gas cell.

A review of optical gas sensing methods employed throughout the twentieth and early twenty-first centuries, which led to this version of correlation spectroscopy, is presented. The equation for the output signal modulation, the modulation index, is derived. The method of correlation spectroscopy is analysed by simplified approximation, which aids the understanding of the method.

The study primarily relates to the detection of CO_2 gas. The 2000 edition of the Hitran database was used to provide spectroscopic absorption data for a series of simulations of the correlation spectroscopy method. The simulations show the dependence of the modulation index on measurement cell target gas concentration, measurement cell target gas pressure and measurement cell target gas temperature. Experiments were carried out to assess the correlation spectroscopy method. These experiments used a large-core optical fibre implementation of a correlation spectroscopy detection system with LED infra-red optical sources. A comparison of simulated and experimental results is given. At gas cell pressures of 1 bar the experimental data and the simulated data were found to agree to within 15%. Simulated results for the detection of CH_4 and O_2 are also presented.

A method of increasing the output modulation index by the pressurisation of a CO_2 containing reference gas cell was also investigated by simulation and experiment. It was found by experiment and simulation, that by the pressurisation of the reference gas cell to 6 bar, the modulation index could by increased by up to a factor of 2. However, it was shown that the cross-sensitivity to a contaminant gas also increased.

Keywords: correlation spectroscopy, gas filter correlation, gas detection, infra-red gas detection, optical fibre sensor, carbon dioxide, methane, oxygen.

Acknowledgements

I would like to acknowledge and sincerely thank the following:

- Professor John P. Dakin, who supervised this project, for his guidance and assistance in relation to the thesis and related publications.
- Dr. Ed A. D. Austin for collaborating on the production of publications and having constructed some of the experimental apparatus.
- Dr. Trevor P. Newson for his help and encouragement, and for having made many helpful observations about correlation spectroscopy.
- Dr. Eleanor J. Tarbox for having made many useful suggestions during the preparation of this thesis.
- Professor Harvey N. Rutt for pointing me in the right direction to find some early examples of correlation spectroscopy gas detection systems.
- Professor Peter G. R. Smith for his assistance at an early stage in the project.
- Friends and colleagues in the Optoelectronics Research Centre for their assistance and encouragement in many ways throughout my studies.
- My parents for their unwavering support.
- The EPSRC for the student bursary which supported me during my studies.
- The industrial consortium (B.O.C. Edwards, N.P.L., Kidde plc., Health and Safety Laboratory, National Grid Transco, Sira and Accurate Controls Ltd.) which provided funding for equipment during this work.

Declaration of Authorship

I, **Paul Chambers**, declare that the thesis entitled:

"A Study of a Correlation Spectroscopy Gas Detection Method"

and the work presented in it, are my own.

I confirm that:

- this work was done wholly or mainly while in candidature for a research degree at this University;
- where any part of this thesis has previously been submitted for a degree or any other qualification at this University or any other institution, this has been clearly stated;
- where I have consulted the published work of others, this is always clearly attributed;
- where I have quoted from the work of others, the source is always given. With the exception of such quotations, this thesis is entirely my own work;
- I have acknowledged all main sources of help;
- where the thesis is based on work done by myself jointly with others, I have made clear exactly what was done by others and what I have contributed myself;
- parts of this work have been published in the publications listed in Appendix B.

Signed: Paul Chambers

Date: 17/10/2005

Contents

Chapter 1

Introduction

Gas sensors are used in several areas of everyday life, for example there are environmental, industrial and medical applications in addition to applications in health and safety. This thesis examines the operation of a particular method of gas detection using optical correlation spectroscopy and shows with what accuracy the response of the system may be predicted with available spectral gas absorption data. The discussion is comprised of six principal chapters and the contents of each of these is summarised below.

There are many optical and non-optical methods of detecting gases. In Chapter 2 a historical review of the development of optical gas sensing systems is presented, including a review of gas sensing systems that are currently in use. The area of optical gas detection methods is discussed in more detail and this includes a review of gas detection methods that were developed during the twentieth and early twenty-first centuries. Methods utilising the photoacoustic effect are described followed by an account of methods that were developed with the advent of semiconductor optical detection technology.

In Chapter 3 the fundamentals of the operation of the correlation spectroscopy system studied in this thesis are described. The mathematical derivation for what is considered the prime signal output, the modulation index, is given and its behaviour is presented using a simplified model of a gas absorption spectrum. Later in this thesis, where appropriate, simulated and experimental findings are compared with these basic results.

A description of the Hitran database, which is a compilation of gas absorption data, and how the data are derived from it is presented in Chapter 4. A review of the physical phenomena that cause the infrared absorption of gases in the infrared is included. The effects on the gas spectra that temperature and pressure changes in the gas cells would be expected to have on the transmission spectra of the gas cells are graphically shown and described. Also, the transmission data for CO_2 at around 2 μm is compared to an experimentally observed transmission spectrum.

The simulated response of a correlation spectroscopy system is presented in Chapter 5. The gas chosen to demonstrate this response is carbon dioxide (CO_2) at spectral wavelengths of approximately 2 μm. The simulations show the consequences of the selection of system components and the expected correlation spectroscopy system response to CO_2. The simulated effects of temperature changes and pressure changes on the derived system measurement are presented and the response of the system to the introduction of a contaminant gas (water vapour) is also discussed. A method of increasing the system's signal response by using pressurised reference gas cells is explored by simulation, and its potential advantages and disadvantages are considered. Simulated results for the detection of methane gas (CH_4) at spectral wavelengths around 1.6 μm and oxygen gas (O_2) at around 0.760 μm are also presented and differences between these and the simulated response obtained for the detection of CO_2 are highlighted.

Experiments carried out to verify the mode of operation of a correlation spectroscopy system are described in Chapter 6. CO_2 was chosen as the gas to be experimentally investigated. These experiments sought to verify some of the results found by simulation, including the response of the correlation spectroscopy system to various concentrations of CO_2 in the measurement gas cell, the effects of pressure and temperature changes in the measurement gas cell and the response of the system to a contaminant gas (H_2O). Results from experiments describing the effect of increasing the pressure of the reference gas cell on the system output are also described and compared to the simulated response.

In Chapter 7 the system performance is analysed from a theoretical and experimental perspective. This includes an analysis of the losses that were experienced and an evaluation of the noise sources in the system. A method of increasing the path-length of the gas cells is described and the experimental results that were obtained are shown.

Chapter 8 discusses the conclusions that can be reached as a result of the work presented in this thesis, and Chapter 9 outlines areas of potential future work that could be undertaken.

There are two appendices to this thesis. Appendix A describes an analysis of the variation of the emission of radiation from a LED (Light Emitting Diode) with temperature, and Appendix B contains a list of the publications that have resulted from the content of this thesis.

Chapter 2

Background

2.1 Introduction

This chapter reviews the development of optical gas sensors, with an emphasis on remote sensing optical-fibre techniques and concludes with an account of selective methods using correlation spectroscopy techniques.

Gas sensors are of importance for a variety of environmental, industrial, medical, scientific and domestic applications. The gas may be, for example, hazardous to human health, an atmospheric pollutant, or of importance, in terms of its concentration, for an industrial or medical process. Apart from systems providing an alarm signal, it is frequently required to obtain accurate real-time measurements of the partial pressure of a particular (target) gas, often in a mixture of other gases.

There are several methods of gas detection that may be applicable to different situations. For example methods relying on mass spectrometry, which compares the mass to electronic charge of a molecule, tends to be used where a very accurate measurement of concentrations of a wide variety of gas species is required. Other methods, such as those that utilise the chemical reaction of a gas with a material or the combustibility of a gas (e.g. a Pellistor gas sensor) tend to find more specific applications, e.g. the monitoring of exhaust emissions or the build-up of specified harmful gases. Optical non-dispersive infrared methods can detect most gas compounds with infrared absorption or emission, often with high sensitivity. The advantages and disadvantages of a variety of methods, including those discussed above, is presented in Table 2.1.

Method	Advantages	Disadvantages
Optical spectroscopy: measurement of optical absorption, emission or scattering.	Offers a direct and rapid, and often highly selective, means of measuring gas concentration.	The gas must have a significant and distinct absorption, emission or scattering in a convenient region of the optical spectrum.
Mass spectrometry.	Very accurate and highly selective means of detecting concentrations of gas including isotope abundance, etc.	Slowly acting, bulky and comparatively expensive. Not easy to use for on-line in situ measurements, as gas sampling necessary.
Gas chromatography.	Very accurate and highly selective means of detecting concentration.	Not easy to use on-line, as gas sampling necessary.
Interaction with a chemical indicator.	Can measure total exposure over time (dosimetry), if a non-reversible reaction is used.	The sensor may be poisoned and/or fouled. May exhibit non-reversible behaviour, which, in many cases, may be undesirable. May need water vapour present, to act as a catalyst, if "dry" reaction is too slow.
Sensors involving interaction with the surface of a semiconductor, or ceramic layer, e.g.CHEMFETS and other electrochemical sensors.	Low cost. Can measure total exposure over time, if a non-reversible reaction is used.	Poisoning can occur. May exhibit non-reversible behaviour, which may be undesirable. May consume analyte.
Catalytically induced combustion and measurement of the heat change (Pellistor gas sensors) [1, 2].	Low cost and practical means of detecting presence of flammable gases.	Poisoning can occur. If other flammable gas is present, may give reading which is not predictably related to the lower explosive limit (LEL).

TABLE 2.1: Summary of Advantages and Disadvantages of Gas Detection Methods.

Optical methods monitor the optical absorption/emission/scattering of a gas species at defined optical wavelengths. The distribution of this optical absorption/emission with wavelength provides an optical identification marker of any specific gas species present, and the magnitude of the optical absorption/emission typically shows the concentration.

Spectroscopic optical methods provide a fast, accurate and stable measurement of a gas species, provided that it has significant absorption or emission of optical radiation in a suitable wavelength band. The simplest diode laser absorption methods usually involve probing at one wavelength where absorption occurs, and also at a wavelength chosen to be essentially free of any absorption by the target gas (and preferably not absorbed by any likely contaminant, since then referencing errors could occur). A comparison of the received powers from these wavelengths allows the target gas concentration to be estimated [3].

The spectroscopic sensing of chemical species has a history dating back to the invention of the photophone and the recording of optical spectra. Most analytical chemistry laboratories possess at least one spectrophotometer for the recognition of a wide range of chemical species, based on their characteristic absorption, fluorescence or Raman-scattering spectra. Normally optical gas sensing methods use more dedicated versions of such spectrometers, which can be used to interrogate remote sensing heads with the use of fibre optic extension leads.

There are many remote free-space laser methods such as FMS (Frequency Modulation Spectroscopy)[4] and LIDAR (LIght Detection And Ranging). One of the most useful is DIAL (DIfferential Absorption LIDAR), where a dual-wavelength laser pulse is directed into the atmosphere and the time-varying back-scattered signatures from light at each of the two wavelengths are compared in order to determine the differential absorption as a function of distance along the path. A non-linear method called CARS (Coherent Anti-Stokes Raman Scattering) has also been used. These methods, and also several other more complex alternatives using multi-photon processes, are not commonly used with optical fibres. This free-space technique has found application in several areas of environmental monitoring, including geothermal emission monitoring [5]. A complete description of these is beyond the scope of this thesis.

2.2 Gas Detection Techniques

Early optical gas analysers relied upon the photoacoustic properties of gases, at the time this was referred to as the "Tyndall-Röntgen effect". The "Tyndall-Röntgen effect" in gases is analogous to the "Bell effect", which is the development of an audible sound arising from the intermittent exposure of a solid or liquid to radiation. Early gas sensing systems that utilised the photoacoustic effect were developed before, during and since World War II, in Britain, the U.S.S.R. and Germany. An example of an early gas

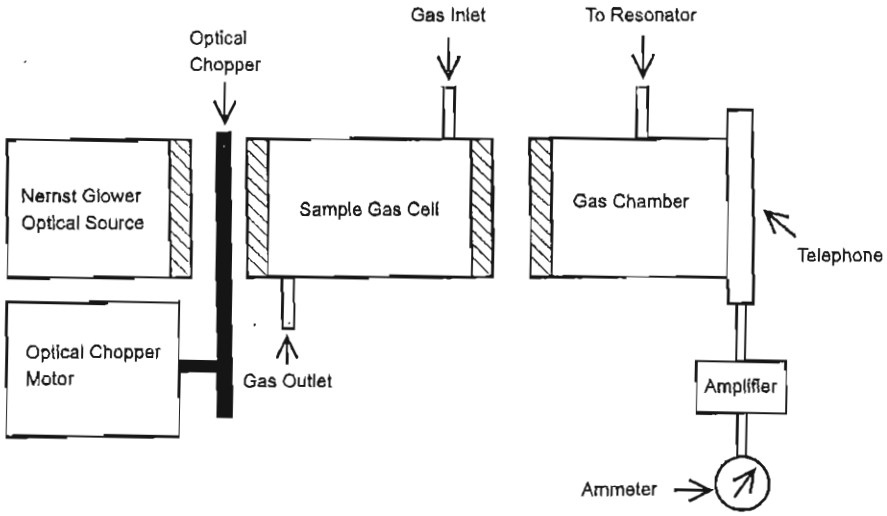

FIGURE 2.1: An early "optico-acoustic" gas detection arrangement due to Vengerov (see references [6, 7])

detection method due to Veingerov (1938), which is described by Hill and Powell in [6], is shown in Figure 2.1. The gas analyser, which was named an "optico-accoustic" analyser, operated by passing intensity modulated optical radiation from a Nernst Glower Source through a highly polished tube to a telephone receiver. The pressure variations induced by the intermittent optical beams resulted in a differing expansion of the gases present in the sample gas cell. This, in turn, induced the generation of acoustic tones that were picked up by the telephone earpiece (microphone). These tones were indicative of the gases present in the sample gas cell. The branch-resonator enabled the pressure fluctuations developed to be amplified, so that the detected signal could be enhanced.

Concurrently with the work by Veingerov, Luft developed a null-balance arrangement in 1946 (see Hill and Powell [6]). This, and systems developed from it, were later referred to as LIRA (Luft Infra-Red Analyser [8]) type analysers, an example of which is shown in Figure 2.2.

The systems operated by passing two alternately chopped optical beams through a reference gas cell and a sample or measurement gas cell to a detector. Initially the devise was "null-balanced" by filling both the reference and sample cells with a gas that had no absorption lines in the spectrum of interest and equalising the intensity of the optical beams by adjusting a blocking trimmer screw. The insertion of the sample gas into the sample or measurement cell leads to a signal modulation at the detector which is proportional to the target gas concentration in the sample gas. It was found that, by the insertion of a reference gas cell in series with the measurement gas cell, the selectivity of the system to the target gas could be improved. The LIRA system was able to detect CO_2 concentrations of less than 10 parts per million (ppm).

Hill and Powell [6] also described the development of early gas analysers that were manufactured during the 1950s and 1960s and the development of early infra-red detectors.

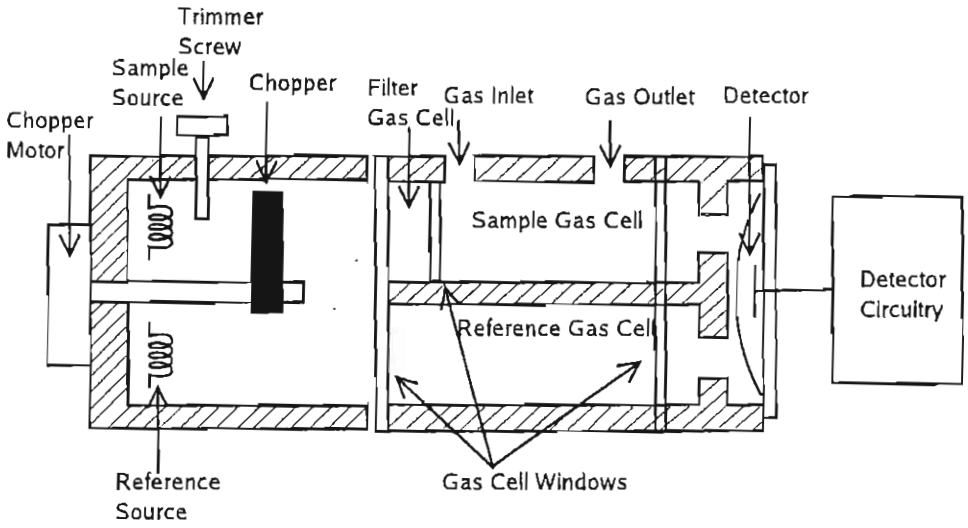

FIGURE 2.2: A Null-Balance Lira (Luft Infra-Red Gas Analyser) gas detection system [6].

A paper published by Goody [9] in 1968 explored the possibility of selectively detecting a specified target gas by a correlation spectroscopy technique. Goody introduced a pressure modulated "cross-correlating spectrometer", a device which involved passing light from an optical source through two sequential gas cells and an optical filter, before impinging on an optical detector, see Figure 2.3. The first gas cell contained the gas volume to be analysed (the measurement cell) and the second contained only the target

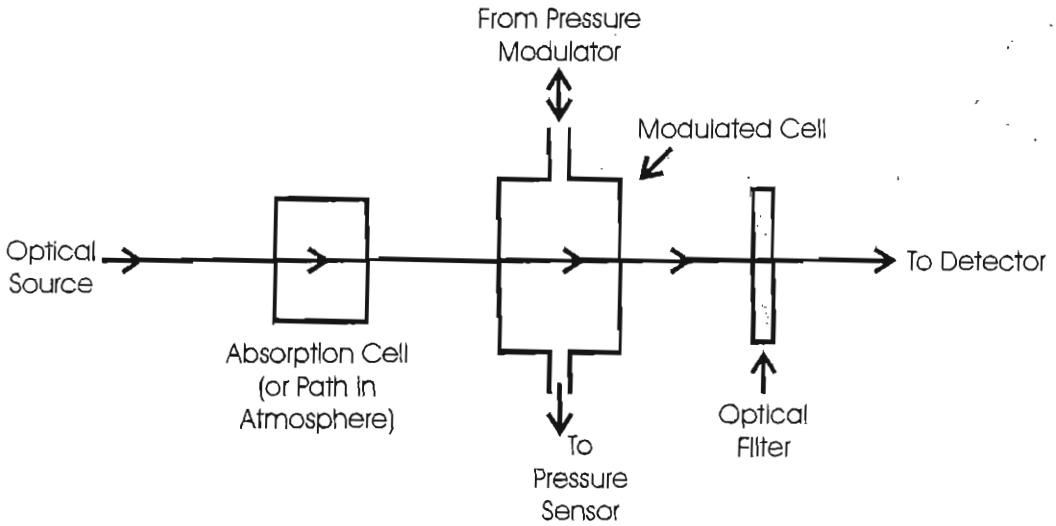

FIGURE 2.3: Pressure Modulation Spectroscopy system (reproduced from Goody [9]).

gas (the reference cell). By modulation of the target gas pressure within the reference gas cell, a modulation of the detected optical power at the output of the measurement gas cell was observed. This magnitude of the output modulation was related to the concentration of target gas within the measurement gas cell. The method showed high rejection of drifts in source power and had high rejection of contaminant gas. A NH_3

sensor based on this method was found to be 140 times less sensitive to N_2O contaminant gas, even though the spectral absorption of N_2O is significantly stronger than the spectral absorption of NH_3 in the band used.

In 1972, Taylor *et al.* [10] published details of a similar system, intended to measure remotely (from a satellite) the temperature of the upper atmosphere from the spectral transmission of CO_2. The system gathered light reflected from the earths atmosphere, and passed it though a pressure modulated reference gas cell to a detector. Their system showed a sensitivity of 1°C. This method utilised the spectral emission of CO_2 at 15 μm.

Another reported method of modulating the transmission of the reference cell was that of Stark modulation. This is the line-splitting effect that results when a high electric field is applied to a gas. It is only effective on molecules having a significant dipole moment, e.g. H_2O, CH_4 etc. Edwards and Dakin [11] investigated the use of Stark modulation for the detection of ammonia and water vapour, both of industrial significance, using optical fibre-based systems. This system demonstrated the use of optical fibres for gas detection, an area which is now discussed in detail.

2.3 Optical Fibre Implementations

Optical detection systems using optical fibres offer a number of advantages over bulk optical sensing systems. The principal advantage is that a robust passive sensing head may be sited remotely from the monitoring station, which is a useful feature in severe environments. This also allows for the development of multiplexed networked systems, where a single interrogation unit can monitor many low-cost passive sensing heads via a predictable propagation medium (i.e. the optical fibre). Conventional silica fibres have the disadvantage that transmission is restricted to the visible and near-infra-red region (0.6 μm to 2.0 μm). Fluoride and other fibres may be used to extend the operation of these sensors further into the infra-red, allowing accurate detection of gases with infra-red absorption in the mid- and far-infra-red. Unfortunately, these fibres are expensive and less robust. Optical fibre sensors are also generally believed to be safe for use in explosive atmospheres. However, the safety of optical fibre sensors is not unqualified, as it has been established that in the case of very high powers, i.e. of the order of 100 mW, or greater in multi-mode fibre, explosive risks may present themselves [12, 13]. Conventional optical fibres have a very small acceptance aperture, which severely restricts the amount of light that can be coupled into a fibre. Thus the power launched into optical fibres from high-radiance near-infra-red (NIR, $\sim$0.7 μm-$\sim$1.5 μm) Light Emitting Diodes (LEDs) is rarely above 1mW, even when large core optical fibres are used, and by comparison the spectral radiance of incandescent filament lamps is usually at least an order of magnitude less. Longer wavelength LEDs ($>\sim$1.5 μm) often have a lower spectral radiance. As the launched power is relatively low, sensitive light detection systems

are required to produce operational sensors. With laser sources, there is no difficulty in achieving launch efficiencies in excess of 80% into multi-mode fibres. Consequently high powers can be launched, and the detection system constraints are eased substantially.

It was realised that narrow-linewidth diode lasers could readily be used in fibre-optic environmental detection systems. Inaba *et al.* [14] suggested the use of a dual-wavelength laser to realise a differential absorption method that could be used over many kilometres of low-loss optical fibre in cases where it was necessary to locate the sensing head remotely from the measuring equipment. This typically involved the comparison of the received powers at two, or more, different wavelengths, each having passed through a remote measurement gas cell, so that the differential absorption of the two wavelengths by the gas sample could be used to infer the concentration of the target gas. The method required that the target gas possessed suitable gas absorption bands within the spectral transmission window of the optical fibre.

Culshaw *et al.* [15] have surveyed some of the system topologies that may be used with laser-based optical gas detection systems and quantified the expected system sensitivities, which are of the order of less than 1 ppm. Stewart *et al.* [16] and Whitenett *et al.* [17] have realised some of these topologies, which included a Distributed FeedBack (DFB) wavelength modulated laser cavity ring-down approach that showed a methane detection sensitivity of 50 ppm.

A laser-based detection system for the detection of NO_2 gas (which is an industrial hazard and common environmental pollutant) was developed by Koybayashi *et al.* [18]. This was achieved by splitting light, from an Ar-ion multi-line laser, into two paths, one passing through a measurement gas, and the other being transmitted directly to the measurement unit as a reference signal. The detection unit contained two filters to separate the two chosen laser lines, and these were then detected on separate optical receivers. One of these chosen laser lines coincided with a strong absorption line in the NO_2 absorption spectrum, whilst the other absorption line was somewhat weaker, hence giving a differential absorption method, by which the concentration of NO_2 in the measurement cell could be found. The system had an estimated detection limit of 17 ppm. The advantages of this dual-wavelength system were that the measurement was dependent on neither the optical power spectrum from a single source, which could drift, nor the system transmission, which could be affected by optical alignment, surface contamination, etc. It was realised that the selection of light sources used in this type of detection system was not necessarily limited to lasers, but broad-band sources such as filtered incandescent lamps or LEDs could also be used.

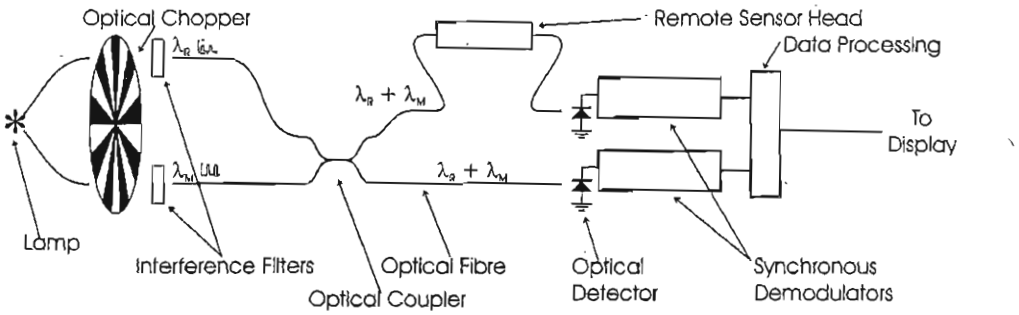

FIGURE 2.4: Schematic of a differential fibre-optic detection system (redrawn from a diagram in Hordvik *et al.* [19]).

Hordvik *et al.* [19] developed a fibre-optic system for the remote detection of methane gas (CH_4), see Figure 2.4. This system used a halogen lamp light source, which was alternately chopped into two separately filtered paths. One path was passed through a narrow-band interference filter, centred at the same wavelength as a strong absorption band of CH_4 (Q-branch centred at 1.666 μm), whilst the other filter covered a broader spectral range, and consequently had lower average absorption. These two complementary-modulated beams were combined by means of a fibre-coupler, with two output ports. Light from one was passed through a measurement cell to an optical detector (the measurement signal), and light from the other was passed directly to an optical detector (reference signal). By comparison of the optical powers in the narrow-band and broadband beams of the light that had and had not passed through the measurement cell, it was possible to calculate the CH_4 concentration.

A somewhat similar system based on the use of optical fibres and optical fibre couplers, but with the innovative use of compact LED light sources, was developed by Stueflotten *et al.* [20]. The schematic of the system is shown in Figure 2.5. Again, two different optical filter wavelengths were used, to give differential attenuation in strong and weak gas absorption regions. This was proposed for remote measurement in hazardous industrial environments, such as off-shore oil platforms. The systems above developed by Hordvik and Stueflotten both had a reported detection limit of approximately 5000 ppm (0.5% vol/vol).

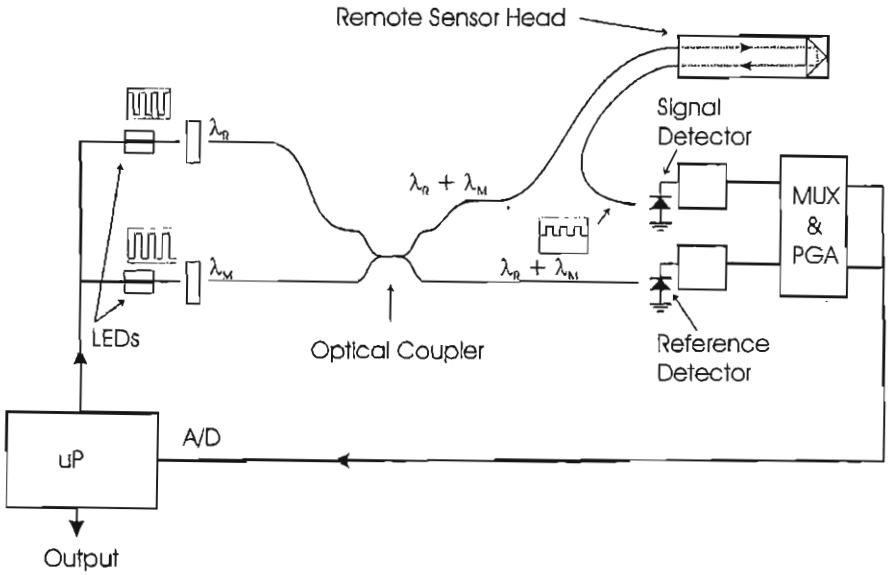

FIGURE 2.5: Schematic of the differential fibre-optic detection system (redrawn from a diagram of Stueflotten *et al.* [20]).

2.4 Sensing using Inelastic Processes

Other forms of spectrophotometric processes rely on Raman scattering. A Raman scattering gas detection method is now briefly reviewed before the principal subject of this thesis, correlation spectroscopy, is described in detail.

Raman scattering involves the inelastic scattering of light, i.e. first absorption and then delayed re-emission of light at a different wavelength to that incident on the material. The Raman process represents a form of scattering in which an incident photon may gain energy from (the anti-Stokes Raman process), or donate energy to (the Stokes Raman process) a vibrational or rotational energy level in a material. This produces a re-emitted photon of different energy and, hence, of a different wavelength. A method of detection that exploits Raman spectroscopy was developed by Samson and Stuart [21] using the detection system shown in Figure 2.6. Raman scattering in gases is generally very weak, but the emission usually occurs in a well defined spectrum.

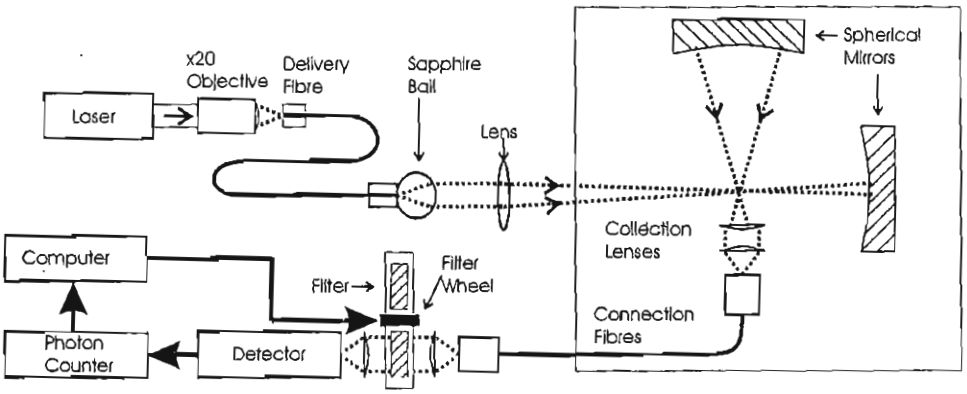

FIGURE 2.6: Schematic of a gas sensor using Raman Scattering (Redrawn from Samson and Stuart [21]).

In the system developed by Samson and Stuart, the laser excites the gas and a mirror is used to reflect the incident light back through the interaction zone. Another concave mirror reflector doubles the level of Raman light received by the collection lenses. The alternative inelastic scattering process of fluorescence is rare in gases, and consequently is not commonly used for optical gas sensors, but fluorescence cannot be ignored when using Raman sensing, as it can cause crosstalk if it occurs in optical glass components or at mirror surfaces. Fortunately, Raman lines for simple gases are narrow compared to fluorescence emission which is usually relatively broadband.

2.4.1 Comb Filter Modulator for Partially Matching Several Spectral Lines

Instead of detecting a gas using a single line of its absorption spectrum, or using a broadband source to cover many absorption lines, there are advantages in using some form of optical "comb" filter, with several periodic narrow transmission windows, in order to match several spectral lines simultaneously. Such a comb filter can be scanned, or correlated, through a set of gas lines to give an intensity modulation. The method has the advantage that it may allow improved selectivity, as a synthetic multiple-narrow-line comb-filter spectrum allows simultaneous measurement on several spectral lines. This reduces interference effects, which can cause complications with laser sources. A method of doing this, with a scanned Fabry-Perot comb filter, has been demonstrated [22, 23] with application to methane detection. Dakin *et al.* implemented a system that passed light sequentially from a source through a Fabry-Perot interferometer to a detector. By changing the spacing of the plates of the interferometer the transmission of fringes of the interferometer were tuned to match the absorption spectrum of the methane target gas. Dakin *et al.* reported a sensitivity limit of 100 ppm [22]. The disadvantage of the Fabry-Perot filter is that it has a regular frequency spacing, whereas the gas absorption features are not normally equally spaced. A variation of the method is to use the correlation

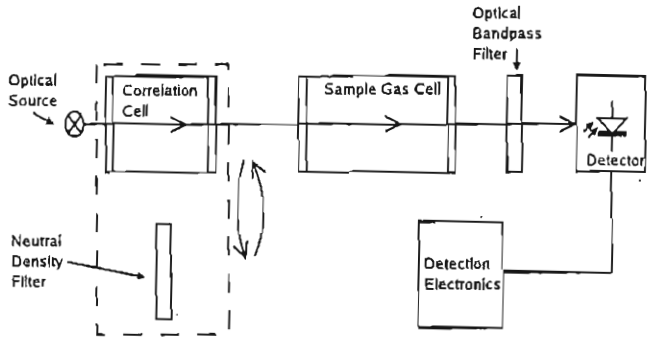

FIGURE 2.7: Schematic of a Gas Filter Correlation (GFC) System due to Herget [26].

spectroscopy complementary source modulation technique with a filter that replicates the gas transmission spectrum.

The Complementary Source Modulation (CoSM) version of correlation spectroscopy is discussed and analysed in the remainder of this thesis.

2.5 The CoSM Method of Correlation Spectroscopy

Optical absorption based correlation spectroscopy is a means of selectively detecting, or "fingerprinting", gases. In optical correlation spectroscopy methods of gas detection, most or all of the usefully attainable spectral features of a target gas, e.g. its absorption or emission spectrum, are compared with a similar reference spectrum. This reference might be an optical filter that can extract certain features of a gas absorption spectrum (examples include the Fabry-Perot method discussed above and synthetic optical filter designs that replicate a gas absorption spectrum [24, 25]), or a sample of the gas itself that can be compared to the transmission spectrum of the target gas. In this way, the concentration of a target gas may be inferred with a defined cross sensitivity to other gases.

Herget *et al.* [26] reported a system known as Gas Filter Correlation (GFC). They demonstrated the applicability of the technique to the on-site detection of atmospheric pollutants in the stacks of industrial plants. A schematic of the method used is shown in Figure 2.7. The optical power passed from an optical source, through a reference gas cell (or "correlation cell"), sequentially followed by a sample gas cell and then the power, filtered by an optical bandpass filter, was incident upon a detector. The reference or correlation gas cell was alternately exchanged with a neutral density filter. The neutral density filter was chosen, so that when the measurement or sample gas cell contained a gas that did not possess any gas absorption lines in the pass-band of the optical bandpass filter, no signal modulation was observed when the neutral density filter and the reference gas cell were interchanged. Then traces of the target gas in the sample gas cell would reintroduce a signal modulation, the magnitude of which was indicative

of the target gas concentration in the sample gas cell. Herget *et al.* observed that when a contaminant gas was introduced into the measurement gas cell a measurement signal was observed that was of the opposite polarity to that which would be seen when the target gas was present in the measurement gas cell.

A system, results from which were published by Kebabian *et al.* in 2000, substituted two alternately switched LEDs, one coupled to a reference gas cell, and the other to a compensating neutral density filter, for the optical source and the arrangement in the Herget system, whereby a reference gas cell was interchanged with a neutral density filter. The output of the reference gas cell and the neutral density filter were coupled into single-mode optical fibres. The two single mode optical fibres were then combined to form one unified output. By the insertion of a second coupler in series, the received power level could be monitored and the neutral density filter adjusted, so that the intensity of the optical signal from the two alternately switched LEDs could be held temporally constant. The combined optical signal would then progress to the measurement gas cell, were if the target gas were present, a signal modulation would be introduced that was in proportion to the measurement gas cell target gas concentration. The system was demonstrated with NO_2 gas, and they claimed a detection limit of 1 ppm. Of the contaminant gases investigated, which were SO_2 and CO_2, they found that the sensor gave no response. However, they found that the system had a sensitivity of 25 ppm m to ozone.

Since the work described here was carried out, and shortly before the submission of this thesis, Cheung *et al.* reported preliminary results of an acetylene correlation spectroscopy gas detection system [27]. Like Kebabian *et al.*, Cheung *et al.* used a fibre-optic system. However, instead of using LEDs as light sources, they used the Amplified Spontaneous Emission (ASE) from the two ports of a Semiconductor Optical Amplifier (SOA). A delay element was included at one output port in order to achieve a 180° phase differential between the two signals. Hence, avoiding the requirement for two separate optical sources.

2.5.1 Advantages of Correlation Spectroscopy

The correlation spectroscopy method is a self referenced method in which the intensity of the two optical sources are compared. This forms a feed back mechanism that stabilises the system. This is advantageous because it renders the measurement immune to drifts in source power or drifts in the optical transmission of the system, which may be, for instance, caused by mechanical shock.

If the correlation spectroscopy system components are correctly selected, the method has the potential to give a selective measurement of a required contaminant gas, with a high rejection of contaminant gases.

If implemented in the NIR ($<\sim 2\ \mu m$) a correlation spectroscopy system may be implemented with standard "off the shelf" optical components. This can be an advantage if it is required to minimise costs.

Similar systems using similar principles can attain high sensitivities. For example a CO_2 GFC (Gas Filter Correlation) system, which uses optical filters, instead of a reference gas cell, and bulk optics can attain sensitivities as high as 10s of parts per billion [28].

2.5.2 Disadvantages of Correlation Spectroscopy

The principal disadvantages of the correlation spectroscopy method are that it only works effectively with gases that posses an absorption spectrum in the infrared. This limits the sensitivity to gases such as O_2 and N_2, that possess weak infrared absorption spectra.

Also, in this variant of correlation spectroscopy there is the requirement for a reference gas cell. This poses the risk that if the target gas is in itself a hazard, eg. flammable or toxic, the permanent presence of the gas, perhaps pressurised, in a reference gas cell may not be desirable.

2.6 Contribution of this Work

The comparatively recent availability of accurate gas absorption databases (Hitran, GEISA, CDSD etc.) opened up the possibility of using these databases to compute the performance of correlation spectroscopy systems. The results of these simulations can then be compared with the observed experimental system response.

This work shows how the Hitran database may be used to simulate the response of correlation spectroscopy systems at the design stage before they are prototyped. This means that correlation spectroscopy systems may be optimised for magnitude of measurement and the rejection of specified gases in a quantitative manner before assembly.

Chapter 3

Operating Principle of Correlation Spectroscopy

3.1 Introduction

In this chapter the behaviour of the correlation spectroscopy method, as introduced in the previous chapter, is discussed. This is comprised of a derivation of the equation of the output signal and a demonstration of the method with the use of a simplified approximation of a gas absorption spectrum.

3.2 Description of the Operation of the Correlation Spectroscopy Method

This correlation spectroscopy method involves the alternate on/off switching of two light sources, i.e. when one source is on the other is off, and vice versa. Light from one of the switched optical sources, S_1, is passed through a reference cell containing only the gas of interest, the target gas, consequently acquiring its characteristic absorption spectrum. This optical beam is then combined with a second switched beam, 180° out of phase to that from S_1, that is directly fed from another optical source, S_2. The source S_2 is assumed to be identical to S_1 in terms of the spectral distribution of its optical emission, but its intensity may differ. This combined optical beam, which may be optically filtered to better match the spectral absorption of the target gas, is then split into two optical beams. One of these beams is incident upon an optical detector, the reference detector. The spectral intensity of S_1 (or S_2) is adjusted so that the optical intensity of the combined beam, as seen by the reference detector, is constant as the two optical sources are alternately switched on and off. The other optical beam is passed through a measurement gas cell onto a second optical detector, the measurement

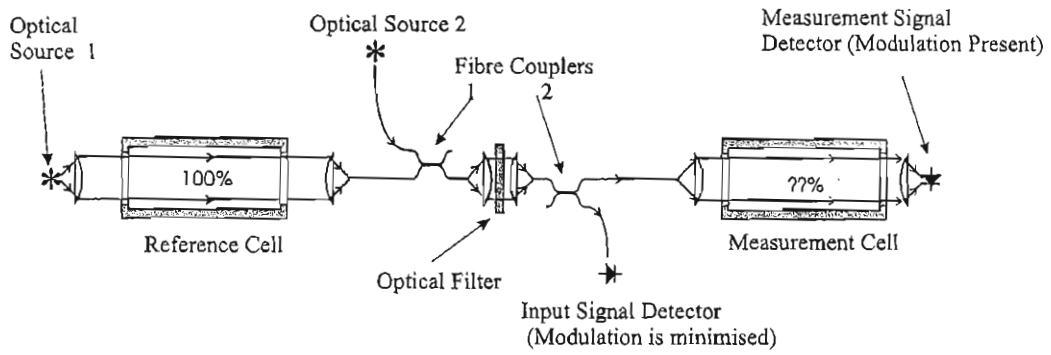

FIGURE 3.1: Schematic of a Fibre Optic Implementation of a Correlation Spectroscopy System.

detector. An estimate of the concentration of target gas present in the measurement gas cell is required. The beam component that has passed through the reference gas cell possesses a reduced amount of optical energy lying within the spectral region of the target gas absorption. The differential absorption of energy in the beams from S_1 and S_2 by the target gas in the measurement gas cell modulates the signal at the measurement detector (which was previously set constant at the reference detector by adjusting the relative strengths of sources S_1 and S_2). The frequency of the modulation is the on/off switching frequency of optical sources S_1 and S_2.

The analysis, in the remainder of this thesis, investigates the relationship between the magnitude and DC-offset of the received AC signal at the measurement detector - the modulation index - to the concentration of target gas in the measurement gas cell and the response to other parameters, such as gas pressure and temperature. The response to contaminant gas is also analysed.

The method is a self-referenced differential spectroscopic measurement approach. It is said to be *self-referenced* because the optical powers received at the reference detector from the two separate optical paths, originating from sources S_1 and S_2, are compared with each other, and *differential* because the measurement involves the comparison of optical spectral powers incident on the measurement detector from sources S_1 and S_2, via the two optical paths along which absorptions are encountered.

A schematic of a correlation spectroscopy system implemented with optical fibres is shown in Figure 3.1. The system shown could be modified by the substitution of the measurement signal detector with a retro-reflector (not shown in Figure 3.1). The output signal would then appear on the unused arm of optical coupler 2. This would effectively double the measurement cell gas interaction length. However, if a 3 dB coupler were used, the received optical power at the measurement detector would be halved.

3.3 Derivation of the Equation for Modulation Index

The modulation index of the currents arising at the measurement detector is defined as the peak to peak magnitude of the AC signal divided by the mean DC level. If $I_{(Meas,S_1)}$ and $I_{(Meas,S_2)}$ are the alternately on/off modulated signal levels due to optical sources S_1 and S_2 respectively, then the modulation index may be expressed as:

$$m = 2\left(\frac{I_{(Meas,S1)} - I_{(Meas,S2)}}{I_{(Meas,S1)} + I_{(Meas,S2)}}\right). \tag{3.1}$$

Here $I_{(Meas,S1)}$ and $I_{(Meas,S2)}$, each contributing to the photocurrent developed at the measurement detector, are defined by the equations

$$I_{(Meas,S1)} = \int S_1(\lambda)F(\lambda)T_{Ref}(\lambda)T_{Meas}(\lambda)Resp_{meas\ diode}(\lambda)d\lambda, \tag{3.2}$$

$$I_{(Meas,S2)} = \int S_2(\lambda)F(\lambda)T_{Meas}(\lambda)Resp_{meas\ diode}(\lambda)d\lambda, \tag{3.3}$$

where $S_1(\lambda)$ and $S_2(\lambda)$ are the optical spectral powers generated at optical sources $S_1(\lambda)$ and $S_2(\lambda)$ respectively, $T_{Ref}(\lambda)$ and $T_{Meas}(\lambda)$ are the optical transmission spectra of the reference and measurement gas cells respectively, $F(\lambda)$ is the transmission spectrum of the optical bandpass filter, and $Resp_{meas\ diode}(\lambda)$ is the responsivity spectrum of the optical measurement signal detector diode.

The photo-currents developed at the reference detector during complementary switching of sources S_1 and S_2, are given by the equations:

$$I_{(Ref,S1)} = \int S_1(\lambda)F(\lambda)T_{Ref}(\lambda)Resp_{ref\ diode}(\lambda)d\lambda, \tag{3.4}$$

$$I_{(Ref,S2)} = \int S_2(\lambda)F(\lambda)Resp_{ref\ diode}(\lambda)d\lambda, \tag{3.5}$$

where $Resp_{ref\ diode}(\lambda)$ describes the spectral responsivity of the reference detector.

For correct operation, the above optical signals should be equalised prior to entering the measurement cell so that $I_{(Ref,S1)} = I_{(Ref,S2)}$, i.e. the power arriving at the reference detector, is assumed to be constant, irrespective of which optical source is active.

In order to continue the analysis the following assumptions are made:

1. The pre-measurement cell signal equalisation (or feedback) condition, as described above, is met, namely:

$$I_{(Ref,S1)} = I_{(Ref,S2)}. \tag{3.6}$$

2. The optical sources are assumed to have uniform and flat spectral emission over the transmission band of the optical bandpass filter. Thus, $S_1(\lambda)$ and $S_2(\lambda)$ may be regarded as constants and placed outside the integral expressions in the equations above.

3. The optical detector diodes have an equal and flat spectral responsivity over an equal or larger spectral range than the transmission spectrum of the optical bandpass filter. Hence the functions, $Resp_{ref\ diode}(\lambda)$ and $Resp_{meas\ diode}(\lambda)$ may similarly be considered to be constants in the equations above and placed outside the integral signs.

Equation 3.6 may now be reduced to an identity expressing the optical intensity of S_2 in terms of S_1. The application of these assumptions to Equation 3.6 yields the result:

$$S_1 = \left(\frac{\int F(\lambda) d\lambda}{\int T_{Ref}(\lambda) F(\lambda) d\lambda} \right) S_2, \tag{3.7}$$

which expresses the optical intensity of S_2 in terms of the optical intensity of S_1, and the application of these assumptions to the expression for the modulation index in Equation 3.1 gives:

$$m = 2 \left(\frac{\int F(\lambda) T_{Ref}(\lambda) T_{Meas}(\lambda) d\lambda \int F(\lambda) d\lambda - \int F(\lambda) T_{Ref}(\lambda) d\lambda \int F(\lambda) T_{Meas}(\lambda) d\lambda}{\int F(\lambda) T_{Ref}(\lambda) T_{Meas}(\lambda) d\lambda \int F(\lambda) d\lambda + \int F(\lambda) T_{Ref}(\lambda) d\lambda \int F(\lambda) T_{Meas}(\lambda) d\lambda} \right). \tag{3.8}$$

Any common mode deviation of the optical emission spectrum of the optical sources, or the responsivity spectrum of the optical detectors from the above assumptions may be represented by multiplying the spectrum of the optical bandpass filter by an appropriate function.

It may be observed from the form of equation 3.8 that on interchanging the reference and measurement gas cells, the same numerical value for the modulation index is obtained.

From a practical point of view Equation 3.8 may be put in the form shown in Equation 3.9, where A represents the factor by which S_2 should be modified, so that the feedback condition, described above, is met:

$$m = 2\left(\frac{\int S_1(\lambda)F(\lambda)T_{Ref}(\lambda)T_{Meas}(\lambda)Resp_{meas\ diode}(\lambda)d\lambda - A\int S_2(\lambda)F(\lambda)T_{Meas}(\lambda)Resp_{meas\ diode}(\lambda)d\lambda}{\int S_1(\lambda)F(\lambda)T_{Ref}(\lambda)T_{Meas}(\lambda)Resp_{meas\ diode}(\lambda)d\lambda + A\int S_2(\lambda)F(\lambda)T_{Meas}(\lambda)Resp_{meas\ diode}(\lambda)d\lambda}\right), \tag{3.9}$$

where

$$A = \frac{\int S_1(\lambda)F(\lambda)T_{Ref}(\lambda)Resp_{meas\ diode}(\lambda)d\lambda}{\int S_2(\lambda)F(\lambda)Resp_{meas\ diode}(\lambda)d\lambda}.$$

3.4 Fundamental Demonstration of the Operation of the Correlation Spectroscopy Method

In order to first describe and illustrate the operation of correlation spectroscopy, an analysis of the method is shown using a first-approximation to a gas absorption spectrum. This gas absorption is then analysed using the equation for the modulation index that has been derived in the previous section. A triangular shaped absorption line was chosen as a first approximation, as opposed to a more complex Gaussian shape, due to the simplicity with which it can be mathematically analysed. It will be seen in later chapters that the responses closely resemble those observed when physical gases are studied either by simulation or experiment.

3.4.1 Assumptions made for this Example

The four component terms in Equation 3.8 for the modulation index may be evaluated as they represent the area under each of the respective transmission functions. As the evaluation is a comparison of areas, it is independent of the absolute values of wavelength, consequently for this example the spectral wavelength range of the optical bandpass filter has been arbitrarily assumed to be 0 to 6. The calculation could equally be performed using wavenumbers, provided that the numerical functions representing the various components were to be suitably transformed.

3.4.2 Response of Correlation Spectroscopy with no Absorbing Gas Present in the Measurement Gas Cell

In this example, the spectrum of the optical bandpass filter is assumed to be rectangular in shape, with flat optical spectral transmission between 0 and 6 of unity as shown by

Figure 3.2. Thus the value of the term $\int_0^{\infty} F(\lambda)d\lambda$ is 6.0.

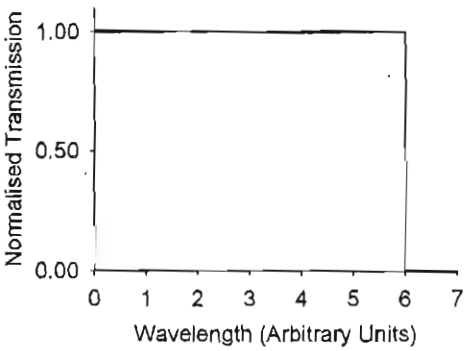

FIGURE 3.2: The transmission spectrum of the optical bandpass filter ($F(\lambda)$) used for this approximation.

The response of the correlation spectroscopy method is first demonstrated when the gas present in the measurement gas cell does not possess any absorption feature within the transmission window of the optical bandpass filter, as shown in Figure 3.3(b). The reference gas cell is assumed to be of unit length and filled with target gas with a triangular shaped absorption spectrum, the transmission spectrum of which is shown in Figure 3.3(a). The transmission spectrum of the reference gas cell is then described as a piece-wise mathematical function and integrated over the transmission window of the optical bandpass filter in Table 3.1. This results in a numerical value for the term $\int_0^{+\infty} F(\lambda)T_{Ref}(\lambda)d\lambda$ of 5.5.

As there is no gas absorption in the measurement gas cell, the term $\int_0^{6} F(\lambda)T_{Meas}(\lambda)d\lambda$ is identical to the transmission of the optical bandpass filter, ie.

$$\int_0^{+\infty} F(\lambda)T_{Meas}(\lambda)d\lambda = 6.00. \tag{3.10}$$

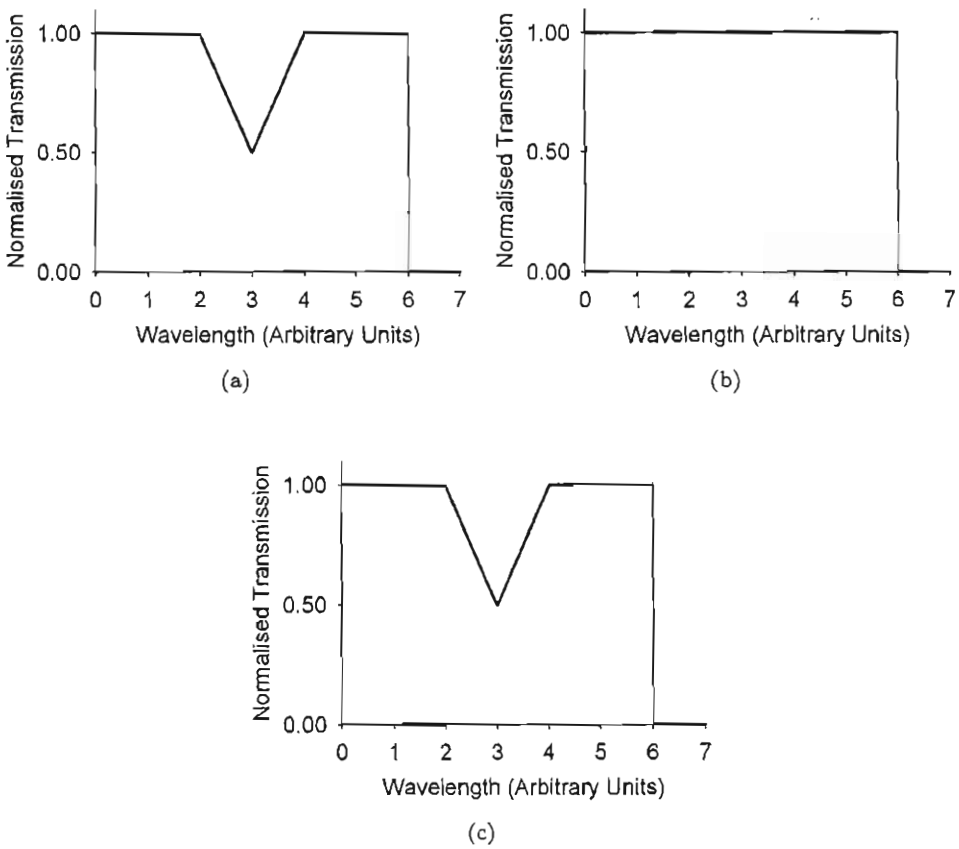

FIGURE 3.3: Response of a correlation spectroscopy system with no absorbing gas present in the measurement gas cell.
(a): Transmission spectrum of reference gas cell ($T_{Ref}(\lambda)$).
(b): Transmission spectrum of measurement gas cell ($T_{Meas}(\lambda)$).
(c): Combined transmission spectra of reference and measurement gas cell ($T_{Ref}(\lambda)T_{Meas}(\lambda)$).

Interval	Transmission Function	Area Integral Evaluation
$0 \leq \lambda < 2$	1	$\int_0^2 1 d\lambda = 2.00$
$2 \leq \lambda < 3$	$\left(2 - \frac{\lambda}{2}\right)$	$\int_2^3 \left(2 - \frac{\lambda}{2}\right) d\lambda = 0.75$
$3 \leq \lambda < 4$	$\left(\frac{\lambda}{2} - 1\right)$	$\int_3^4 \left(\frac{\lambda}{2} - 1\right) d\lambda = 0.75$
$4 \leq \lambda < 6$	1	$\int_4^6 1 d\lambda = 2.00$
	Total Area	$\int_0^{+\infty} F(\lambda)T_{Ref}(\lambda)d\lambda = 5.50$

TABLE 3.1: Evaluation of the piecewise linear function representing the transmission function of the approximated reference gas cell spectrum ($T_{Ref}(\lambda)$), filtered by the optical bandpass filter $F(\lambda)$

Also, because the measurement gas cell contains no spectral absorption feature in this spectral interval, the value of $\int_0^{+\infty} F(\lambda)T_{Ref}(\lambda)T_{Meas}(\lambda)d\lambda$ may be considered identical to that of the integral $\int_0^{+\infty} F(\lambda)T_{Ref}(\lambda)d\lambda$ calculated above, consequently

$$\int_0^{+\infty} F(\lambda)T_{Ref}(\lambda)T_{Meas}(\lambda)d\lambda = 5.50. \tag{3.11}$$

Substitution of these values into Equation 3.8 gives

$$m = 2\left(\frac{5.5 \times 6.0 - 5.5 \times 6.0}{5.5 \times 6.0 + 5.5 \times 6.0}\right) = 0.0\ , \tag{3.12}$$

as required.

3.4.3 Response to Target Gas Present in the Measurement Gas Cell

The response of a correlation spectroscopy system when the measurement gas cell contains target gas exhibiting the same optical absorption spectrum as the reference gas cell is now considered, and again the triangular-shaped absorption spectrum approximation is used. The transmission spectra of the reference and measurement gas cells are shown in figures 3.4(a) and 3.4(b), respectively.

The integral for the reference gas cell transmission may be evaluated as shown before in Table 3.1:

$$\int_0^{+\infty} F(\lambda)T_{Ref}(\lambda)d\lambda = 5.50, \tag{3.13}$$

and similarly for the target gas containing measurement gas cell:

$$\int_0^{+\infty} F(\lambda)T_{Meas}(\lambda)d\lambda = 5.50. \tag{3.14}$$

The spectrum of the reference and measurement gas cells in series is shown in Figure 3.4(c). This spectrum is the product of the reference cell and measurement cell gas spectra, in this specific case it is the square of either one. The evaluation of the integral for these gas cells in series is shown in Table 3.2 to be 5.17.

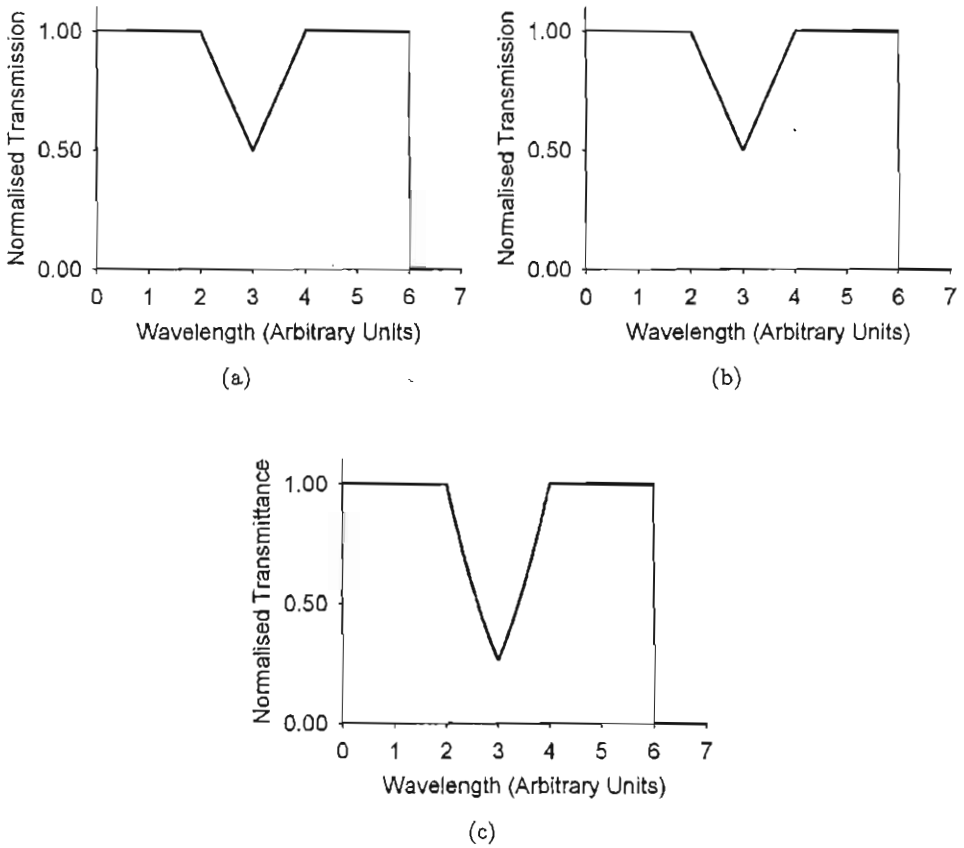

FIGURE 3.4: Response of correlation spectroscopy with target gas present in the measurement gas cell.
(a): Transmission spectrum of reference gas cell ($T_{Ref}(\lambda)$).
(b): Transmission spectrum of measurement gas cell ($T_{Meas}(\lambda)$).
(c): Combined transmission spectra of reference and measurement gas cells ($T_{Ref}(\lambda)T_{Meas}(\lambda)$).

Interval	Transmission Function	Area Integral Evaluation
$0 \leq \lambda < 2$	1^2	$\int_0^2 1^2 d\lambda = 2.00$
$2 \leq \lambda < 3$	$\left(2 - \frac{\lambda}{2}\right)^2$	$\int_2^3 \left(2 - \frac{\lambda}{2}\right)^2 d\lambda = 0.58$
$3 \leq \lambda < 4$	$\left(\frac{\lambda}{2} - 1\right)^2$	$\int_3^4 \left(\frac{\lambda}{2} - 1\right)^2 d\lambda = 0.58$
$4 \leq \lambda < 6$	1^2	$\int_4^6 1^2 d\lambda = 2.00$
	Total Area	$\int_0^\infty F(\lambda)T_{Ref}(\lambda)T_{Meas}(\lambda)d\lambda = 5.17$

TABLE 3.2: Evaluation of the piecewise function representing the series transmission of both the reference gas cell ($T_{Ref}(\lambda)$) and measurement gas cell ($T_{Meas}(\lambda)$) (both possessing the triangular shaped approximated gas absorption spectra), filtered by the optical bandpass filter transmission spectrum, $F(\lambda)$.

The modulation index when both cells contain target gas is, therefore,

$$m = 2\left(\frac{5.17 \times 6.00 - 5.50 \times 5.50}{5.17 \times 6.00 + 5.50 \times 5.50}\right) = 0.025 \ .$$

3.4.4 Response to Changing Concentration/Path-length of Target Gas in the Measurement Gas Cell

In order to show the effect of different optical path-lengths and different target gas concentrations of the measurement gas cell, the Beer-Lambert law is applied to the triangular shaped gas absorption spectrum. The relationship between the optical transmission of a gas sample and a change in concentration (partial pressure) or the path-length is expressed by the Beer-Lambert law, as shown by Equation 3.15, where I_0 is the incident power, I is the transmitted power, ϵ represents the molar absorption coefficient, c is the concentration of the gas and l is the path-length of the gas sample.

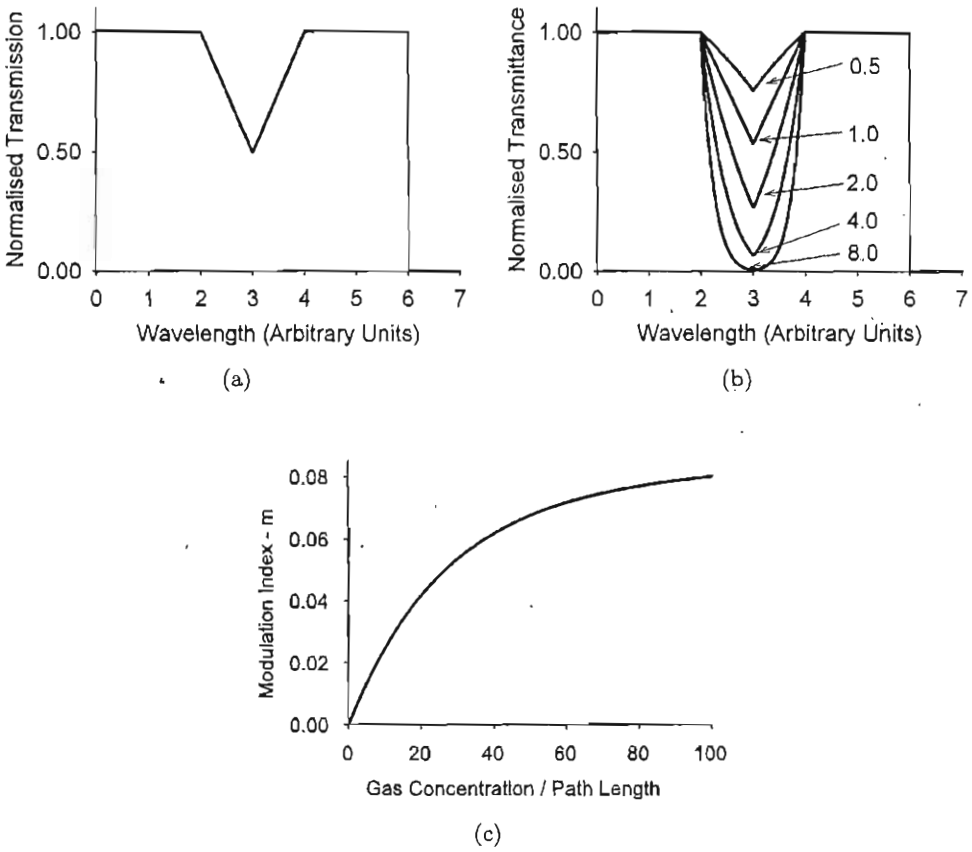

FIGURE 3.5: Response of a correlation spectroscopy system to changing gas concentration/path-length of the measurement gas cell.
(a): Transmission spectrum of reference gas cell.
(b): Transmission spectrum of measurement gas cell (the parameter is the power to which the triangular approximation is raised).
(c): Modulation index variation versus increasing partial pressure/gas cell path-length.

$$\frac{I_0}{I} = 10^{\epsilon(\tilde{\nu})cl}. \tag{3.15}$$

The correlation spectroscopy system is modelled with the reference gas cell containing a reference gas with the approximated transmission spectrum shown in Figure 3.5(a). The transmission spectrum of the measurement gas cell is modelled by the same triangular shaped absorption spectrum raised to various exponents, in an attempt to represent a change in gas concentration/path-length. The graphs in Figure 3.5(b) show these model spectra.

The modulation indices corresponding to these measurement gas cell spectra are shown in Figure 3.5(c). At low exponents the response can be seen to approximate to a near linear shape. However, as the exponent increases the response can be seen to tend asymptotically towards a final value.

3.4.5 Response to Different Line Intensities

The response of the correlation spectroscopy method to the approximated line-shape with varying strengths is now shown. This forms a basis for estimating the different responses that would be expected from absorption spectra with different strengths. Figure 3.6(a) shows the transmission spectra that were considered for both the reference and measurement gas cells with the approximated triangular peak absorption varied between 0 and 1. The modulation index was then calculated and the variation of modulation index versus absorption-line peak intensity is shown in Figure 3.6(b), which shows that with increasing intensity of the absorption line the modulation index increases in an exponential like manner.

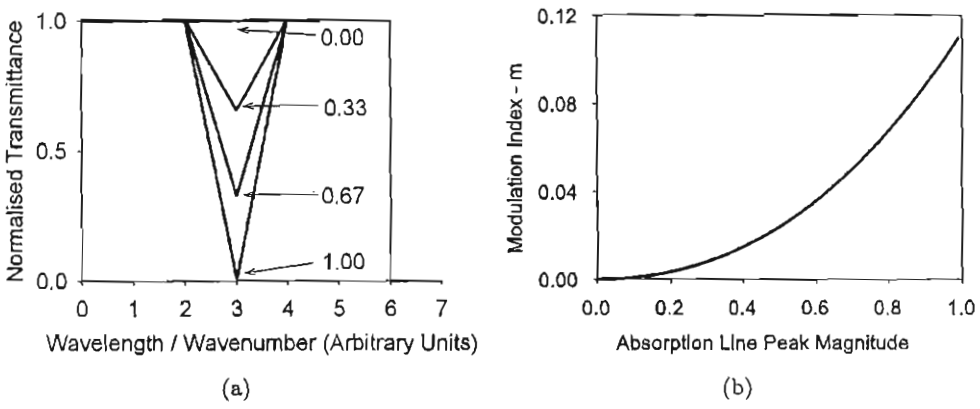

FIGURE 3.6: Response of a correlation spectroscopy system to varying absorption line strengths
(a): Transmission spectrum of reference gas cell.
(b): Resultant modulation index from differing concentrations.

3.4.6 Effects on Modulation Index due to Gases Present in the Measurement Gas Cell with Overlapping/Non-Overlapping Absorption Spectra

The effect of gas absorption in the measurement gas cell that coincides, overlaps or does not overlap with the absorption of the reference gas is now considered. This models the effect on the modulation index that would be expected from contaminant gases. The triangular shaped absorption spectrum shown is again assumed.

The triangular shaped absorption spectrum of the measurement gas cell is swept across the transmission spectrum of the optical bandpass filter, as indicated in Figure 3.7(a). This results in the variation of modulation index as a function of the wavelength displacement of the measurement gas cell absorption spectrum shown in Figure 3.7(b). This shows that the modulation index is dependent on the degree of overlap of the reference and measurement gas absorption spectra. When the absorption spectra overlap, the resultant modulation index is 0.025 and when they are non-overlapping, the resultant modulation index is -0.0083. In conclusion, whereas an overlapping (coincident) absorption spectrum results in a positive modulation index, a non-coincident absorption spectrum results in a negative modulation index. A negative modulation index can also be thought of as a 180° phase difference of the measurement signal compared to that which would be seen when target gas is present in the measurement gas cell.

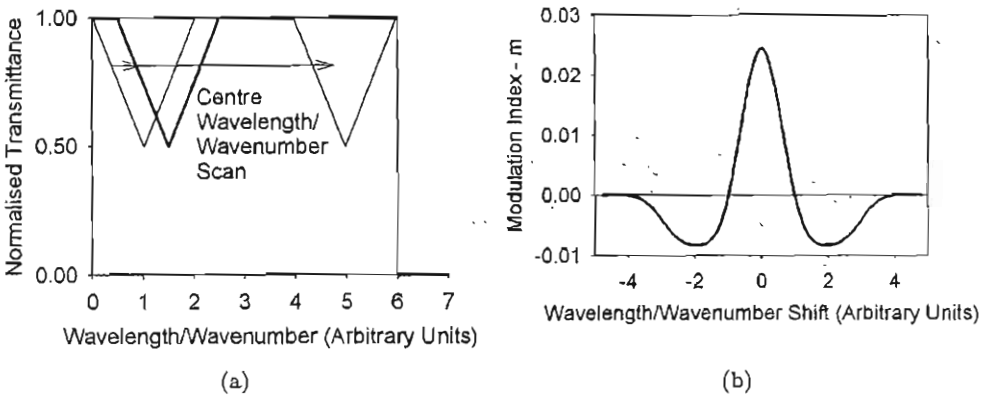

FIGURE 3.7: Effect of changing reference gas linewidth on modulation index(m).
(a): Transmission spectra of measurement gas cell.
(b): Modulation index variation versus increasing partial pressure/gas cell pathlength.

3.5 Conclusions

This chapter has introduced the concept of complementary source modulation correlation spectroscopy. This has included a definition of the technique, a derivation of the equation describing modulation index (m) and an illustration of the technique using an approximated absorption spectrum.

Chapter 4

The Hitran Database

4.1 Introduction

An account of how gas absorption data were extracted from the Hitran database is given in this chapter. These absorption data are used in later chapters as the base data for simulations that describe the operation of a correlation spectroscopy gas detection system. The study presented in this thesis, and the data reviewed in this chapter, primarily relate to the absorption of CO_2 gas at around 2 μm.

The account of the extraction of gas absorption data from the Hitran database in this chapter includes:

- A review of the physical phenomena that give rise to the absorption of light by gases.
- The operation of the Hitran-PC software, the software that was used to calculate the gas transmission spectra from the Hitran data.
- An illustration of the effects of variations in pressure and temperature on gas transmission spectra.

In order to quantify the accuracy of the Hitran data, a comparison of the Hitran data and an experimental observation is also included.

4.2 Fundamental Infra-red Gas Spectral Absorption Mechanisms

A review of the physical phenomena that give rise to spectral gas absorption is described in this section. This then allows the data in the Hitran database to be shown and the

procedures that the Hitran-PC software uses to be described, with the use of the CO_2 absorption spectrum at around 2 μm. The topics reviewed in the text below are the discussed in spectroscopy text books such as [29] and [30].

4.2.1 Rotational-Vibrational Light Absorption of CO_2

The absorption spectrum of CO_2 gas at around 2 μm arises from the interaction of light with rotational and vibrational energy resonances of the CO_2 molecule. The rotational and vibrational behaviours are first discussed individually, and then how these behaviours combine to form the infrared absorption spectrum of CO_2 is described.

4.2.1.1 Rotational Energy Transitions

As the spectroscopic absorption of light, in the infrared section of the electromagnetic spectrum, is the combination of rotational and vibrational behaviours, it is necessary to first review the theory of molecular rotational microwave absorption of radiation. The absorption of radiation at microwave frequencies by molecules is due to changes in their rotational energy state. Microwave absorption of radiation will occur, at defined frequencies, due to a resonance between the incoming radiation and the structure of the molecule, which will possess decreasing energy level populations at higher energy levels as described by the Boltzmann distribution:

$$\frac{N_{upper}}{N_{lower}} = \exp\left(\frac{-\Delta E}{kT}\right) \tag{4.1}$$

where N_{upper} and N_{lower} describe the difference in energy level populations of an upper and lower state, ΔE describes the difference in energy between the two states, k is the Boltzmann constant and T is the absolute temperature. In line with quantum theory, the permitted energy levels occur in discrete quanta. Hence, the absorption manifests itself as sets of discrete absorption lines. The quantum number associated with the rotational quantum energy levels is usually denoted J. With increasing values of J the degeneracy (the number of states a molecule possesses having identical energy) of the permitted energy states of the molecule increases as $2J + 1$. Therefore the relative populations of energy levels described in terms of J is:

$$Population \propto (2J + 1) \exp\left(\frac{-E_J}{kT}\right), \tag{4.2}$$

where E_J is the energy associated with the rotational quantum number. A solution of the Schrödinger wave equation yields a mechanism for describing the permitted absorptions of energy that may occur. This results in a series of selection rules that describe the

permitted changes in J that are allowed. Each change in the value of J (ΔJ) results in a branch of the absorption spectrum. With the exclusion of Raman effects (as these are beyond the scope of this thesis) the values of ΔJ that give rise to the absorption spectrum are:

- $\Delta J = -1$ (P branch)
- $\Delta J = 0$ (Q branch)(this only occurs in molecules that are not symmetric)
- $\Delta J = +1$ (R branch)

4.2.1.2 Molecular Vibrations

A molecule may vibrate in a number of modes. The permitted modes of vibration of the CO_2 molecule are shown in Figure 4.1. Vibrations associated with the symmetric stretch, symmetric bend and asymmetric stretch are labelled v_1, v_2 and v_3 respectively.

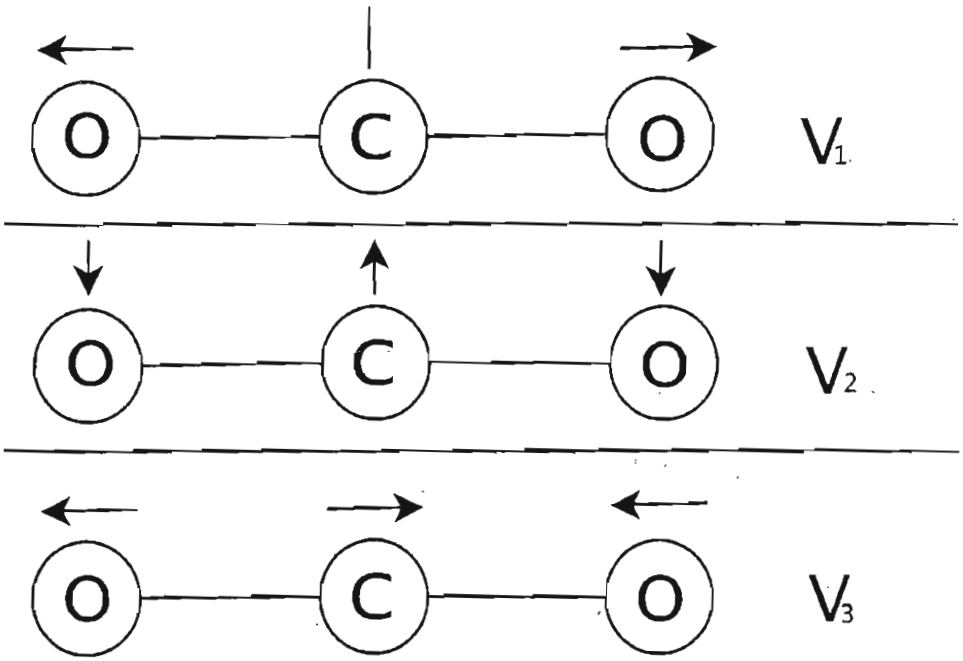

FIGURE 4.1: Diagrammatic illustrations of the v_1, v_2 and v_3 vibration motions. The v_1 mode is the symmetric stretch, the v_2 mode is the symmetric bend and the v_3 mode is the asymmetric stretch.

Each of the fundamental molecular vibrations of CO_2 may be considered to be an oscillation, where the energies are considered to be quantised. Multiples of each fundamental frequency also exist, which are known as overtones. These overtones are normally denoted by placing an integer before the term for the fundamental vibration. Figure 4.2 diagrammatically shows these vibrational energy transitions and shows energy transitions that occur within an energy well described by an anharmonic oscillator. Vibrational energy transitions may also occur between energy levels not involving the ground

state and these are termed hot-bands, as they increase in magnitude with increasing temperature.

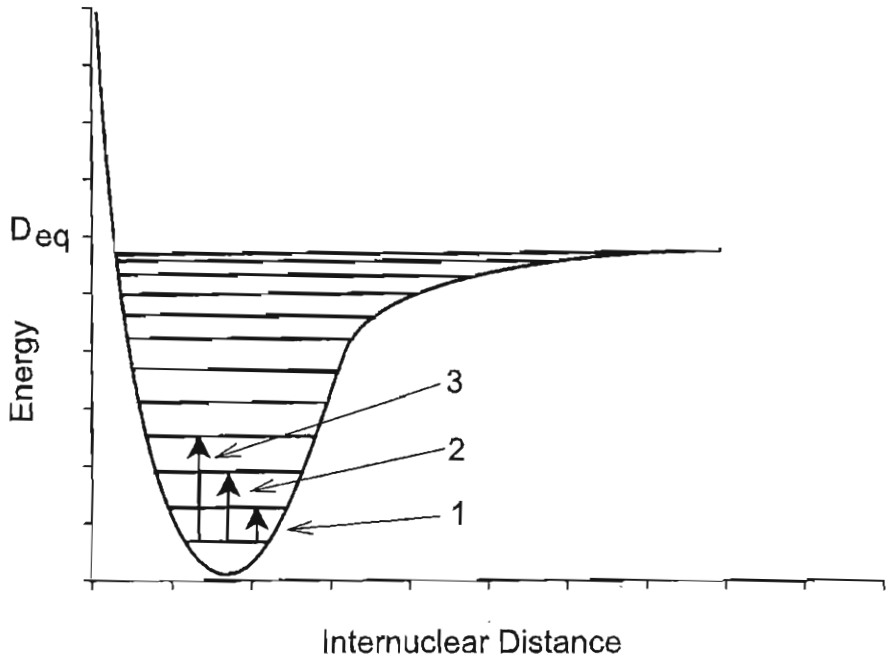

FIGURE 4.2: The energy transitions that give rise to the vibrational spectral absorptions. The fundamental and the first and second overtones are shown. The quantised energy well is shown as being described by an anharmonic oscillator.

4.2.1.3 Combination of Rotation and Vibration

Each vibrational energy level is associated with a series of rotational energy levels. Energy transitions may occur between the rotational energy levels associated with different vibrational energy levels. This results in a rotational absorption spectrum appearing around each vibrational frequency and its overtones.

4.2.1.4 Fermi Resonance

Where the distribution of energy population levels overlap, giving rise to overlapping absorption lines, a Fermi resonance may occur. This is where energy coupling between the energy transitions occurs, usually resulting in the depletion of one absorption and the strengthening of the other. With infrared absorption spectra, Fermi resonances usually occur where the spacing between the absorption lines is of the order of tenths of nanometres. The Fermi resonance is described by an integer value describing the order of the perturbation of the energy states. A value of 1 describes the unperturbed state and higher values describe the increasing orders of perturbation.

4.2.2 Hitran Database

The Hitran database is a compilation of previously measured and/or calculated spectroscopic absorption data that can be used to approximate the transmission of radiation through a gas sample. The Hitran database was used as the source of the base spectroscopic data for the simulations, the results of which are shown later in this thesis. For the purposes of the simulations, the data were used as a numerical approximation to the transmission spectra of the reference and measurement gas cells - represented by the numerical functions $T_{Ref}(\lambda)$ and $T_{Meas}(\lambda)$, respectively (defined in Chapter 3). These data enabled numerical approximations, to the values $\int T_{Ref}(\lambda)d(\lambda)$ and $\int T_{Meas}(\lambda)d(\lambda)$ over the spectral intervals chosen, to be calculated.

The simulations described in this thesis concerning the detection of CO_2 gas used data from the Hitran 2000 [31] database. The parameters that are used to calculate the absorption spectrum for each energy transition are listed below.

- Vacuum wavenumber (cm^{-1}).
- Line strength.
- Air-broadened line half-width.
- Self-broadened line half-width.
- Energy of the lower state.
- Temperature dependence.
- Air-pressure shift.

The parameters that are listed above were derived from spectra that were observed experimentally and also from the literature published by Mandin *et al.* [32] in 1977. These data, together with other published experimental data that were then available, were reinterpreted by Rothman *et al.* in 1992 [33] by means of a Direct Numerical Diagonalisation data fitting technique. However, segments of these data were found to disagree with later experimental measurements and theoretical calculations, for example Aguir *et al.* [34] observed that the spectral locations of some band centres disagreed with their theoretical study by up to 36 cm^{-1}. The findings of Aguir *et al.*, the work of Mandin *et al.* in 1977 and others were then incorporated by Tashkun *et al.* [35] into the Carbon Dioxide Spectral Databank (CDSD). Finally, in late 2004, as this thesis was being prepared, Rothman *et al.* released the Hitran 2004 database [36]. The revisions relating to CO_2 gas consisted of the substitution of the CDSD data for the earlier data.

The Hitran notation for linear triatomic molecules with a large Fermi resonance is used (class 5, for the purposes of Hitran [36]). This class of molecule includes CO_2.

Rotational-vibrational transitions with a large Fermi resonance are described by the Hitran notation $v_1 v_2 l v_3 r$ [36], where v_1 is an integer representing the overtone of the symmetric stretch mode, v_2 is an integer representing the overtone of the bending mode and l is an integer representing quantised angular momentum associated with the bending mode, v_3 is an integer representing the overtone of the antisymmetric stretch mode and r is the ranking index of the perturbation associated with the Fermi resonating group.

The quantum energy transitions resulting in the absorption spectrum of CO_2 at approximately 2 μm are shown in Table 4.1. As may be observed, the CO_2 absorption spectrum around 2 μm is mainly composed of the $2v_1 + v_3$ and $v_1 + 2v_2 + v_3$ interactions with the ground state, which are shown in bold in Table 4.1. There are also contributions from several "hot bands", which are also listed in Table 4.1.

20012-00001	40002-01101	31113-11101	**20013-00001**	30014-10002
21113-01101	30013-10001	21112-01101	**12212-00001**	30013-10002
20022-00011	40014-20003	31113-11102	40013-20002	22212-02201
32213-12202	30012-10001	23312-03301	**20011-00001**	31112-11101
40012-20001	30012-10002	21111-01101	30011-10001	22211-02201
12211-00001	20021-00011	31112-11102	31111-11101	23311-03301

TABLE 4.1: The energy transitions that lead to the optical absorption by CO_2 at around 2 μm, Hitran notation is used, which is described in the text (these data may be obtained from [31], or the JHawks Software that is supplied with the Hitran database).

Commercial software is available to evaluate the parameters contained within the Hitran database that were listed above, and produce a data file with numerical data representing the absorption/transmission versus wavelength. One such program, which was used for all gas spectra in this thesis, is Hitran-PC. Hitran-PC is distributed by Ontar Corporation and was developed by the University of South Florida (USF).

The composite transmission spectrum of CO_2, in the spectral region of 1.9 μm up to 2.1 μm, as detailed in the Hitran database and resulting from the absorption bands listed in Table 4.1, is shown in Figure 4.3. A path-length of 26 cm, a temperature of 20°C and a pressure of 1 bar were modelled. The data shown in Figure 4.3 was computed using the Hitran-PC software that is described in the following section. A path-length of 26 cm was chosen, so that a comparison can be made between the simulated results presented in this chapter and the experimental results presented in Chapter 6. Figure 4.3 also shows the P-R branch structure associated with each transition and the spectroscopic nomenclature associated with each absorption band.

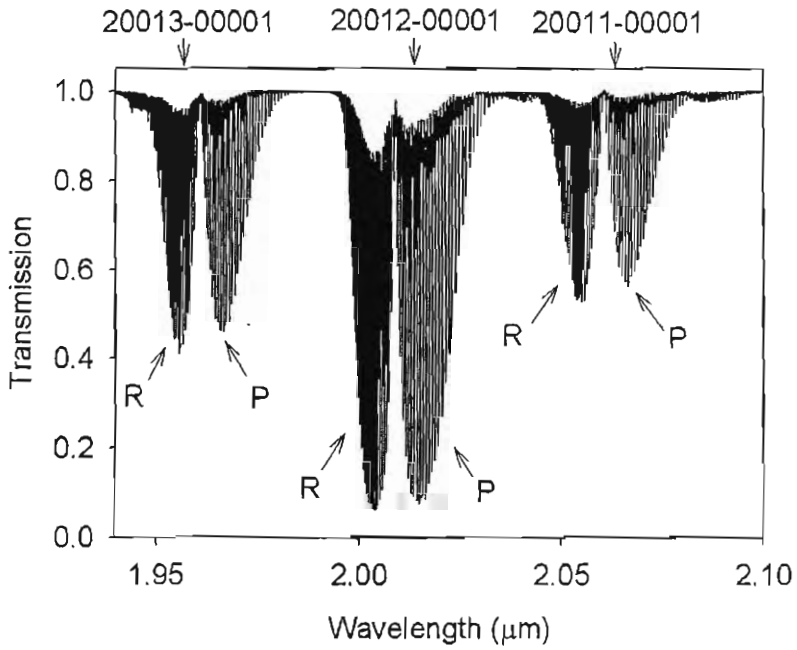

FIGURE 4.3: Transmission spectrum of 100% CO_2 gas over a 26 cm path length at 20°C and at a total pressure of 1 bar (transmission data were obtained from the Hitran database and processed by Hitran-PC).

4.3 Effects of Changing Pressure

The absorption lines, that manifest themselves as a result of the quantised nature of the rotational energy transitions, have a finite linewidth due to the collision of molecules and the motion of molecules. The most significant cause of line broadening in heavy molecules, such as CO_2, with gas pressure is that of collision broadening. This is where two molecules collide and then exit from the collision with a phase change. The rate of collisions increases with gas pressure. The line broadening effects resulting from collision broadening are described by a Lorentz lineshape. Random molecular motion, to a lesser extent, also contributes to the observed linewidth of gases such as CO_2. This is termed Doppler broadening. The Voigt lineshape, which incorporates both the Lorentian and Doppler lineshapes, was used for all gas spectra shown in this thesis.

The effects of line-broadening, with increasing pressure, are illustrated in Figures 4.4 and 4.5 respectively. The graph in Figure 4.4 shows the effect of pressure broadening for the three most intense absorption lines in the R branch of the 20012-00001 CO_2 absorption at around 2 μm, and Figure 4.5 shows the effect of three weaker lines in the same absorption branch. The graph in Figure 4.5 shows that the absorption lines are decreasing in magnitude with decreasing wavelength. This is because the lines are representative of the tail of the energy level distribution (see equation 4.2 above).

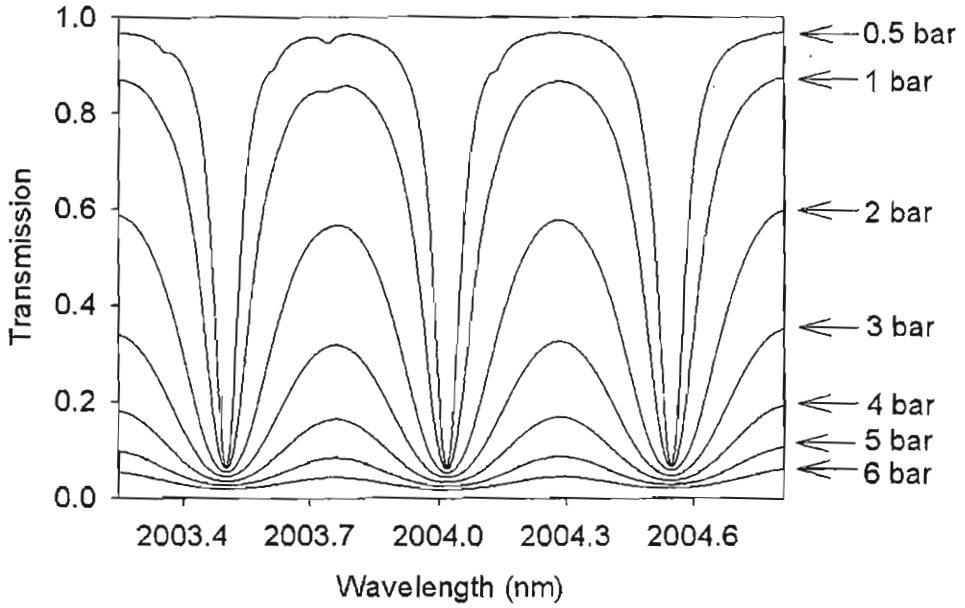

FIGURE 4.4: Transmission spectra of three lines at the peak absorption of the R branch of the 20012-00001 transition of CO_2 at different gas pressures. The graph shows the Hitran data for a temperature of 20°C and a path-length of 26 cm.

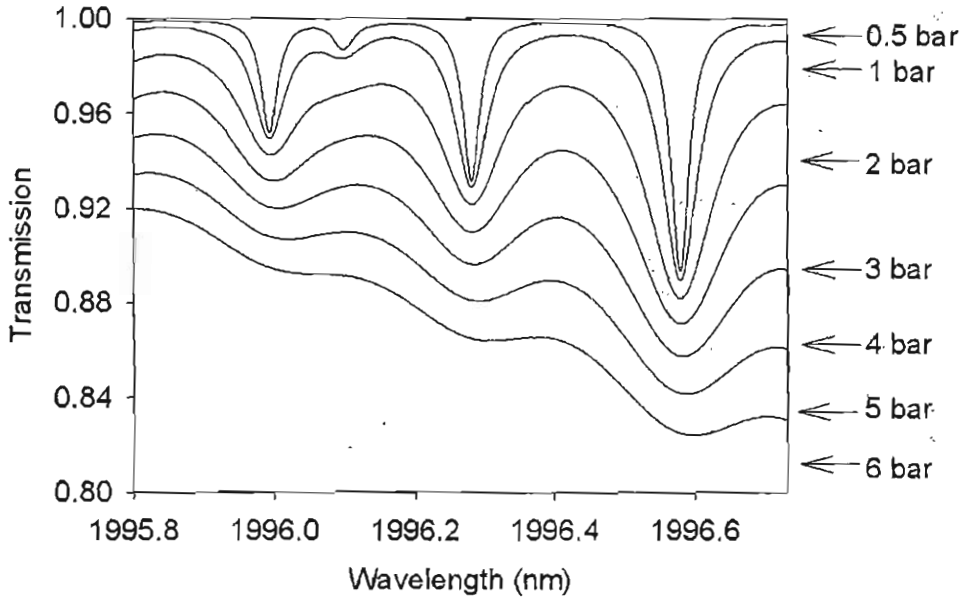

FIGURE 4.5: Transmission spectra of three weak lines in the R branch of the 20012-00001 transition of CO_2 at different gas pressures. The graph shows the Hitran data for a temperature of 20°C and a path-length of 26 cm.

4.4 Effects of Changing Temperature

According to the ideal gas law ($PV = nRT$, where P is the gas pressure, V is the gas volume, n is the number of moles of gas present, R is the molar gas constant and T is the absolute temperature), a change in the temperature of a gas will result in a change in the density of a gas, if the gas pressure is held constant. This means that the quantity of the gas present in a fixed optical path should reduce with an increase of temperature.

From Equation 4.2, shown above, it would also be expected that the rate of decay of the Boltzmann distribution would decrease. As a consequence of the rate of increasing degeneracy of the molecule, $2J + 1$, having no temperature dependence, a net increase of the wavelength distance from the band centre of the absorption band and the peaks of the P-R branches would be expected.

The results of these effects on the sets of strong and weak absorption lines are shown in Figures 4.6 and 4.7. Figure 4.8 shows the effect of a temperature change of 100°C on the band origin; this effect is caused by the shift in the peaks of the P and R branches.

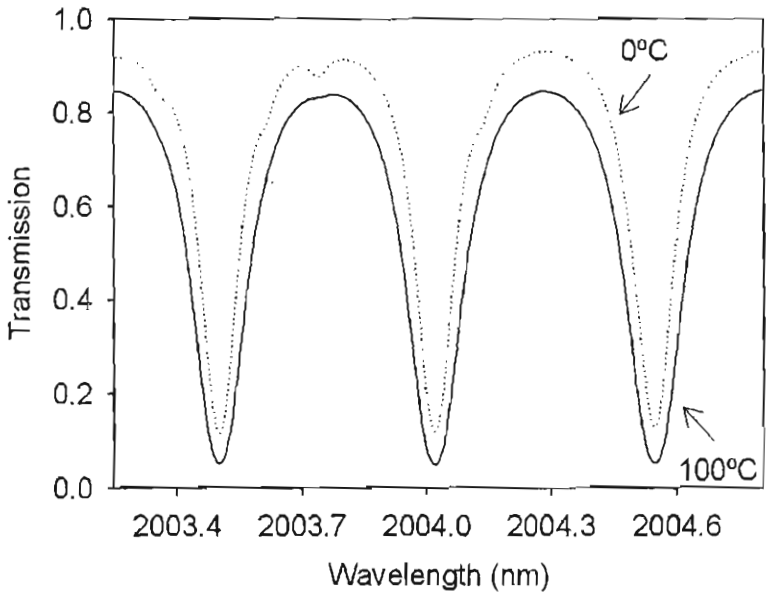

FIGURE 4.6: Transmission spectra of three intense lines in the R branch of the 20012-00001 transition of CO_2 at different gas temperatures. The graph shows the Hitran data for a total pressure of 1 bar and a path-length of 26 cm.

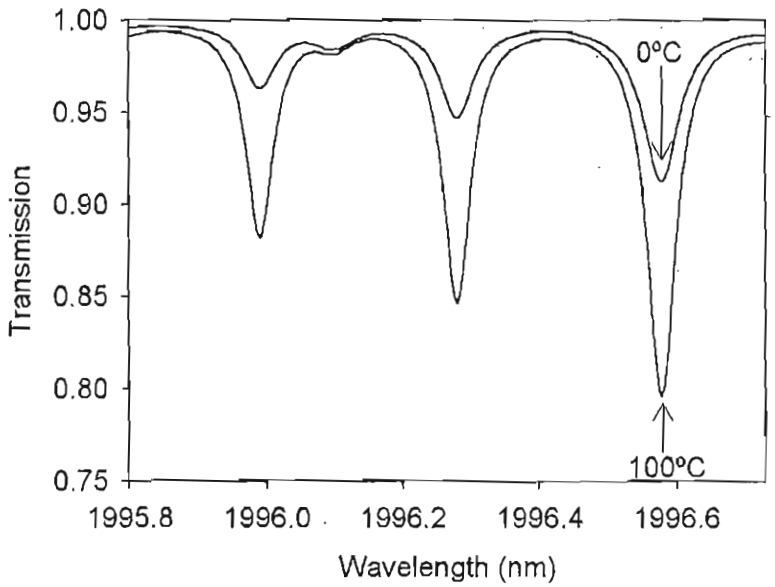

FIGURE 4.7: Transmission spectra of three weak lines in the R branch of the 20012-00001 transition of CO_2 at different gas temperatures. The graph shows the Hitran data for a total pressure of 1 bar and a path-length of 26 cm.

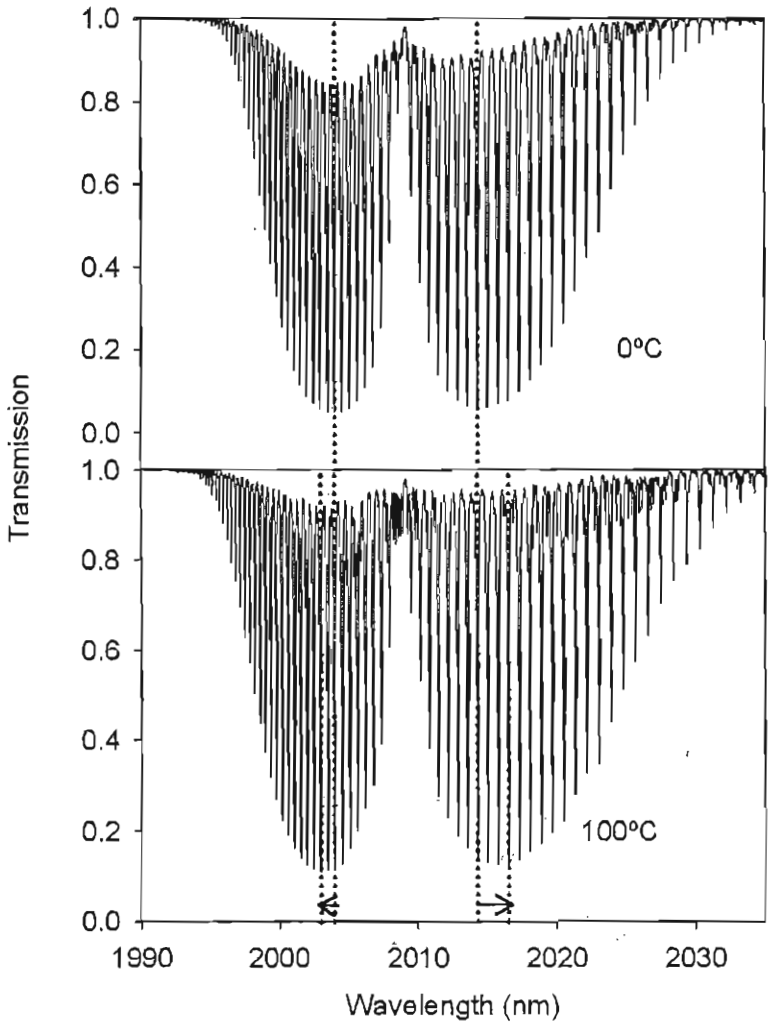

FIGURE 4.8: Transmission spectra of the 20012-00001 transition of CO_2 at different gas temperatures, the trend of the peak absorption tending away from the centre wavelength of the transition is shown. The graph shows the Hitran data for a total pressure of 1 bar and a path-length of 26 cm.

4.5 Comparison of Hitran CO_2 data with an Experimental Observation

In order to compare the Hitran data with a direct experimental observation, a CO_2 containing 10 cm long gas cell was inserted into the sample compartment of a Varian Cary 500 UV/NIR spectrophotometer. Using the spectrophotometer, the transmission spectrum of the CO_2 gas sample was scanned between 1.9 μm and 2.1 μm using a slit bandwidth of 2 nm, which yielded a low noise measurement. The data were normalised to a background measurement that used the 10 cm long gas cell filled with N_2 gas, which has no absorption bands around 2 μm. The measurement that was obtained is shown in Figure 4.9. Data were also extracted from the Hitran database using the Hitran-PC program over the same spectral wavelength range, with the same 10 cm pathlength and, for comparison, are also shown in Figure 4.9.

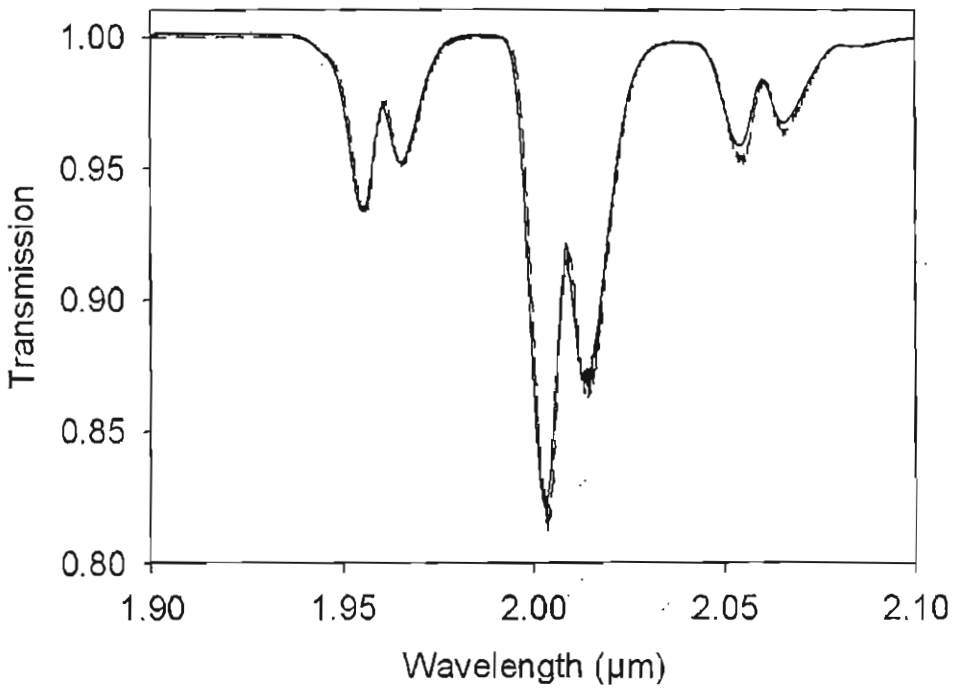

FIGURE 4.9: Experimental observation of the CO_2 gas absorption spectrum. Data extracted from the Hitran database filtered with a 2 nm bandwidth rectangular filter is also shown for comparison.

A difference plot of the experimentally observed data and the Hitran extracted data is shown in Figure 4.10. The standard deviation of the difference of the two data sets is 3.5×10^{-3}, which is 0.4% of the peak transmission of the CO_2 absorption in this spectral interval. This suggests that the Hitran data should be able to give predictions of the gas absorption to within 0.4% of the actual absorption.

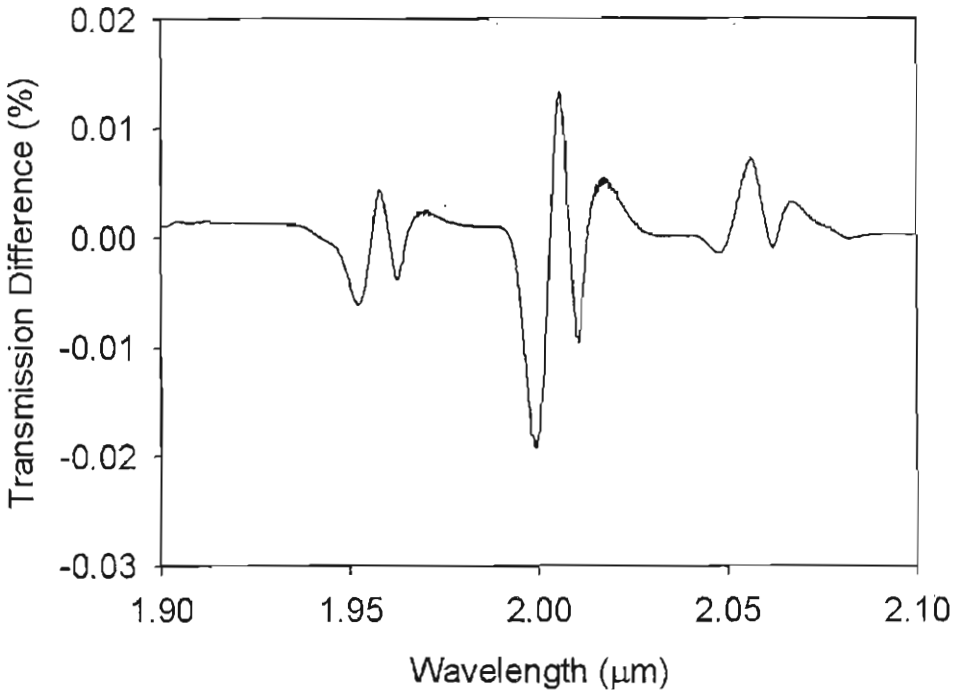

FIGURE 4.10: Difference between the recorded spectrum on the spectrophotometer and the processed Hitran data.

4.6 Conclusions

This chapter has summarised the physical phenomena that give rise to the spectral absorption of CO_2 at around 2 μm and described published data that quantifies these effects in the Hitran database and software that computes the resultant transmission spectrum, Hitran-PC.

Following on from this discussion the effects of pressure and temperature changes on the transmission spectrum of individual lines were shown and described. The effects of pressure broadening were principally due to collision broadening which forms part of the Voigt lineshape. The effects of temperature changes were also shown, these were shown to be of reduced absorption magnitude, due to the change in molecular density and the changes in the molecular energy levels, which manifests itself as a separation of the peaks of the P-R absorption spectrum.

Finally, in order to quantify the accuracy of the Hitran database, a comparison between data from the Hitran database, processed by Hitran-PC, and an experimental observation was shown. This showed that the standard deviation of the difference between the measured data and the Hitran data was 0.4%. This good agreement confirms that the use of the Hitran database to predict experimental behaviour is well justified.

Chapter 5

Simulation of Correlation Spectroscopy Method

5.1 Introduction

Simulated results describing the response of a correlation spectroscopy system are shown in this chapter. The results that are presented and discussed relate principally to the detection of carbon dioxide gas (CO_2). Simulation results concerning the detection of methane gas (CH_4) and oxygen gas (O_2) are also presented. The differences between the results obtained for the detection of CH_4 gas and O_2 gas and those obtained for the detection of CO_2 gas are then shown.

The discussion of the detection of each gas starts with a the presentation of the gas transmission spectrum. The results from the simulations that describe the dependence of modulation index upon the choice of light sources and optical bandpass filter are shown and discussed.

The impact of the input signal power on the signal to noise ratio in the output measurement signal is analysed. A method of increasing the sensitivity of a correlation spectroscopy system by increasing the gas pressure of the reference gas cell is then discussed with application to the detection of CO_2 gas.

The effects on the system sensitivity to a contaminant gas (water vapour was selected) is also considered, from both the viewpoint of the dependence on modulation index of the bandwidth of the optical bandpass filter and of the pressurisation of the reference gas cell.

In Chapter 6, results obtained by simulation are compared to results obtained by experiment.

5.2 Spectroscopic Data for the Absorption of CO_2

The monitoring of the concentration of CO_2 gas present in an atmosphere may be required for the control of a variety of processes. These processes may be biological, industrial or domestic in nature. CO_2 gas is an important component of the atmosphere of the Earth and other planets. CO_2 gas is also a greenhouse gas that contributes to global warming [37].

The spectroscopic origins of the CO_2 absorption at around 2 μm, shown in Figure 5.1, was discussed in Chapter 4. A path-length of 26 cm is used for Figure 5.1, because this was the length of the gas cells used for the experiments described in Chapter 6.

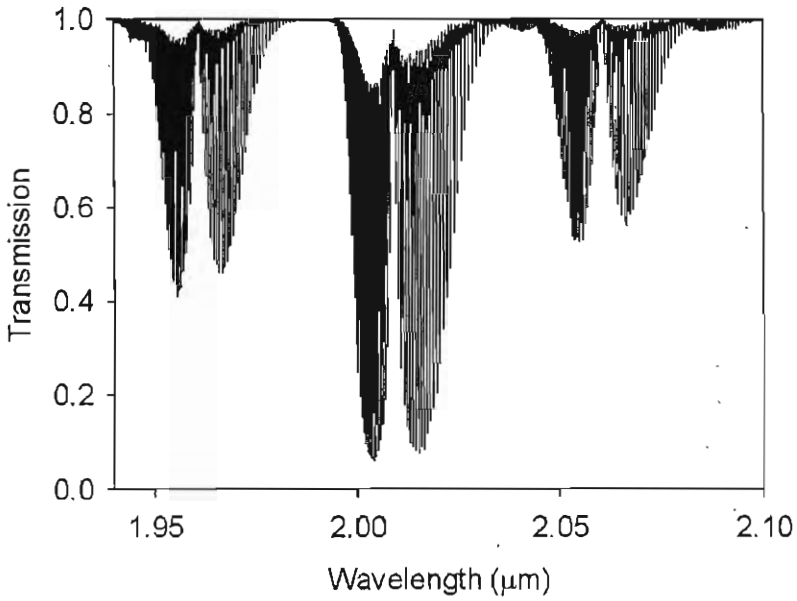

FIGURE 5.1: Transmission spectrum of 100% CO_2 gas over a 26 cm path length at 20°C and at a total pressure of 1 bar (transmission data were obtained from the Hitran database).

5.3 Determination of Effects of Selection Optical Components used in a Correlation Spectroscopy System

In this section the effects of the choices of the centre wavelength and the Full width at Half Maximum (FWHM) bandwidth of the Gaussian shaped optical bandpass filter are graphically shown and described. The FWHM bandwidth is the bandwidth between the half-maximum values of the Gaussian shaped optical transmission function. The choice of optical bandpass filter also shows the effect of any common mode change in the emission spectrum of the light sources or the responsivity spectrum of the optical detectors.

5.3.1 Effect of varying the Centre Wavelength of the Optical Bandpass Filter

The dependence of modulation index on the centre wavelength of the optical bandpass filter was first determined with a narrow 2 nm FWHM bandwidth. Figure 5.2 shows the effect on the modulation index of sweeping the centre wavelength of this narrow optical bandpass filter across the spectrum of the CO_2 absorption around 2 μm. It may be observed that the shape of the response closely relates to a convolved (or "smoothed") version of the original CO_2 absorption spectrum. It was found that with the use of this narrow 2 nm FWHM bandwidth filter, a maximum modulation index of 0.161 was obtained at a centre wavelength of 2.004 μm. So that the graphical results remain consistent, a centre wavelength of 2.004 μm was adopted for the results presented, which relate to the simulated response of a CO_2 correlation spectroscopy detection system.

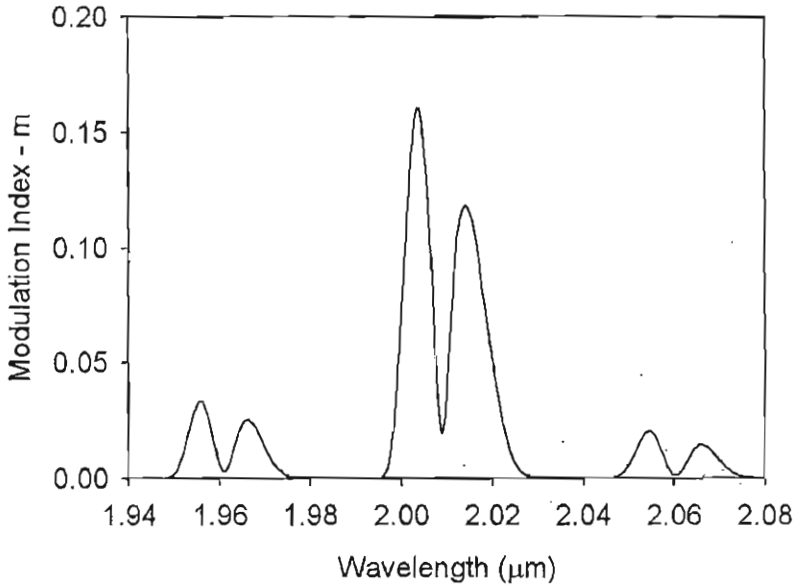

FIGURE 5.2: Modulation Index (m), as a function of optical bandpass filter centre wavelength. The reference and measurement gas cells were modelled as both being of length 26 cm, containing 100% CO_2 gas, at a temperature of 20°C and at a total pressure of 1 bar. The transmission spectrum of the optical bandpass filter was modelled as being Gaussian shaped and possessing a 2 nm FWHM bandwidth.

5.3.2 Effect of Varying the Bandwidth of the Optical Bandpass Filter

The effect of varying the FWHM bandwidth of the optical bandpass filter was investigated by considering bandwidths from 0.1 nm up to 200 nm. The centre wavelength of the optical bandpass filter was taken to be 2.004 μm. Figure 5.3 shows the result of this simulation. The response of the modulation index can be seen to rise quickly to a maximum, where the optical bandpass filter was centred on the side of an absorption

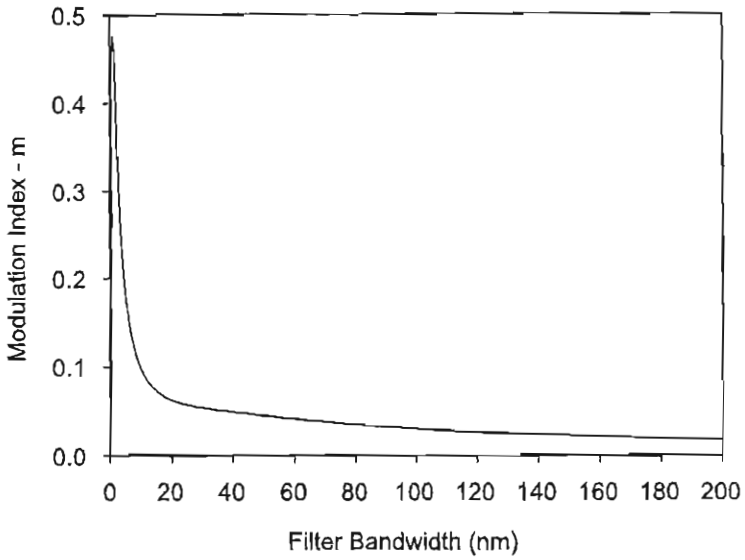

FIGURE 5.3: Modulation Index (m) versus the optical bandpass filter FWHM bandwidth. The reference and measurement gas cells were modelled as being 26 cm long and containing 100% CO_2 gas at a temperature of 20°C and a total pressure of 1 bar. The Gaussian shaped optical bandpass filter was modelled as having a centre wavelength of 2.004 μm.

line and then decay towards zero, where the rate of decay is effected by the positive contribution of absorption lines included as the bandwidth of the optical bandpass filter increases.

5.3.3 Combined Effect of Varying the Centre Wavelength and Bandwidth of the Optical Bandpass Filter

With changing optical bandpass filter centre wavelength, the optimal bandwidth to chose for the optical bandpass filter may change, and with changing bandwidth the optimal centre wavelength may also be effected. For completeness Figure 5.4 shows a composite 3-dimensional graph of the combined effects of varying the optical bandpass filter centre wavelength and the FWHM bandwidth.

5.4 Signal to Noise Considerations

Thus far the discussion has concentrated on the modulation index and it was found that the optimum was achieved with a narrow bandwidth of the optical bandpass filter centred on a relatively intense absorption line.

While with the use of a narrow-band optical bandpass filter a maximum modulation index would be attained, a wider bandwidth optical bandpass filter would allow more

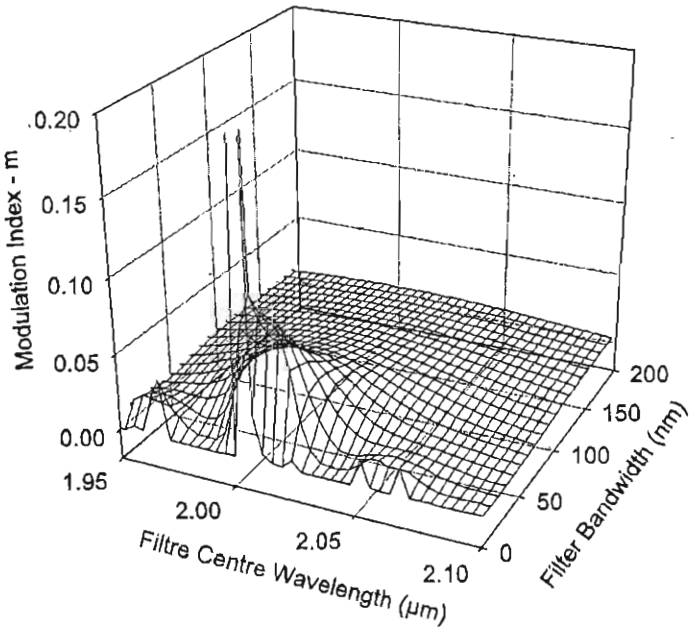

FIGURE 5.4: Modulation Index (m) as a function of the centre wavelength and FWHM bandwidth of the optical bandpass filter . In aiding the graphical representation of these simulation data the data-set has been undersampled so that the underlying behaviour of the plot can be seen. The 26 cm long reference and measurement cells were modelled as containing 100% CO_2 gas at a temperature of 20°C and at a total pressure of 1 bar.

optical power to be transmitted. Thus a wider bandwidth optical bandpass filter would allow a greater signal to noise ratio (SNR) to be obtained at the measurement detector.

The effects on the signal to noise ratio, due to photon (shot) and thermal noise incident, on the measurement signal detector are now examined. Photon noise arises from the incidence of optical radiation on a semi-conductor detector and thermal noise arises from the feedback resistor in the associated transimpedance amplifier. The magnitude of photon and thermal noise are given by the equations:

$$\begin{aligned} I_{ShotNoise} &= \sqrt{2qI_{Sig}B}, \\ I_{ThermalNoise} &= \sqrt{4kTB/R_{Feedback}}, \end{aligned}$$

where q is the electronic charge, k is the Boltzmann constant, T is the absolute temperature (assumed to be room temperature, 20°C, 293 K), I_{Sig} is the mean DC output current of the output detector and B is the noise bandwidth. The effect of filtering the output with a low-pass filter with a time constant of 10 seconds was modelled. This resulted in a value for the noise bandwidth, B, of 0.025 Hz (see Appendix A of reference [38]).

The effect on the SNR in the measurement signal of increasing the optical bandpass filter bandwidth at three different spectral power intensities is shown in Figure 5.5.

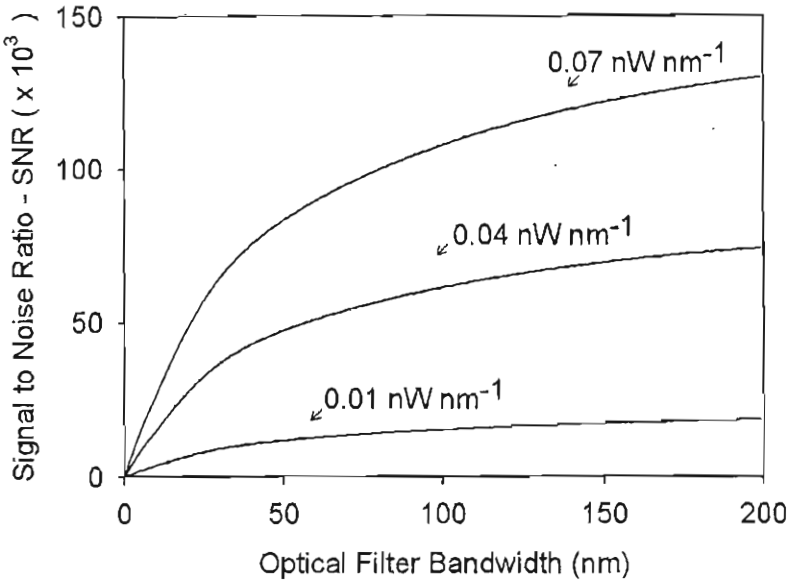

FIGURE 5.5: Simulated variation in SNR at three different source power spectral intensity, ranging from 0.01 nW nm^{-1} to 0.07 nW nm^{-1} as the bandwidth of the Gaussian shaped optical bandpass filter (centred at 2.004 μm) is increased. The quoted spectral power intensity is the average power intensity that would arrive at the measurement detector if there were no absorption in the measurement gas cell. The reference and measurement gas cells were modelled as being 26 cm long and as containing only CO_2 gas at a temperature of 20°C and at a total pressure of 1 bar.

With increasing optical bandpass filter bandwidth, the SNR initially rises (as shown in Figure 5.3) since the rate of decrease in the modulation index is initially less than the square root increase of the component noise sources described above. However, with increasing optical bandpass filter bandwidth, and consequently increasing signal noise power, the SNR will eventually begin to decrease (not shown in Figure 5.3). For the purpose of the discussion in this thesis, a FWHM bandwidth of 175 nm is adopted because this approximates to the bandwidth of the Light Emitting Diode (LED) light source used in the experiments described in Chapter 6.

When the SNR shown in Figure 5.5 is combined with the trend of the modulation index with measurement gas cell concentration, a minimum detectable CO_2 gas concentration may be estimated. From the simulation this was found to be 0.01% (100 ppm) with an optical bandpass filter bandwidth of 175 nm and a received optical power level of 0.01 nW nm^{-1}.

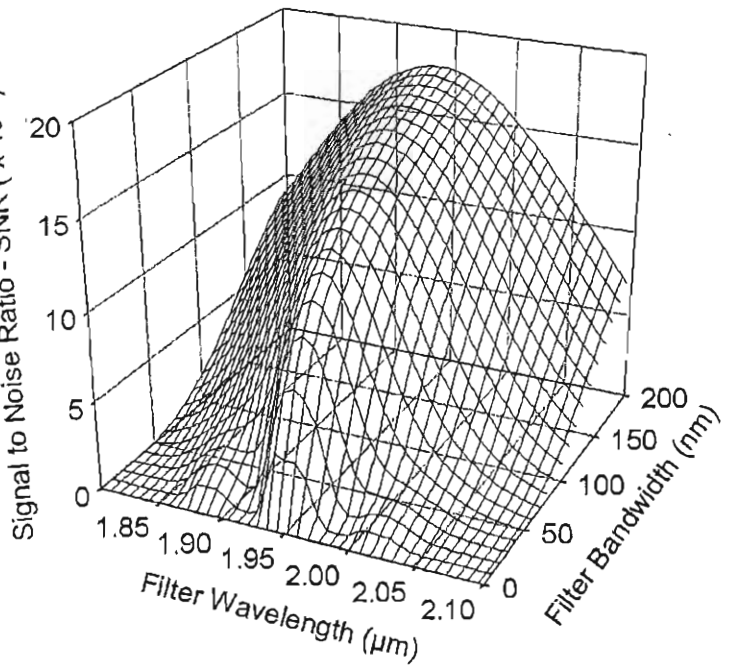

FIGURE 5.6: Signal to Noise Ratio (SNR) in the measurement signal as a function of the centre wavelength and FWHM bandwidth of the optical bandpass filter . In aiding the graphical representation of these simulation data, the data-set has been undersampled so that the underlying behaviour of the plot can be observed. The spectral power intensity was modelled as being 0.01 nW nm^{-1}. Other conditions are as per Figure 5.5.

In Figure 5.6 the simulated SNR as a function of the optical bandpass filter bandwidth and centre wavelength is shown on a 3-dimensional plot. This shows that the shape of the simulated SNR response, indicated in Figure 5.5, occurs at other optical bandpass filter centre wavelengths, but with diminished magnitude, as the centre wavelength of the optical bandpass filter moves away from the most intense CO_2 absorption at 2.004 μm.

5.5 The Effect of Varying CO_2 Concentration within the Measurement Gas Cell

The effect of varying the concentration of CO_2 target gas in the measurement gas cell on the modulation index is shown in Figure 5.7. The shape of the modulation index response can be seen to closely resemble a linear response at low concentrations before approaching a maximum of 0.018 at 100% CO_2 gas concentration. This response has the same shape as that found by approximation in Section 3.4.4, Chapter 3, and is also further discussed in Section 6.3 of Chapter 6.

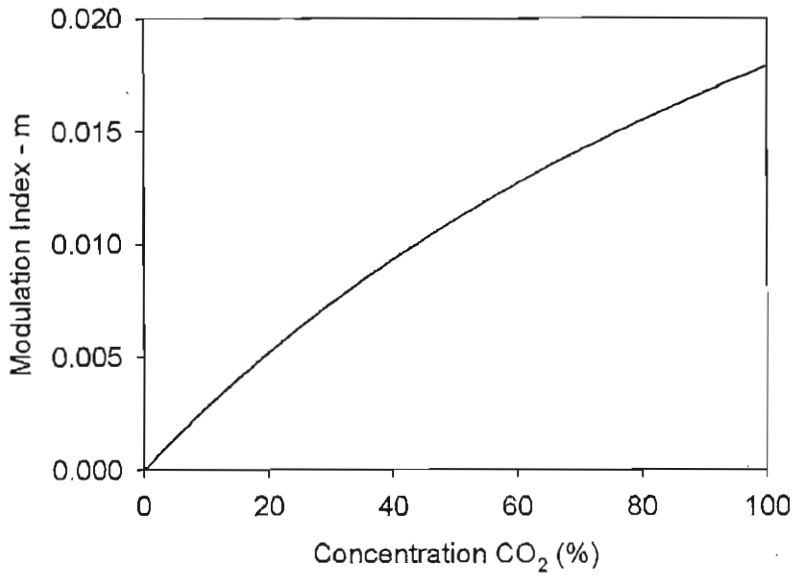

FIGURE 5.7: Modulation Index (m) as a function of CO_2 gas concentration (%vol/vol) in the measurement cell. The reference and measurement gas cells were modelled as being of 26 cm length and the reference cell was modelled as containing a mixture CO_2 and air at 20°C and at a total pressure of 1 bar. An optical bandpass filter possessing a FWHM bandwidth of 175 nm at a centre wavelength of 2.004 μm was modelled.

5.6 The Effect of Changing Optical Spectra from the Optical Sources

Any common mode variation in the emission spectrum of the light sources may be represented by a change in the centre wavelength or bandwidth of the optical bandpass filter. However, the centre wavelength or bandwidth of either source may change independently. Thus, this method of correlation spectroscopy was modelled using two separate light sources, each possessing a Gaussian shaped spectral emission, and no optical bandpass filter. Figure 5.8 shows the effect of holding the emission spectrum of optical source 1 constant, while changing the centre wavelength of the spectral emission from optical source 2. This shows that, with the conditions specified in the caption to Figure 5.8, the magnitude of the modulation index tends to decrease from a maximum of 0.018 and, if the emission spectrum from the two sources tends not to overlap, a modulation index in antiphase to the usual modulation would be observed.

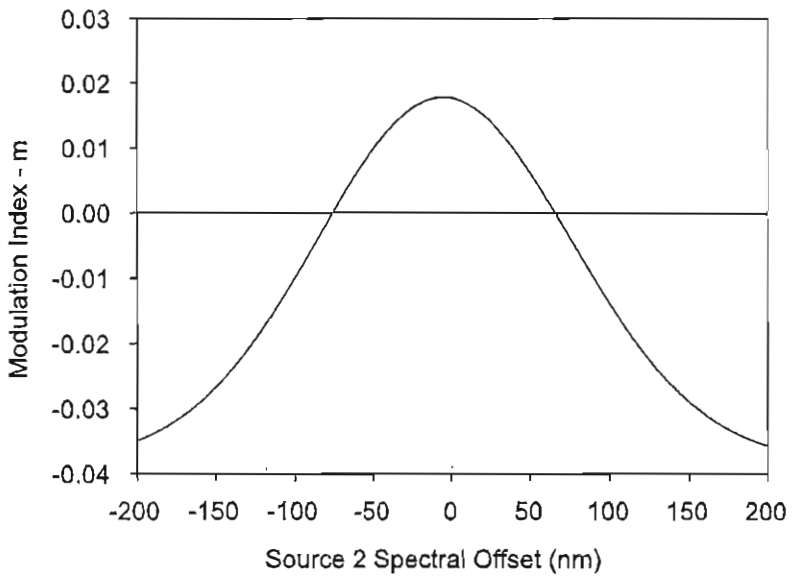

FIGURE 5.8: Modulation Index (m) as a function of the offset of the spectral emission from optical source 2. The two optical light sources were modelled as possessing Gaussian shaped emission spectra of a FWHM bandwidth of 175 nm. The emission spectrum from source 1 was centred at 2.004 μm. No optical bandpass filter was present. The reference and measurement gas cells were modelled as being of 26 cm length and the reference cell was modelled as containing 100% CO_2 gas at 20°C and at a total pressure of 1 bar.

The correlation spectroscopy system was also modelled with an optical bandpass filter, with a Gaussian shaped transmission function, present. The result of this simulation is shown in Figure 5.9.

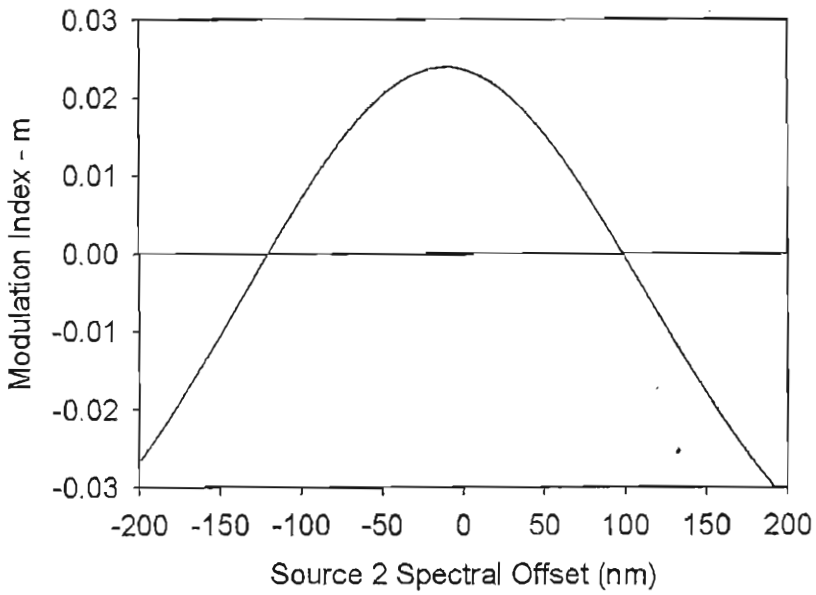

FIGURE 5.9: Modulation Index (m) as a function of the offset of the spectral emission from optical source 2. The two optical light sources were modelled as possessing Gaussian shaped emission spectra of a FWHM bandwidth of 175 nm. The emission spectrum from source 1 was centred at 2.004 μm. An optical bandpass filter was included in the simulation and was Gaussian shaped and was centred at 2.004 μm. The reference and measurement gas cells were modelled as being of 26 cm length and the reference cell was modelled as containing 100% CO_2 gas at 20°C and at a total pressure of 1 bar.

Due to the combined effect of having both the emission function of the light sources and the transmission function of the bandpass filter Gaussian shaped, a narrower FWHM bandwidth results. This results in a higher result for the maximum modulation index of 0.021. Otherwise the graph can be seen to exhibit a similar trend to where there was no optical bandpass filter present, ie. the modulation index decreased as the peak wavelength of the emission of source 2 moves away from that of optical source 1.

5.7 The Effect of Changing Measurement Gas Cell Pressure

The effects of gas pressure variations, in the measurement gas cell, on the modulation index are now considered. The measurement gas cell was modelled as experiencing a change in pressure, but the temperature of the measurement gas cell was modelled as remaining constant. The pressure and temperature of the reference gas cell were also modelled as remaining constant. Figure 5.10 shows the result of this simulation, which indicates that a variation of $+/-0.1$ bar would lead to a $+5.22\%/-5.69\%$ error in the received modulation index. This suggests an average dependence of the modulation index on the measurement gas cell pressure, with the conditions shown, of 0.6 % $mbar^{-1}$.

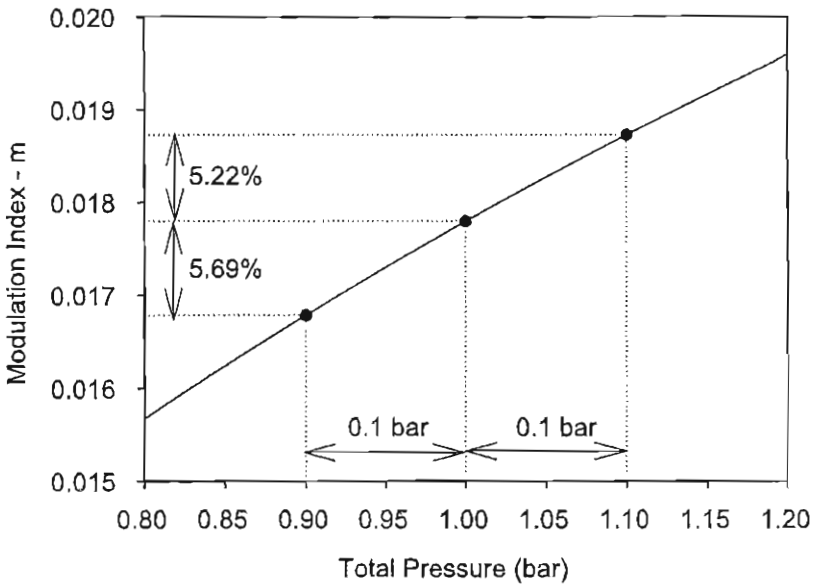

FIGURE 5.10: Simulated variation of modulation index with the pressure of the measurement gas cell, both cells were modelled as containing 100% CO_2 at 1 bar and to be 26 cm long. The reference gas cell was modelled as being at a temperature of 20°C and the optical bandpass filter was modelled as having a centre wavelength of 2.004 μm and a bandwidth of 175 nm.

5.8 The Effect of Varying Measurement Cell Gas Temperature

The effects of changing the temperature of the measurement cell were modelled over a range of temperatures from 10°C to 30°C. The concentration and pressure of the CO_2 gas in both gas cells were modelled as remaining constant, at 100% and 1 bar, respectively. The temperature of CO_2 gas in the reference cell was modelled as remaining constant at 20°C. As before, the optical bandpass filter was modelled as being centred

at 2.004 μm and with a bandwidth of 175 nm. Figure 5.11 shows the result of this simulation, which suggests that a variation of temperature, between 10°C and 30°C, would lead to +2.45%/-2.47% error in the measurement compared to a measurement gas cell temperature of 20°C. The simulation also suggests that the modulation index decreases with increasing measurement temperature and that the dependence of modulation index on measurement gas cell temperature is 0.2 %°C^{-1}.

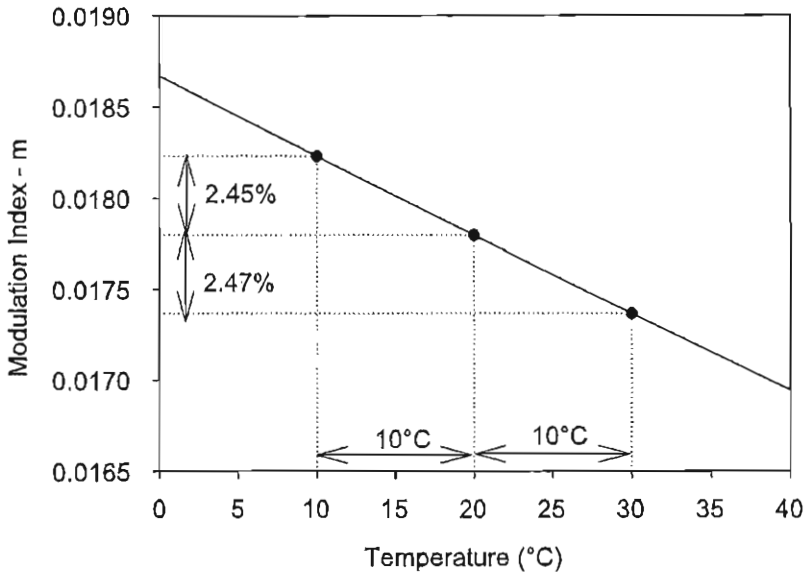

FIGURE 5.11: Simulated variation of modulation index with various gas temperatures of the measurement gas cell. Both cells were modelled as containing 100% CO_2 gas at 1 bar and as being 26 cm in length. The reference gas cell was modelled at a gas temperature of 20°C and the optical bandpass filter was modelled as having a centre wavelength of 2.004 μm and a bandwidth of 175 nm.

5.9 The Effect of Changing Optical Bandpass Filter Bandwidth when there is H_2O Vapour in the Measurement Gas Cell

Figure 5.12 shows the Hitran absorption spectrum of 2.3% H_2O vapour around 2 μm (according to British Standard 1339 [39] saturated air holds 2.3% H_2O (volume/volume) at 20°C). The figure shows that, while there is no significant absorption from H_2O within the band used for measurement, some absorption does lie at the lower range of wavelengths. Thus, some interference may be expected with the use of wider bandwidth filters.

With the measurement gas cell containing H_2O saturated N_2 gas, Figure 5.12 shows the effect, on the modulation index, of increasing the bandwidth of the optical bandpass filter. Figure 5.12 shows that as the bandwidth of the filter increases the effect

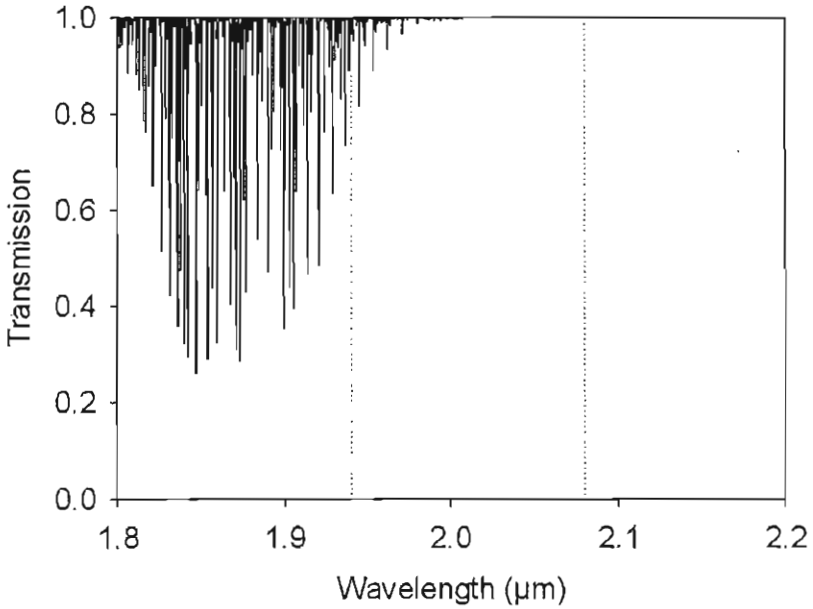

FIGURE 5.12: Transmission of 2.3% H_2O gas over a 26 cm path length at 20°C and a total pressure of 1 bar (transmission data was obtained from Hitran database). The dotted vertical lines show the spectral range used for the CO_2 spectra.

on modulation index of the contaminant gas also increases and also, the modulation index becomes a negative value at larger bandwidths of the optical bandpass filter. Also the graph shows that, for the conditions specified, with an optical bandpass filter bandwidth of 25 nm the modulation index would be insensitive to water vapour. This is because the proportion of overlapping and non-overlapping absorption lines results in zero modulation index sensitivity to H_2O vapour.

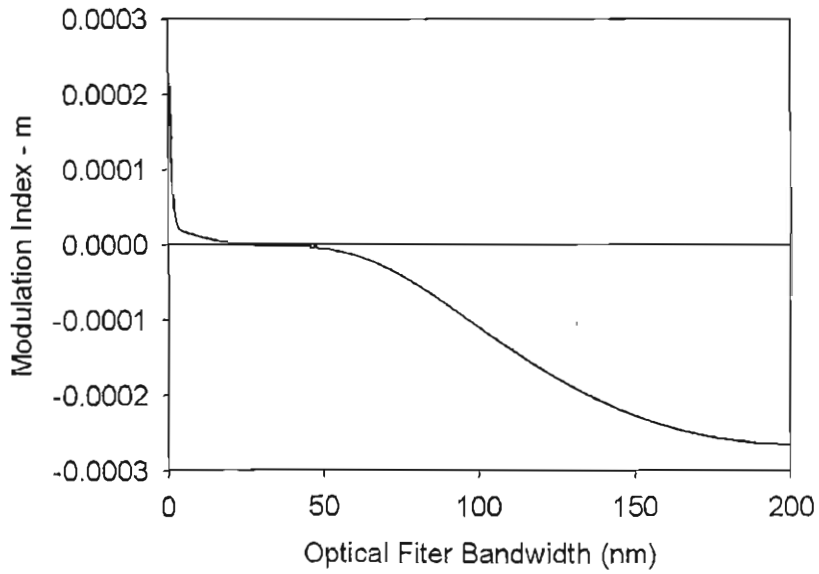

FIGURE 5.13: Variation of the modulation index with varying bandwidth of the optical bandpass filter. The measurement gas cell was modelled as containing H_2O vapour saturated N_2 gas (approx 2.3% H_2O).

5.10 Method for Improving System Sensitivity to CO_2 by the Pressurisation of the Reference Gas Cell

In this section the possibility of increasing the sensitivity of a correlation spectroscopy system by increasing the pressure of the reference gas cell is discussed. The idea has been investigated previously by Herget *et al.* [40]. It was qualitively identified that while an increase in modulation index would result, due to the effect of line broadening due to the increased reference gas pressure, there would be the associated drawback that cross-contamination from the mainly non-overlapping absorption spectra of a contaminant gas would also increase.

The effects of increasing reference gas cell pressure can be quantified and a factor can be introduced that is a measure of this sensitivity enhancement. This has been named the 'improvement factor'. The variation of this improvement factor with measurement gas cell concentration is also described.

Increasing the pressure of a gas cell containing solely CO_2 has the following effects:

1. Further increasing the concentration (partial pressure) beyond 1 bar.
2. Increasing the effects of collision broadening on the Voigt lineshape that was used for these simulations.

This suggests that the improvement of the modulation index would continue to follow the trend of increasing measurement gas cell concentration that was described in Section 3.4.4, Chapter 3, and then with application to the detection of CO_2 gas in Section 5.5 of this chapter.

Figure 5.14 shows the simulated rise in modulation index that may be achieved by raising the pressure of the reference gas cell to 6 bar. The improvement factor, as defined above, is the ratio of the modulation index attained with the reference gas cell at 6 bar compared to that attained with the reference gas cell at 1 bar. This is shown to be 1.999 for the case where the measurement gas cell contains 100% CO_2 target gas. Figure 5.14 shows that the graphical response of modulation index versus increasing pressure of the reference gas cell will follow a similar trend, to that with increasing gas concentration of the measurement gas cell.

5.10.1 Change of Improvement Factor with Changing Measurement Gas Cell Concentration

While in the previous section it was shown that the improvement factor attained with a reference gas cell pressure increase to 6 bar and 100% concentration of CO_2 gas in the

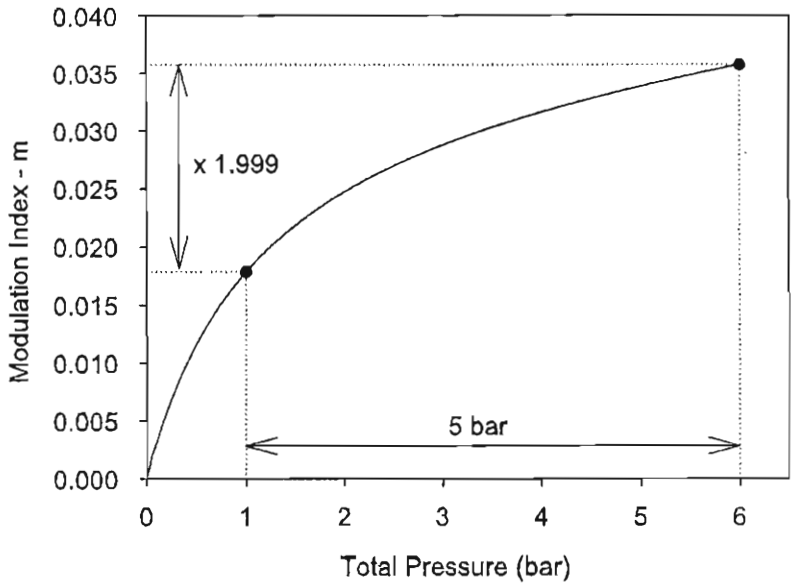

FIGURE 5.14: Potential improvement of a Correlation Spectroscopy system Modulation Index (m) by the pressurisation of the reference gas cell. The reference gas cell was modelled as being varied between 0 bar and 6 bar at a temperature of 20°C and at a length of 26 cm. The measurement gas cell was modelled as containing 100% CO_2 gas at a pressure of 1 bar and as being of 26 cm length. The optical bandpass filter was modelled as having a centre wavelength of 2.004 μm and a FWHM bandwidth of 175 nm.

measurement gas cell was 1.999, this does not remain constant with decreasing measurement gas cell CO_2 concentration (mixed with air). Figure 5.15 shows the simulated rise in modulation index with increasing reference gas cell pressure at various measurement gas cell concentrations of CO_2.

Table 5.1 shows the improvement factors associated with these measurement gas cell CO_2 concentrations; clearly the improvement factor decreases with decreasing measurement gas cell concentration.

Concentration	Improvement Factor
100%	1.999
80%	1.950
60%	1.898
40%	1.845
20%	1.788

TABLE 5.1: The effect of measurement gas cell CO_2 concentration on the improvement factor.

This effect of decreasing measurement gas cell CO_2 concentration on the improvement factor is shown in Figure 5.16. Here, the CO_2 concentration is shown on a logarithmic scale, and the modulation index is shown to decay asymptotically towards 1.731. The fact that the response decays towards a constant value with decreasing measurement cell CO_2 concentration also serves to confirm the previous assertion that the concentration

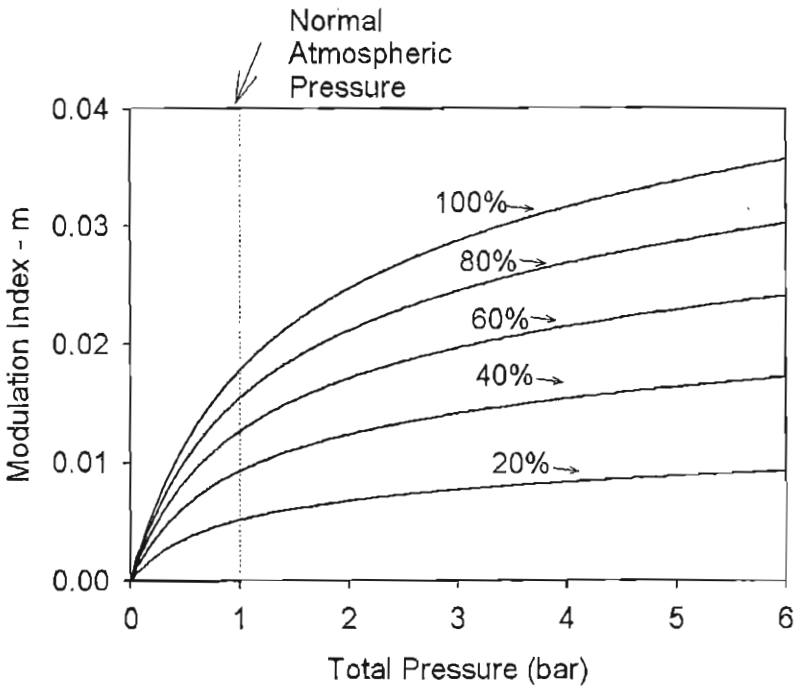

FIGURE 5.15: Simulated improvement of a correlation spectroscopy system modulation index (m), at selected measurement gas cell CO_2 concentrations, versus the reference gas cell CO_2 pressure. The reference gas cell was modelled as being varied between 0 bar and 6 bar. Both gas cells were modelled at a temperature of 20°C and as being of 26 cm in length. The measurement gas cell was modelled as containing 100% CO_2 at a pressure of 1 bar.

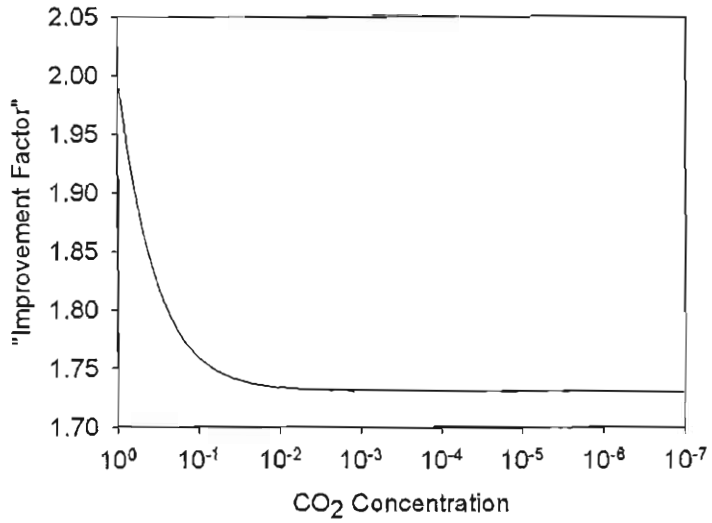

FIGURE 5.16: Modulation index (m), at different measurement gas cell concentrations shown on a logarithmic scale. The measurement cell was modelled as being at a pressure of 1 bar and as being 26 cm long. The CO_2 containing reference gas cell, held at 20°C, was at a pressure of 6 bar and was also 26 cm long, and the optical bandpass filter had a centre wavelength of 2.004 μm and a FWHM bandwidth of 175 nm.

response at low concentrations starts as a near-linear response (see Section 3.4.4, Chapter 3, and Section 5.5 of this chapter).

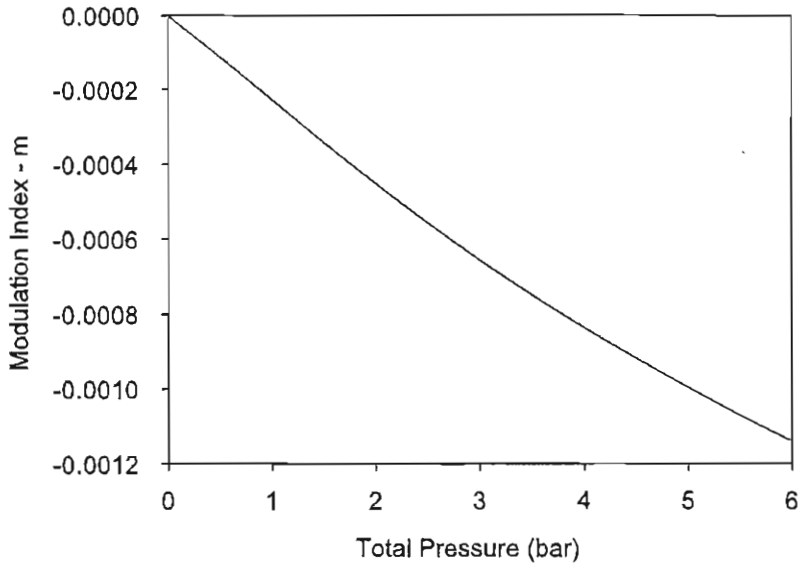

FIGURE 5.17: Change in modulation index as the reference gas cell CO_2 pressure is increased. The measurement gas cell was simulated as containing a mixture of 2.3% H_2O vapour and air at a total pressure of 1 bar and was modelled as being of length 26 cm. The reference gas cell, modelled as being held at 20°C, as being swept between pressures of 0.5 bar up to 6 bar and was also modelled as being of length 26 cm. The optical bandpass filter was modelled as having a centre wavelength of 2.004 μm and a bandwidth of 175 nm.

5.10.2 The Change of Modulation Index due to a Contaminant Gas (H_2O Vapour)

As was mentioned in the introduction, the cross-talk in measurements due to a contaminant gas would be expected to increase with increasing reference gas cell CO_2 pressure due to the line broadening effects. The transmission spectrum of 2.3% H_2O vapour around 2 μm (according to British Standard 1339 [39], saturated air holds 2.3% H_2O (volume/volume) at 20°C) was previously shown in Figure 5.12. Figure 5.17 shows the results of a simulation carried out to demonstrate this. Figure 5.17 shows that as the CO_2 pressure of the reference gas cell is increased, the cross-talk due to the contaminant gas (H_2O vapour) increases and the observed modulation index is negative. In particular, with the reference gas cell at a CO_2 gas pressure of 1 bar and the measurement gas cell containing 2.3% H_2O vapour, a simulated modulation index of -2.154×10^{-4} is obtained. By comparison the modulation index that would be attained with a reference gas cell pressure of 6 bar is -1.140×10^{-3}. This shows that the modulation index, due to H_2O vapour and the pressurisation of the reference gas cell, increases at a rate of approximately -2×10^{-4} bar^{-1}. In conclusion, by the pressurisation of the reference gas cell, the modulation index will increase by a factor of 2 at 100% measurement gas cell CO_2 concentration, but the response to 2.3% H_2O vapour has also increased by a factor of 5. This factor relating the increased sensitivity to a contaminant gas will also change with changing measurement gas cell CO_2 and H_2O concentrations.

5.11 Simulation Results for the Detection of Methane

5.11.1 Introduction

Knowledge of the concentration of methane gas (CH_4) is required for number of applications, which include the monitoring of its concentration in the composition of natural gas, the detection of its concentration in the atmosphere (due to its role as a greenhouse gas) in addition to several medical applications, one of which is that its concentration in human breath indicates the function of the human digestive system.

CH_4 possesses an absorption band at approximately 1.6 μm - 1.8 μm. The most intense of these is the $3v_2$ absorption band. Other absorption band contributions are present at this spectral interval, some of which have been theoretically identified and others which have been solely recorded from laboratory measurements. The data that were used for these simulations were obtained from the 2001 update to the Hitran 2000 database. Data dating from 1992 were included in the database for this spectral interval, which was based upon experimental observations by Brown *et al.* [41]. Modelled data do exist for the spectral interval 4800 cm^{-1} - 6250 cm^{-1} (2.083 μm - 1.600 μm), which includes a tetradecad caused by a Fermi-resonance, comprised of fourteen bands giving rise to interactions with the ground state [42]. However, these data were not incorporated in the 2001 update to the Hitran database due to uncertainties with the modelled parameters.

5.11.2 Simulation Results

The simulation results relating to the detection of CH_4 gas are shown in the same format as were the results for the detection of CO_2 gas, and the conclusion relates to the similarities and the contrasts between the results for the two gases.

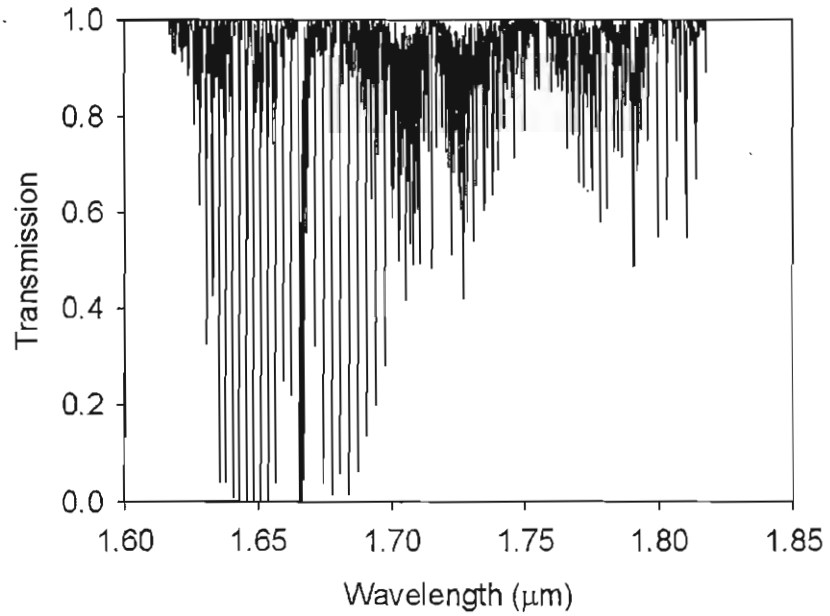

FIGURE 5.18: Transmission of 100% CH_4 gas over a 26 cm path length at 20°C and a total pressure of 1 bar (transmission data was obtained from Hitran database).

Figure 5.18 shows the transmission of CH_4 gas between 1.60 μm and 1.85 μm. The simulated modulation index dependence on the centre wavelength of the optical bandpass filter with a narrow 2 nm bandwidth is shown in Figure 5.19.

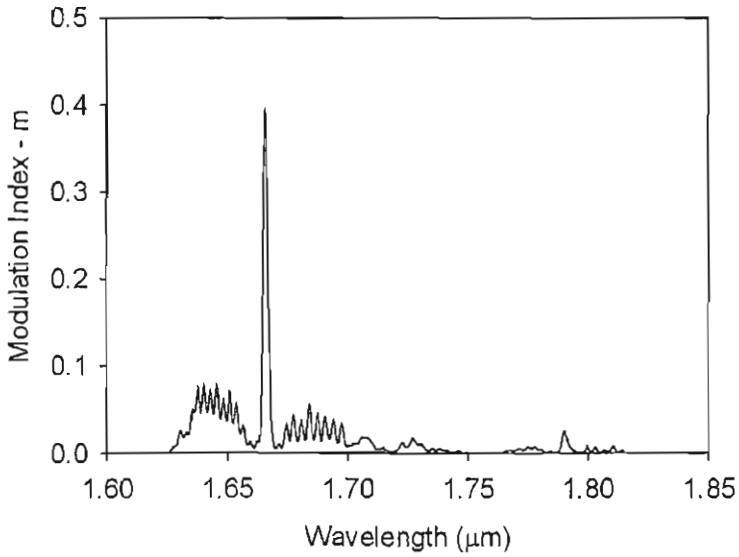

FIGURE 5.19: Modulation Index (m), as a function of filter centre wavelength. The reference and measurement gas cells were modelled as both containing 100% CH_4, being 26 cm long, at a temperature of 20°C and at a total pressure of 1 bar. The transmission spectrum of the optical bandpass filter is modelled as being Gaussian shaped and possessing a 2 nm FWHM bandwidth.

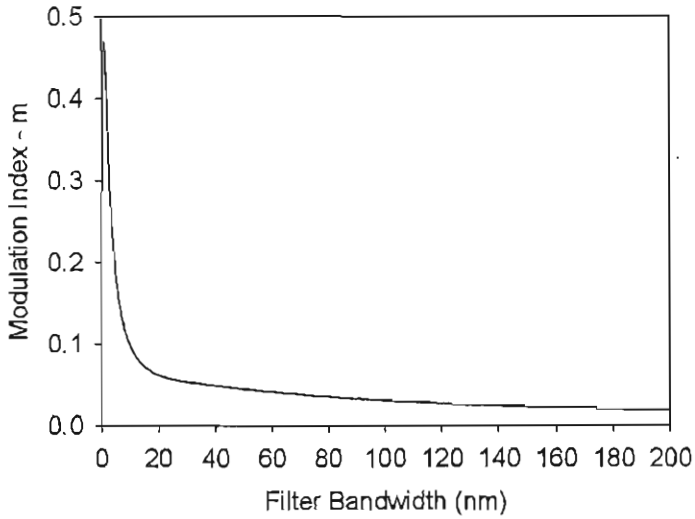

FIGURE 5.20: Modulation Index (m) versus optical bandpass filter FWHM bandwidth, the 26 cm long reference and measurement cells are modelled as both containing 100% CH_4 gas, at 20°C and at a total pressure of 1 bar. The Gaussian shaped optical bandpass filter was modelled as having a centre wavelength of 1.666 μm.

Figure 5.20 shows the variation of the modulation index with the bandwidth of the optical bandpass filter, centred at 1.666 μm. The effect on the modulation index of changing both the centre wavelength and bandwidth of the optical bandpass filter is shown in Figure 5.21.

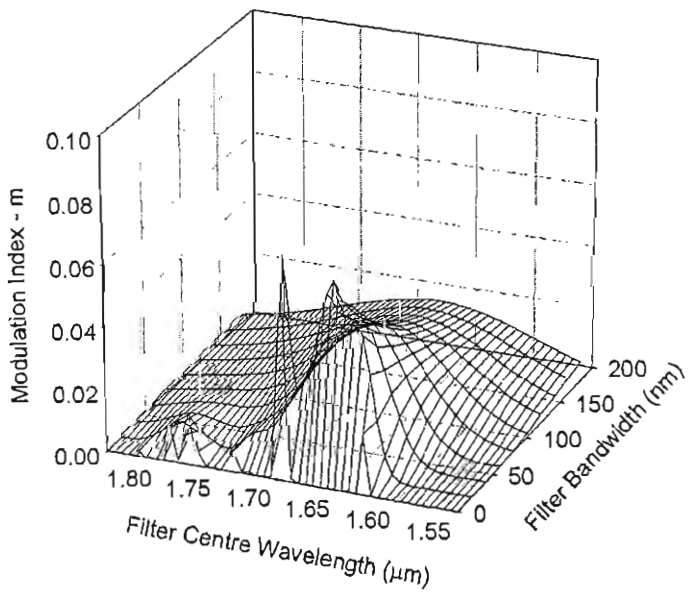

FIGURE 5.21: Modulation Index (m) as a 3-D function of the centre wavelength and FWHM bandwidth of the optical bandpass filter. The data-set was undersampled in order to aid visualisation. The 26 cm long reference and measurement cells were modelled as containing 100% CH_4 gas at a temperature 20°C and at a total pressure of 1 bar.

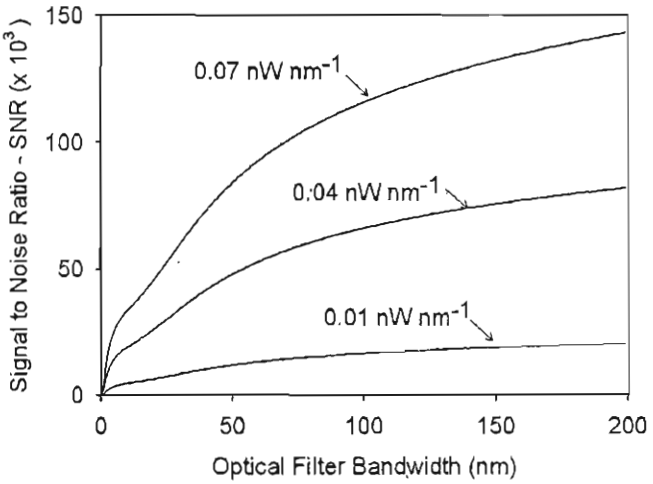

FIGURE 5.22: Simulated variation in SNR at different source power intensities, from 0.01 nW nm^{-1} to 0.07 nW nm^{-1} as the bandwidth of the Gaussian shaped system bandpass optical filter (centred at 1.666 μm) is increased. The reference and measurement gas cells were modelled as being of 26 cm length and containing 100% CH_4 gas at 20°C and a total pressure of 1 bar. The time constant of the measurement signal low-pass filter was 10 seconds.

Figure 5.22 shows the results from simulation of the variation of the SNR in the measurement at the measurement detector at three optical spectral intensities. The combined effect of changing both the centre wavelength and bandwidth of the optical bandpass filter on the SNR is shown in Figure 5.23.

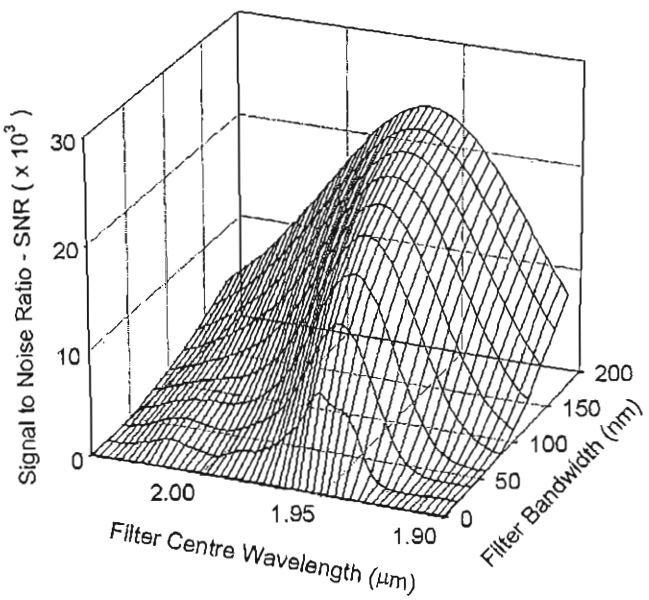

FIGURE 5.23: Expected SNR in measurements as a function of system bandpass filter centre wavelength and bandwidth with a mean optical power incident upon the reference detector of 0.01 nW nm^{-1}. The reference and measurement gas cells are of 1 m length and contain only CH_4 at 20°C and a total pressure of 1 bar. The time constant of the measurement signal low-pass filter was 10 seconds.

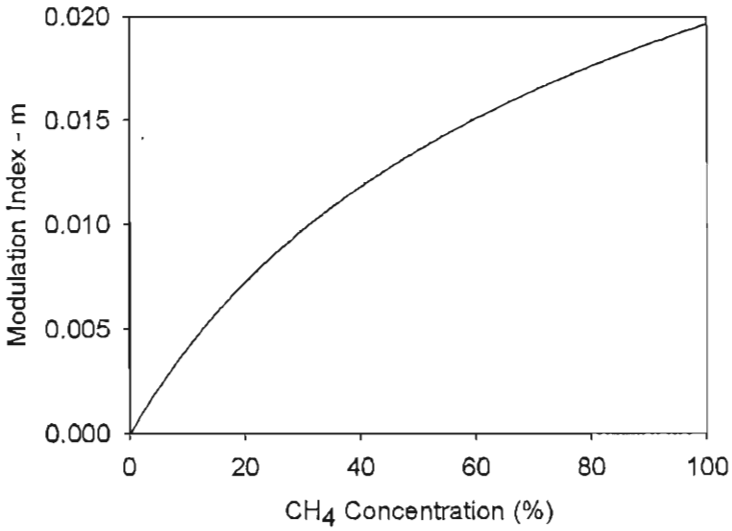

FIGURE 5.24: Modulation Index (m) as a function of CH_4 concentration (%vol/vol) in the measurement cell. The reference and measurement cells were modelled as being of 1m length and the reference cell was modelled as containing 100% CH_4 at 20°C, at a total pressure of 1 bar. An optical bandpass filter having a bandwidth of 100 nm at a centre wavelength of 1.666 μm was modelled.

The simulated effect of changing the measurement cell CH_4 gas concentration is shown in Figure 5.24. Figure 5.25 shows the simulated effect of changing the CH_4 gas pressure of the measurement gas cell.

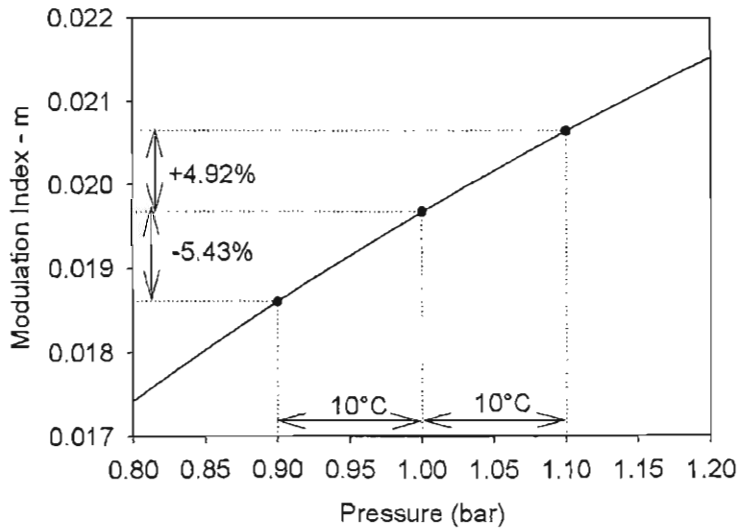

FIGURE 5.25: Expected variation of modulation index with the total pressure of the measurement cell, assuming both cells contained 100% CH_4 at 1 bar and were 26 cm long. The reference cell was simulated as being held at 20°C and the optical bandpass filter was simulated as having a centre wavelength of 1.666 μm and a bandwidth of 175 nm.

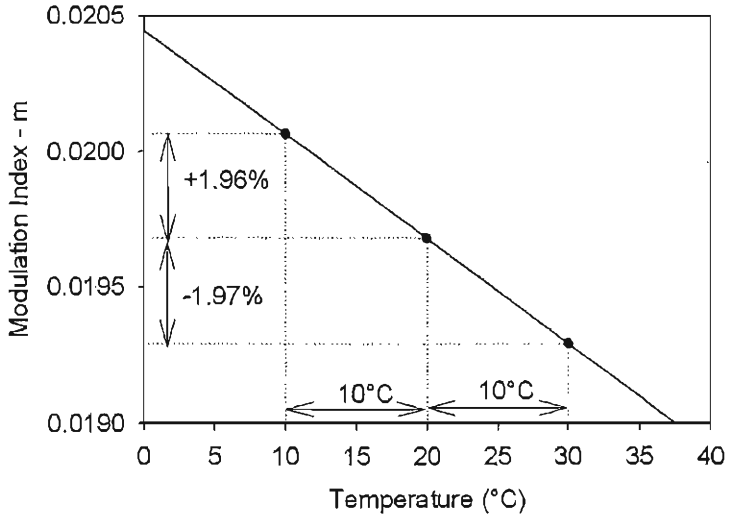

FIGURE 5.26: Expected variation of modulation index with temperature of the measurement cell, both cells were modelled as containing 100% CH_4 at 1 bar and as being 26 cm long. It was modelled that the reference cell was held at 20°C and that the optical bandpass filter had a centre wavelength of 1.666 μm and a bandwidth of 175 nm.

The results from the simulation, using the Hitran data, showing the simulated variation of the modulation index with solely the CH_4 gas temperature of the measurement gas changing is shown in Figure 5.26.

5.12 Simulation Results for the Detection of O_2

5.12.1 Introduction

The detection of Oxygen (O_2) is required for several industrial and medical applications. Knowledge of the concentration of O_2 gas can also be of use for atmospheric scientists.

The absorption of O_2 used for these simulations is the Fraunhoffer A-band absorption, also referred to in the spectroscopic literature as $b^1\sum_g^+ - X^3\sum_g^+$. The data that are included in the Hitran 2000 database were derived from measurements made by Brown and Plymate [43].

5.12.2 Summary of Simulation Results

The transmission of O_2 gas, simulations deriving the modulation index and its dependence on changes in concentration, pressure and temperature are now presented. Simulation results showing the SNR characteristics are also given. With O_2 gas an optical bandpass filter bandwidth of 2 nm is used for the SNR calculations, due to the narrower bandwidth of the absorption line spectrum at this wavelength.

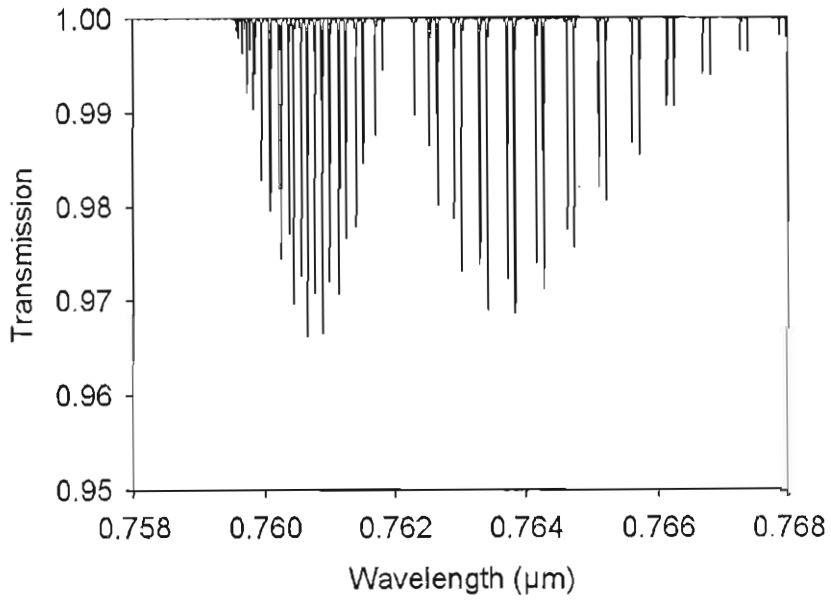

FIGURE 5.27: Transmission spectrum of 100% O_2 gas over a 26 cm path length at 20°C and at a total pressure of 1 bar (transmission data were obtained from Hitran database).

Figure 5.27 shows the transmission of O_2 gas between 0.758 μm and 0.768 μm. The simulated modulation index dependence on the centre wavelength of the optical bandpass filter, with a narrow 2 nm bandwidth, is shown in Figure 5.28.

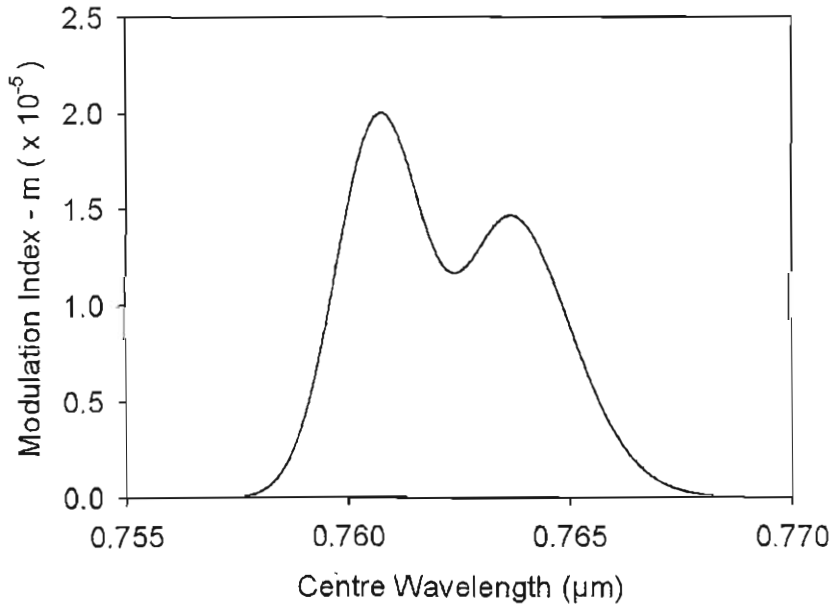

FIGURE 5.28: Modulation Index (m), as a function of the optical bandpass filter centre wavelength, both reference and measurement cells were modelled as containing 100% O_2, at a path length of 26 cm length at 20°C and at a total pressure of 1 bar. The transmission spectrum of the optical bandpass filter was modelled as possessing a 2 nm FWHM bandwidth.

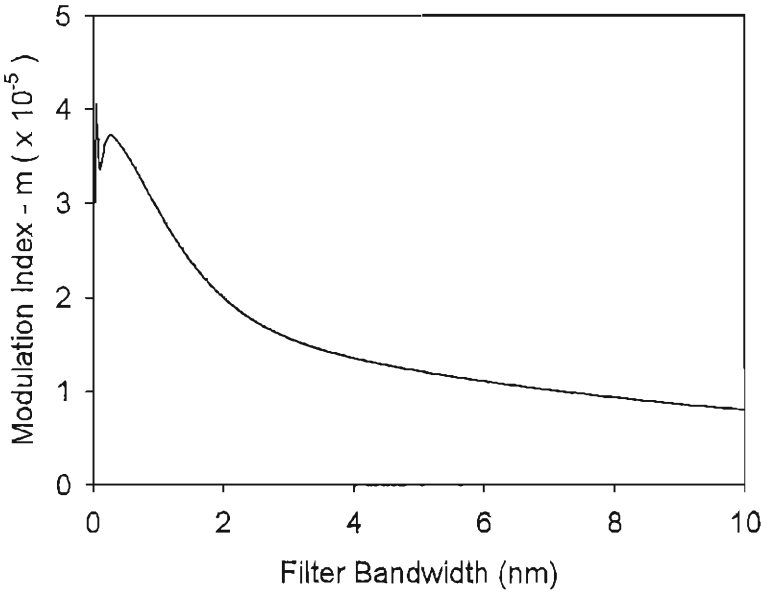

FIGURE 5.29: Modulation Index (m) versus the optical bandpass filter FWHM bandwidth. The 26 cm long reference and measurement cells were modelled as both containing 100% O_2 gas at 20°C and at a total pressure of 1 bar. The Gaussian shaped optical bandpass filter was modelled as having a centre wavelength of 0.761 μm. The graph is under-sampled to aid visualisation.

Figure 5.29 shows the variation of the modulation index with the bandwidth of the optical bandpass filter, centred at 0.761 μm. The combined effect of changing both the centre wavelength and bandwidth of the optical bandpass filter is shown in Figure 5.30.

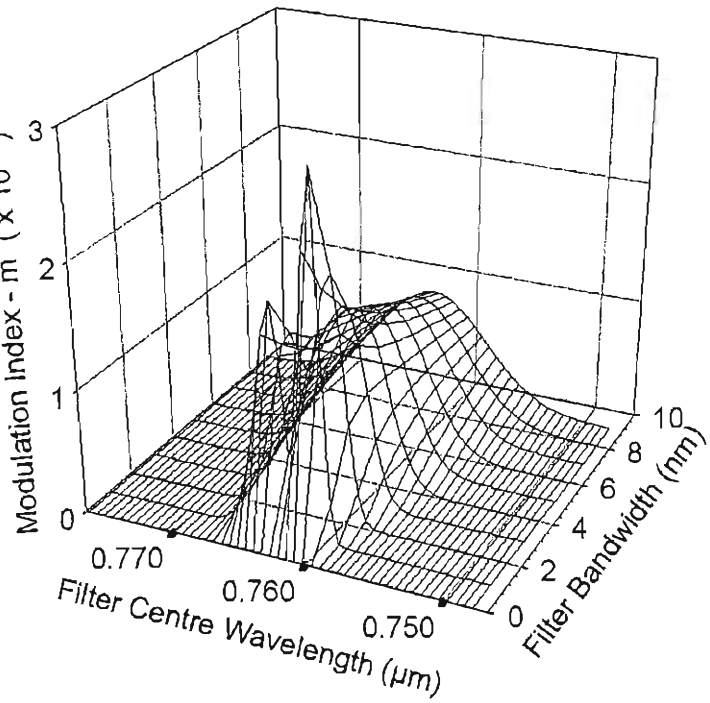

FIGURE 5.30: A 3-D representation of Modulation Index (m) as a function of the optical bandpass filter centre wavelength and FWHM bandwidth. The 26 cm long reference and measurement cells were modelled as containing 100% O_2 gas at 20°C and at a total pressure of 1 bar.

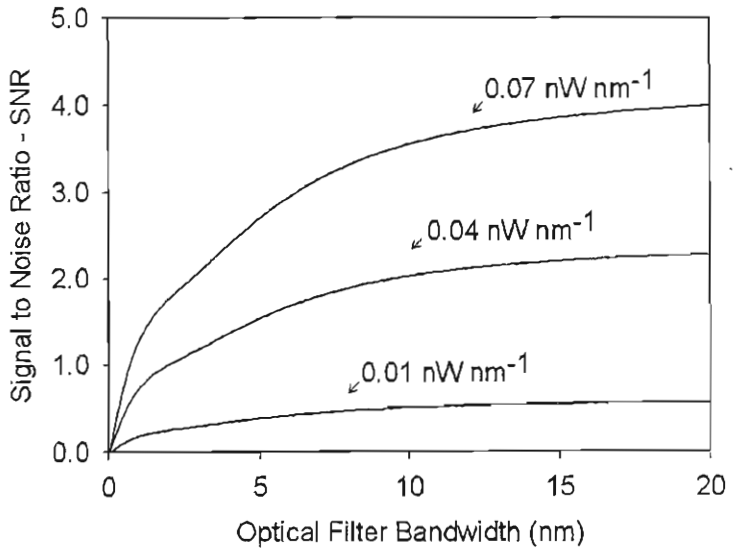

FIGURE 5.31: Simulated variation in SNR at different source power intensities, from 0.01 nW nm^{-1} to 0.07 nW nm^{-1} as the bandwidth of the Gaussian shaped system bandpass optical filter (centred at 0.761 μm) is increased. The reference and measurement gas cells were modelled as being of 26 cm length and containing 100% O_2 gas at 20°C and at a total pressure of 1 bar. The time constant of the measurement low pass filter was 10 seconds.

Figure 5.31 shows the simulation of the variation of the SNR in the measurement at the measurement detector at three optical spectral intensities. The combined effect of changing both the centre wavelength and bandwidth of the optical bandpass filter on the SNR is shown in Figure 5.32.

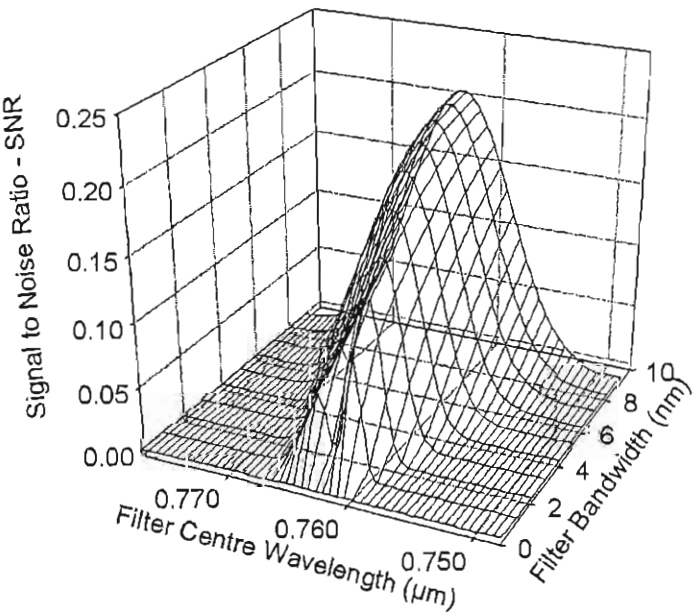

FIGURE 5.32: Simulated SNR in measurement signal as a function of the optical bandpass filter centre wavelength and bandwidth, with a mean optical power incident upon the reference detector of 0.01 nW nm^{-1}. The reference and measurement gas cells were modelled as being of 26 cm length and containing 100% O_2 at 20°C and at a total pressure of 1 bar. The time constant of the measurement low pass filter was 10 seconds. The graph is under-sampled to aid visualisation.

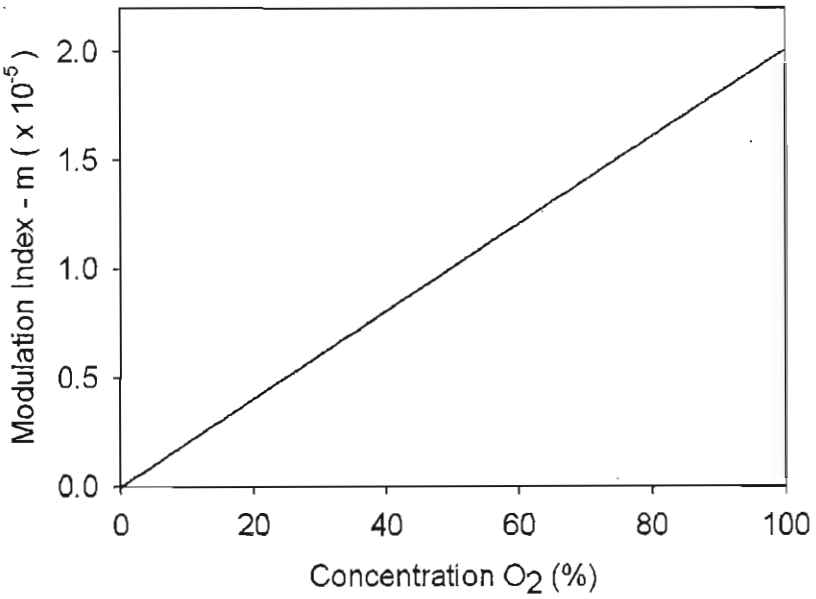

FIGURE 5.33: Modulation Index (m) as a function of O_2 concentration (%vol/vol) in the measurement gas cell. The reference and measurement gas cells were modelled as being 26 cm in length and the reference gas cell was modelled as containing 100% O_2 gas at 20°C and at a pressure of 1 bar. An optical bandpass filter having a FWHM bandwidth of 2 nm at a centre wavelength of 0.761 μm was modelled.

The simulated effect of changing the measurement cell O_2 gas concentration is shown in Figure 5.33. Figure 5.34 shows the simulated effect of changing the O_2 gas pressure of the measurement gas cell.

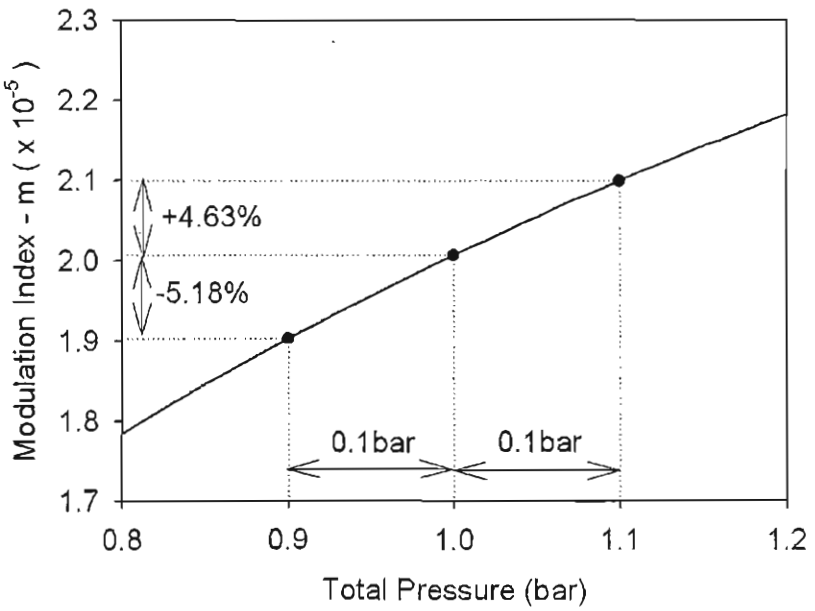

FIGURE 5.34: Simulated variation of modulation index with the total pressure of the measurement cell. Both the cells were modelled as containing 100% O_2 gas at a total pressure of 1 bar and as being 26 cm in length. The reference gas cell was modelled as being at 20°C and the optical bandpass filter was modelled as having a centre wavelength of 0.761 μm and a FWHM bandwidth of 2 nm.

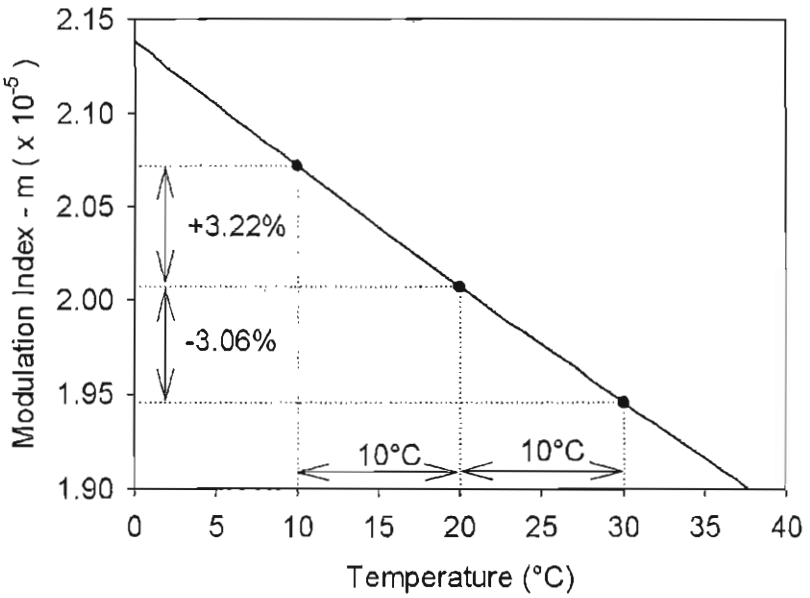

FIGURE 5.35: Simulated variation of modulation index with the temperature of the measurement cell. Both cells were modelled as containing 100% O_2 at 1 bar and being 26 cm long. The reference gas cell was modelled as being at 20°C and the optical bandpass filter was modelled as having a centre wavelength of 0.761 μm and a FWHM bandwidth of 2 nm.

The results of a simulation using the Hitran data that show the effect of the CH_4 gas temperature in the measurement cell on the modulation index are presented in Figure 5.35.

5.13 Conclusions

This chapter contained the results from simulations that modelled the response of a correlation spectroscopy gas detection system, with a particular emphasis on CO_2 gas. It was observed that the trend of modulation index versus the centre wavelength of the optical bandpass filter, at a narrow 2 nm filter bandwidth, is closely related to a convolved (or "smoothed") version of the original CO_2 absorption spectrum. It was shown that as the bandwidth of the optical bandpass filter was increased the modulation index decreased at wider filter bandwidths. However, when signal to noise considerations were included, it was shown that the optimal bandwidths for operation of the correlation spectroscopy system was with a significantly wider optical bandpass filter bandwidth.

A method of improving the correlation spectroscopy system sensitivity by increasing the pressure of the reference gas cell was also analysed. It was shown that by increasing the CO_2 gas pressure of the reference gas cell to 6 bar an improvement in the modulation index of 1.999 could be attained, if there was 100% CO_2 gas in the measurement gas cell. It was shown how the improvement reduced with decreasing measurement gas cell CO_2 concentration and this improvement was accompanied by an increasing response

to a contaminant gas in the measurement gas cell. This was due to wider absorption lines principally due to collision broadening effects. The simulated rate of increase of the effect of cross-talk to 2.3% H_2O was found to be twice that of the response to CO_2 target gas.

A summary of the simulation results relating to the detection of CO_2, CH_4 and O_2 is given in Table 5.2. In the table, the minimum detectable gas concentrations relate to a received spectral power of 0.01 nW nm^{-1} at the measurement detector. This was chosen because it approximates to the received power in the CO_2 system analysed experimentally in the following chapter. At wavelengths smaller than 2 μm optical sources typically have a significantly more intense emission spectrum leading to a significantly lower detection limit. The simulated results relating to the dependence of the modulation index on the temperature variation of the measurement gas cell and the introduction water vapour into the measurement gas cell were found to differ considerably from the experimental findings for the CO_2 sensor. These are discussed in the following chapter.

Gas	CO_2	CH_4	O_2
Centre Wavelength	2.004 μm	1.666 μm	0.761 μm
Filter Bandwidth	175 nm	175 nm	2 nm
Modulation index at 100% measurement gas cell concentration	0.018	0.020	2×10^{-5}
Pressure Dependence (0.9 - 1.1 bar)	0.6 % $mbar^{-1}$	0.5 % $mbar^{-1}$	0.5 % $mbar^{-1}$
Temperature dependence	0.2 %°C^{-1}	0.2 %°C^{-1}	0.3 %°C^{-1}
Minimum detectable gas concentration (using a received power of 0.01 nW nm^{-1})	0.01%	0.01%	400%

TABLE 5.2: Summary of results for the detection of CO_2, CH_4 and O_2 gases.

Chapter 6

Experimental Results and Comparison with Simulation

6.1 Introduction

In this chapter a description of experiments is presented that were carried out to verify the operation of a CO_2 gas correlation spectroscopy detection system. These experiments had the objective of establishing the operation of a CO_2 correlation spectroscopy gas detection system with regard to varying CO_2 concentration in the measurement gas cell, the pressurisation of the reference gas cell, temperature variations of CO_2 gas in the measurement gas cell, and the cross-sensitivity to a contaminant gas (water vapour). A description of the equipment used, the procedures followed in the carrying out of the experiments, the results from the experiments and an analysis and discussion of these results are included. The method of increasing the modulation index by increasing the reference gas cell pressure, hence increasing the system sensitivity, is also examined.

The power loss budgets and the noise present in the experiments are analysed in Chapter 7.

6.2 The Experimental Setup

The experimental CO_2 correlation spectroscopy gas detection system that was used consisted of optical, electronic/computer control and gas handling segments. The system topology of the experimental system is shown in Figure 6.1 and is described in the following sections.

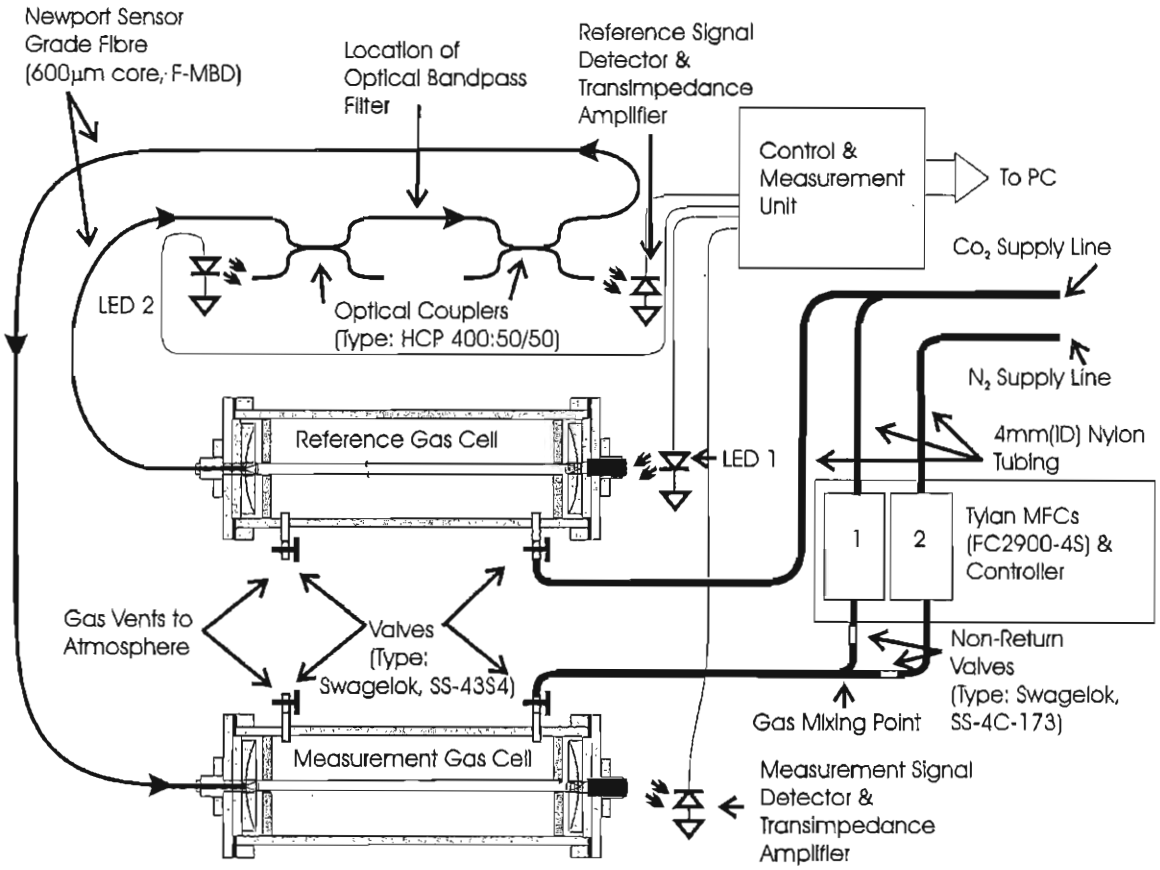

FIGURE 6.1: The topology of the correlation spectroscopy used for the experimental investigations.

6.2.1 Optical and Electronic System

The light sources used in this system were two GaSb-InAs LED20 2 μm LEDs in TO-5 packages with integrated Peltier coolers. These were manufactured by IBSG, based in St. Petersburg, Russia. In order to obtain a higher spectral power output, these LEDs were cooled, so that the in-built temperature dependent resistor exhibited a resistance of 40 kΩ. The emission spectrum of the LED20 LED was recorded using the external input of a Perkin Elmer System 2000 FTIR using an average of 200 measurements. A temperature controller was set so that the temperature dependent resistor in the Peltier cooled LED package, exhibited a resistance of 40 kΩ. The LED was driven with a DC drive current of 75 mA. The recorded spectrum is shown in Figure 6.2. The optical spectral transmission of the Edmund Optics condenser lenses and the responsivities of the optical detector photodiodes were shown as being flat around 2 μm on the product data-sheets.

In order to ascertain the spectral transmission of the HCP400 optical couplers, that were used in the correlation spectroscopy system investigated, the wavelength dependence was experimentally found using a Cary UV 400 spectrophotometer. A fibre input of the optical coupler was placed facing the optical source of the spectrophotometer, and

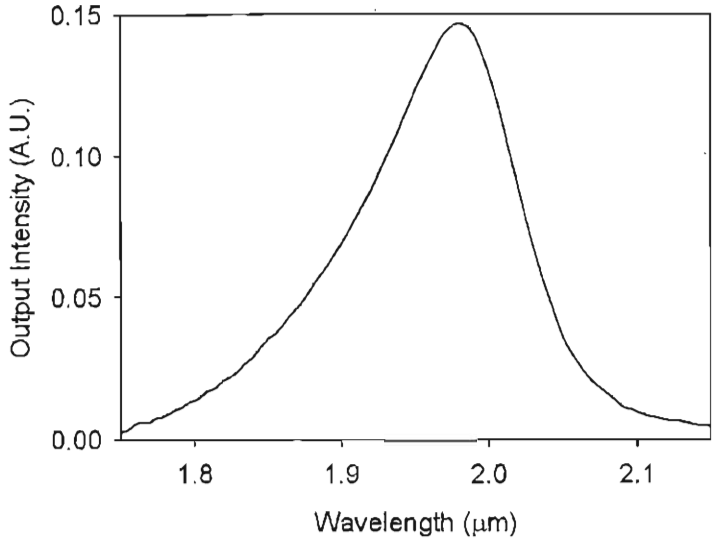

FIGURE 6.2: The emission spectrum of a LED20 2 μm LED manufactured by IBSG, St. Petersburg, Russia. The LED was driven with a DC current of 75 mA and the LED was cooled so that the temperature dependent resistor exhibited a resistance of 40 kΩ. The spectrum was recorded using the external input of a Perkin Elmer System 2000 FTIR and a MIR-TGS detector.

the two output arms of the coupler were sequentially placed facing the measurement detector.

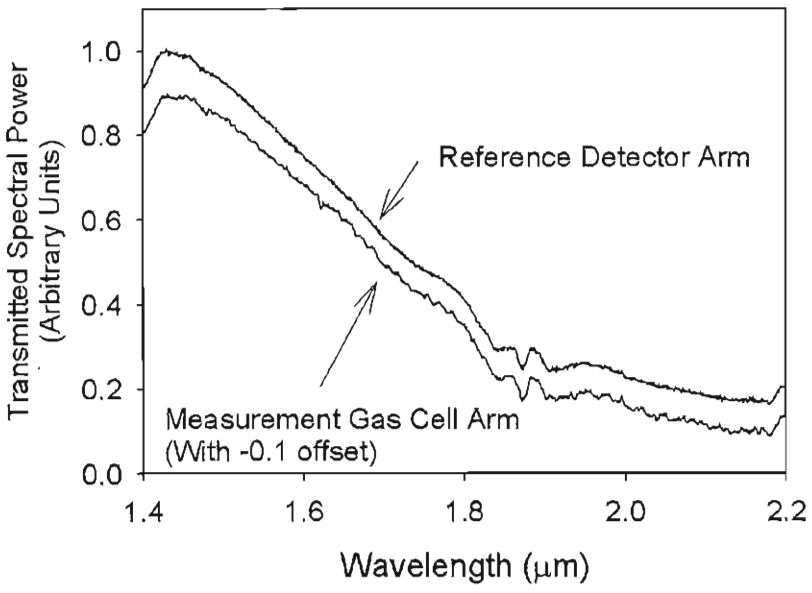

FIGURE 6.3: The optical spectral transmission observed from the two output arms of a HCP400 optical coupler. The transmission spectra of the output arms that were connected to the reference detector and the measurement gas cell are shown. The measurements were carried out using a Cary UV 400 spectrophotometer.

Figure 6.3 shows the transmission spectral characteristic of the optical coupler, from the output arms that were connected to the reference detector and the measurement gas cell of the correlation spectroscopy system. The figure shows that the transmission

of both arms of the coupler is similar in terms of the shape of the spectral response, and approximately a factor of 4 times higher at 1.5 μm than it is at around 2 μm. Consequently, at around 2 μm, the transmission of each arm of the optical coupler is, at most, 12.5% of the input power applied to the input arm, due to the combination of the splitting action and spectral loss of the optical coupler.

Figure 6.4, which is a magnified version of the transmission spectrum of the optical coupler around 2 μm, suggests that there is a 30% decrease in the transmission of the optical coupler across the 200 nm band used for the CO_2 measurements. The figure also shows that the downward slope across the this spectral band was linear. As the gradient of the spectral loss change across the spectral absorption of CO_2 appears to be approximately linear, and the spectral absorption of CO_2 is approximately symmetric around 2.01 μm, it would thus be expected that the effects the on the recorded modulation index would approximately balance. The effect of two optical couplers in series, possessing a 30% linear downward slope, across the bandwidth of the CO_2 spectral absorption was simulated. The simulation with a CO_2 concentration of 100%, a pressure of 1 bar and a temperature of 20°C was used. It was found that the resultant change of the modulation index, as a consequence of this 30% linear downward slope across the 175 nm FWHM spectral bandwidth of the optical bandpass filter, would be <1%.

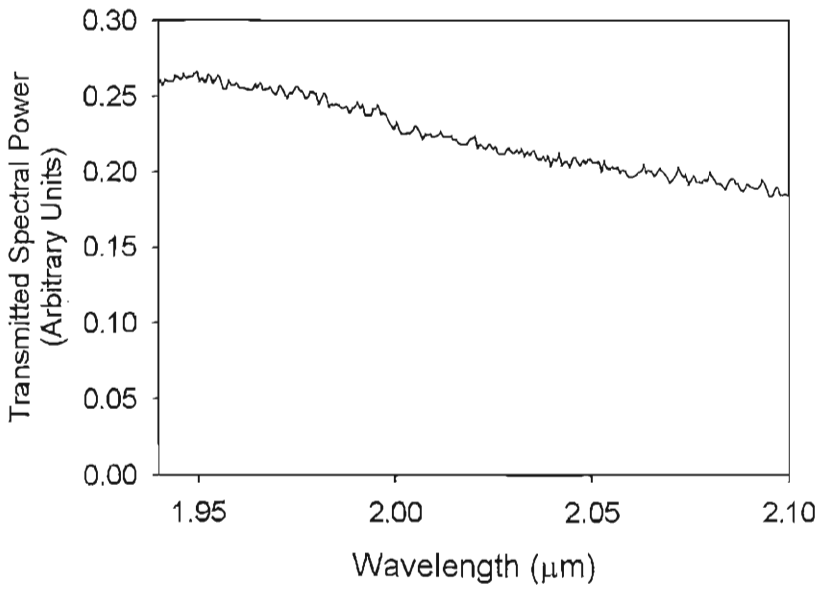

FIGURE 6.4: The optical spectral power observed at the reference detector output arm of the optical coupler. The spectral wavelengths shown cover the region of the spectral absorption of CO_2 around 2 μm.

Hamamatsu extended InGaAs G8373-01 solid state photodiodes were used as the reference and measurement optical detectors. These were used with transimpedance amplification arrangements, where the feedback resistors used with the reference detector and the measurement detector were 10 MΩ and 100 MΩ, respectively. The Operational AMPlifiers (OPAMPs) in the transimpedance amplifiers were Analog Devices OP27s.

The optical fibres used in the system were 600 μm core diameter Newport sensor grade fibre (F-MBD).

The output signal at the measurement detector, which was due to the presence of the gas under investigation in the measurement gas cell, was measured by a lock-in amplifier. A sampled output from the lock-in amplifier was then fed to a single-pole low pass filter, with a time constant of 10 seconds, in order to filter the signal present at the measurement detector. This control system was designed and built by Dr. E. A. D. Austin. The circuits used to control the switching of the LEDs consisted of a Voltage Controlled Current Source (VCCS) with a switching transistor in parallel with the LEDs. The switching frequency used was 500 Hz.

A measurement signal was found to be present when there was only dry nitrogen (N_2) present in the measurement gas cell. In order to correct this, it was necessary to subtract a voltage offset from the measured signal in order to obtain a zero reading at 0% measurement gas cell CO_2 concentration. This offset was assumed to be due to a failure in the optical couplers, in that they did not combine the optical power in a precise 50/50 ratio. Typically this offset was approximately 15 mV, whereas the average DC total measurement voltage was approximately 200 mV.

6.2.2 The Gas Cells

Two gas cells, each 26 cm long were used. A diagram of the design used for these gas cells is shown in Figure 6.5. Originally these gas cells were to be used in an arrangement where it was intended that the majority of the optical power went via a three-pass arrangement and the remainder would go via a single pass. However, owing to difficulties in establishing the effective path-length, the cell was simplified to a single-pass arrangement by the introduction of plastic blocking plates in front of the concave mirrors, and the appropriate adjustment of the distance between the optical fibre ferrules and the focussing lenses. This is further discussed in Section 7.5 of Chapter 7.

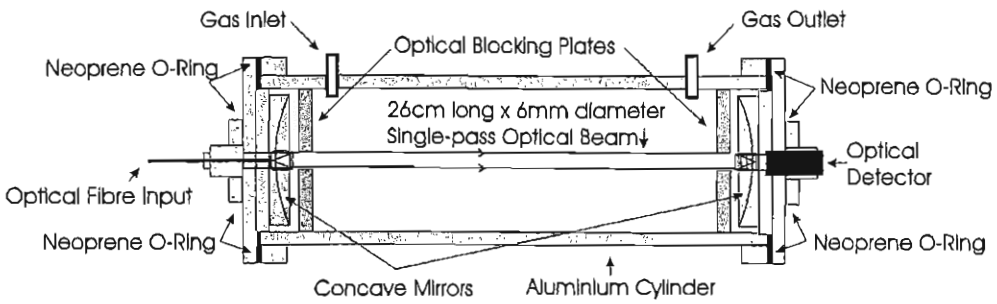

FIGURE 6.5: A schematic diagram of the a 26 cm long gas cell used during the experimental investigations. The modifications to the 3-pass gas cell discussed in Section 7.5 of Chapter 7 are shown, i.e. the insertion of the blocking washers.

In order to monitor the pressure of the gas in the gas cells Druck PTX7517-1 pressure transducers were attached to the fittings on the gas cells. A LM35CZ temperature sensor was attached under insulating tape to the outside of the gas cell. The temperature of the measurement gas cell was controlled by means of a coil of 6 mm copper pipe wound round the cell and circulated with water from a temperature controlled bath.

6.2.3 Gas Handling System

The gases that were used for the experiments described in this chapter were supplied from the sources, and were of the grades, mentioned in Table 6.1. Gas from these sources was passed through nylon 4 mm tubing (part number: NMSF06M BLU, Copely Developments) into a mixing arrangement where the gases were separately fed into two Tylan FC2900-4S Mass Flow Controllers (MFCs) and then through two non-return valves before being mixed in the required ratio. Flow rates through the MFCs were determined with reference to the Tylan FC2900-4S MFC datasheets for the repective gases.

Gas	Supplier	Grade	Delivery Method
Nitrogen (N_2)	BOC Gases	>99.99%	Cylinder (ORC piped supply)
Carbon Dioxide (CO_2)	C.K. Gases	99.95%	3L Cylinder

TABLE 6.1: Sources of gases used in experiments and their purity as supplied from the cylinder.

As some of the experiments required the pressurisation of the reference gas cell, a direct link from the CO_2 supply to the reference gas cell was installed. This link is also shown in Figure 6.1.

6.3 The Dependence of Modulation Index on Measurement Gas Cell CO_2 Concentration

The first experiment to be described had the objective of obtaining experimentally the relationship between the modulation index and the measurement gas cell CO_2 concentration at room temperature and pressure (20°C and 1 bar respectively). The results from this experiment then allowed a quantitative comparison with simulation to be made. The results from this experiment also enabled the noise sensitivity of the setup to be assessed.

6.3.1 Experimental Procedure

In order to find the dependence of the modulation index on measurement gas cell CO_2 concentration, increasing concentrations of CO_2 gas diluted in N_2 gas (ranging from 0% to 100%, in steps of 20%) were examined. The experiment to establish this dependence sequentially analysed each gas concentration in 10 minute time slots, starting at 0% CO_2 gas concentration. A return to 0% CO_2 gas concentration was performed at the end of the experiment in order to enable the stability of the measurement during the 120 minute experiment duration to be observed. The break-down of the 120 minute experiment time is shown in Table 6.2. The table also shows the relative flow rates that were applied to the Tylan FC2900-4S MFCs in order to obtain a mixture of CO_2 and N_2 gases of the required composition (these flow rates were calculated using the data supplied on the MFC datasheet). The interface electronic circuitry for the Tylan FC2900-4S MFCs was previously constructed by Mr. T. C. Austin for use with a sputtering arrangement. The gas flow rate through the MFC depended linearly on the voltage applied to the MFC's control terminal. The electronic circuitry converted the voltage applied to the control terminal of the MFC, which varied linearly between 0 and 5 V, to a numerical value that varied linearly between 0 and 1000.

Time at which CO_2 gas concentration was applied.	Percentage of CO_2 present in the Measurement Gas Cell diluted in N_2 gas.	Gas Flow rates used	
		N_2	CO_2
0 min(0 s)	0%	1000	0
10 min(600 s)	20%	1000	339
20 min(1200 s)	40%	1000	905
30 min(1800 s)	60%	491	1000
40 min(2400 s)	80%	184	1000
50 min(3000 s)	100%	0	1000
60 min(3600 s)	0 %	1000	0
70 min(4200 s)	End		
Relative Flow Factors	N_2	1.000	
	CO_2	0.737	

TABLE 6.2: The time schedule of the experiment to find the dependence of modulation index on measurement gas cell CO_2 concentration. The relative gas flow rates used to obtain measurement gas cell samples are also shown.

The breakdown of the 10 minute time slot, during which each CO_2 gas concentration was analysed, is shown in Table 6.3. Initially, a 3 minute time period was allocated, during which the gas mixture flowed through the measurement gas cell. The system then remained idle for a 1 minute period in order to allow it to stabilise to the changed measurement gas cell CO_2 concentration. During the following 5 minutes the recorded

measurements contributed to an averaged value used for the subsequent analysis. Finally, a 1 minute time period was allocated before the next gas mixture was analysed.

Time (min)	Time (s)	Action
0-3 min	0-180 s	Gas cells with gas supply flowing through them
3-4 min	180-240 s	Gas valves closed and system idle
4-9 min	240-540 s	Active Measurement
9-10 min	540-600 s	System idle

TABLE 6.3: Breakdown of the 10 minute time-slot allocated to each CO_2 gas concentration used during the experiment to determine the variation of modulation index with CO_2 gas concentration.

6.3.2 Experimental Results

A graphical representation of the results obtained from this experiment is shown in Figure 6.6. This is the output of the measurement digital low pass filter, sampled at a frequency of 1 Hz during the experiment. In order to remove the high frequency (i.e. compared to the time span of the measurement) noise present in the experimental apparatus, from the graphical representation, the signal was filtered, or smoothed, using a 60 point Hanning function (a low pass filtering function).

In the results shown in Figure 6.6, the standard deviation of the signal during the active measurement time slots is 1.5×10^{-4}. When compared to the modulation index full scale deflection (0.017), this yields a SNR response of 112. In Chapter 7, the system noise that would be expected by theory is derived and compared to this experimental result.

The "smoothed" result of the Hanning filtering function is shown in Figure 6.7. The points shown in this figure are the averages of the data recorded during the active time slots and the error bars show the peak to peak variations of the data.

6.3.3 Derived Trends and Comparison with Simulation

In order to show the trend of the experimental data it was decided to fit the data to a mathematical function. The function chosen to fit the data was $m(x) = ax^b$, where x is the CO_2 gas concentration, $m(x)$ represents the dependence of the modulation index on x, a represents the value of the modulation index reached at 100% measurement gas cell CO_2 concentration and b represents the shape of the curve. For values of b approaching 0, the rate of decrease of the slope, $\frac{d(m(x))}{dx} = abx^{b-1}$, decays as a reciprocal function,

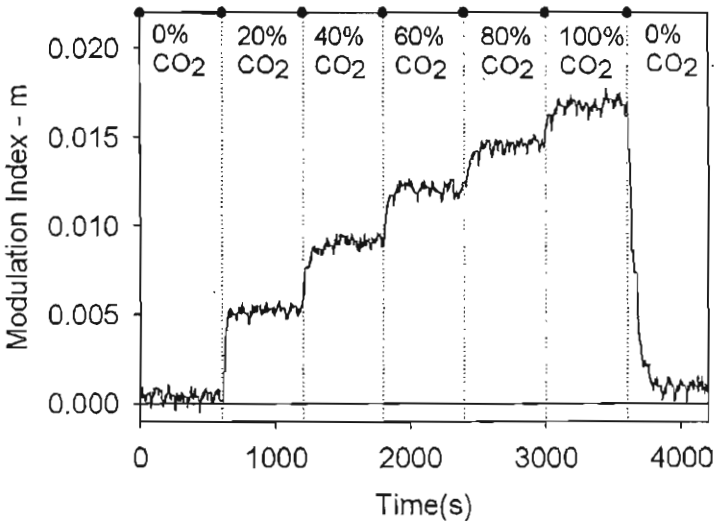

FIGURE 6.6: Raw data of modulation index (m) with varying measurement gas cell CO_2 concentration diluted in N_2 gas. The data were sampled at a sampling frequency of 1 Hz. Both the reference and measurement gas cells were held at a temperature of 20°C and at a pressure of 1 bar.

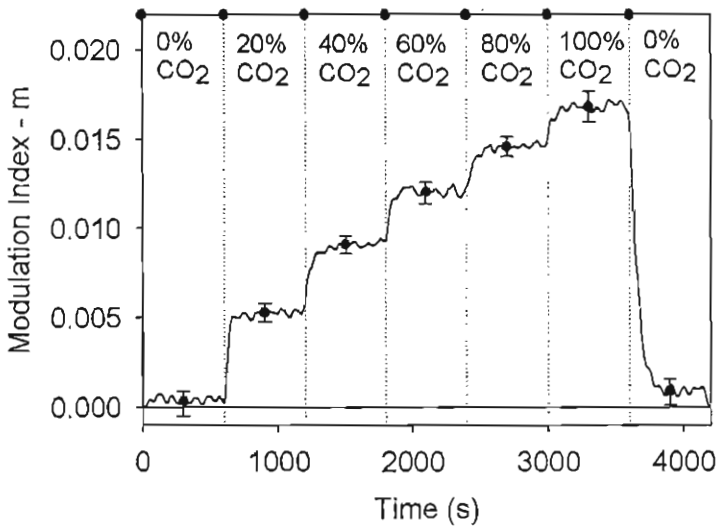

FIGURE 6.7: Smoothed data of modulation index (m) with varying measurement gas cell CO_2 concentration diluted in nitrogen gas (N_2). The "smoothing" function used was a 60 point Hanning function. The error bars show the peak to peak variation in the raw data signal and the data-point represents the average modulation index during the active measurement time period. Other conditions are as described in the caption of Figure 6.6.

whereas as b approaches 1 the slope is constant and the shape of the graph approaches a straight line. These behaviours are described by equations 6.1 and 6.2 respectively:

$$\frac{d(m(x))}{dx} \rightarrow ab\tfrac{1}{x}, \quad as \quad b \rightarrow 0 \tag{6.1}$$

$$\frac{d(m(x))}{dx} \rightarrow a, \quad as \quad b \rightarrow 1 \tag{6.2}$$

The averaged data points shown in Figure 6.7 were used to construct a least squares data-fit. The comparison of the averaged experimental data points and the data-fit is shown graphically in Figure 6.8.

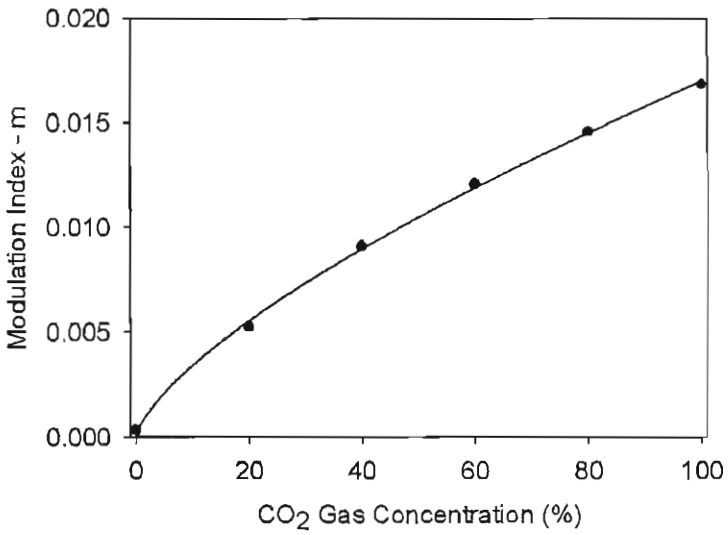

FIGURE 6.8: Experimental averaged results extracted from the data shown in Figure 6.7. The reference and measurement gas cells were each 26 cm long and were held at a temperature of 20°C and a pressure of 1 bar. The least squares data fit to the function $m(x) = ax^b$ is also shown.

In order to enable the experimental data points and simulated data to be compared, a simulation was carried out to model the dependence of modulation index on CO_2 concentration in the measurement gas cell. This simulation incorporated the emission spectrum of the LED20 LED. A graphical comparison of the simulation result and the least-squares data-fit to the experimental data is shown in Figure 6.9.

By also fitting the simulation data to the same function the parameters extracted from the data can be used to directly compare the simulation results with the experimental results. Table 6.4 shows a comparison between the numerical values extracted for a and b from the experimental and simulated data-fits. The data in the table include the standard errors associated with a and b, and the values of r^2 (a measure of the accuracy of the data fits) were found to exceed 0.995 for both the experimental and simulated data-fits. These data also show that there is a 7.65% difference between the experimental and simulated data for the value a, which describes the value of the modulation index that is attained at 100% measurement gas cell CO_2 concentration. The simulation

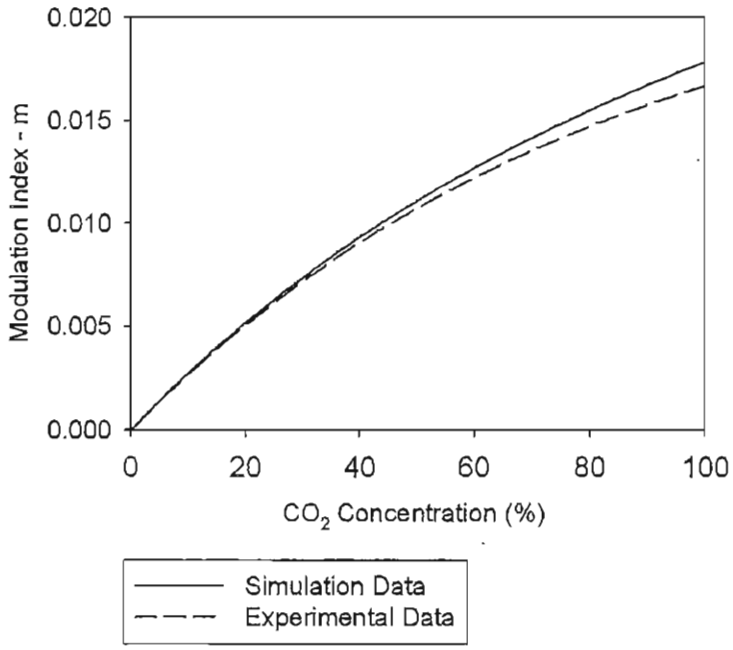

FIGURE 6.9: The fitted function and the experimental results and the simulation result describing the dependence of modulation index on the measurement gas cell CO_2 concentration. The method of least squares data fit to the experimental results was described in the text. In the experiment and the simulation the reference and measurement gas cells were 26 cm long, at a temperature of 20°C and at a total CO_2 pressure of 1 bar.

has thus suggested that a 7.65% greater modulation index would be observed at 100% measurement gas cell concentration than was experimentally found to be the case.

The value of b extracted from the experimental data was found to be 8.83% less than that extracted from the simulated data. This means that the data obtained from experiment is somewhat less linear than the simulation suggested.

6.3.4 The Noise in the Experimental Results

The RMS noise in the modulation index observed during the active measurement time slots in the above measurements was 2.8×10^{-4}. The division of the modulation index, with 100% CO_2 gas in the measurement gas cell, 0.0183, by the RMS noise, 2.8×10^{-4}, gives the SNR of the measurement, which was 65. The feedback system and the comparison with the theoretically expected noise are described in Section 7.4.6 of Chapter 7.

Function to which data was fitted: $f(x) = ax^b$		
Experimental Data Fit	Value	Std. Error
a	0.0170	±0.0002
b	0.6953	±0.0236
r^2	0.9959	
Simulation Data Fit		
a	0.0183	±0.0001
b	0.7567	±0.0057
r^2	0.9974	
Variable	% Difference $\left(\frac{Sim-Exp}{Exp}\right)$	
a	+7.65%	
b	+8.83%	

TABLE 6.4: The fitted least squares data-fit parameters to the experimental and simulated results for the variation of CO_2 gas concentration in the measurement gas cell with a reference gas cell CO_2 pressure of 1 bar. The percentage disagreement between the parameters extracted for the experimental and simulated results is also shown as a proportion of the extracted values from the experimental data. The values of r^2 for the data fit of the experimental and simulated data are also given.

6.4 Method of Increasing the Modulation Index by Increasing the Reference Gas Cell CO_2 Pressure

In Chapter 5 a method of increasing the modulation index by increasing the CO_2 reference cell gas pressure was described in terms of simulated results. The concept of the 'improvement factor' was also introduced, which was the factor by which the modulation index increases, due to the reference gas cell being pressurised to a given CO_2 gas pressure. With the introduction of a contaminant gas vapour (H_2O) the simulations also suggested that the magnitude of the modulation index would increase with increasing contaminant gas concentration when the reference gas cell was pressurised. In the following sections the results from experiments are presented that had the objective of experimentally verifying these trends suggested by simulation.

6.4.1 The Experiment

In order to assess the effect of the pressurisation of the reference gas cell, the analysis that was shown in Section 6.3 with a reference gas cell pressure of 1 bar, was repeated at other reference gas cell CO_2 pressures. The "smoothed" results from these experiments are shown in Figure 6.10. Due to the relatively fast rise of the response of modulation index versus reference gas cell CO_2 pressure at low pressures, an experiment at a reference

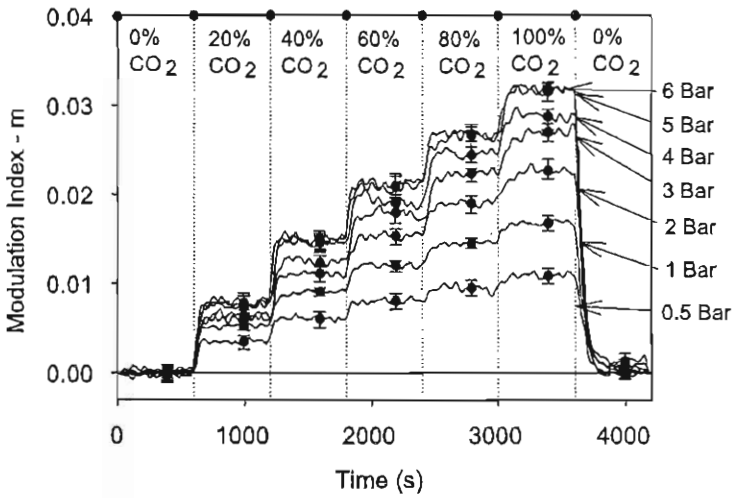

FIGURE 6.10: Smoothed experimental data of modulation Index (m) with varying measurement gas cell CO_2 concentration diluted in N_2 gas at the selected CO_2 gas pressures in the reference gas cell that are indicated by the labels on the graph. The error bars show the peak to peak variation in the sampled 1 Hz data signal and the data points represent the average modulation index during each active time period. Other conditions are as described in the caption of Figure 6.7.

gas cell CO_2 pressure of 0.5 bar was carried out in order to give an improved graphical impression of the response. For the experiment, at a reference gas cell pressure of 0.5 bar CO_2, a KNF Neuberger VP1HV diaphragm vacuum pump was used to depressurise the CO_2 containing reference gas cell.

For analysis the data presented in Figure 6.10 are grouped into two classifications, which are:

1. Grouping by reference gas cell CO_2 pressure, at varying measurement gas cell CO_2 concentrations.
2. Grouping by measurement gas cell CO_2 concentration, at varying reference gas cell pressures.

In the following two sections the experimental data are analysed in terms of each of these classifications.

6.4.2 Analysis of Grouping by Reference Gas Cell CO_2 Pressures at Varying Measurement Gas Cell CO_2 Concentrations

The data-fit to the function $m(x) = ax^b$ that was carried out with the data describing the CO_2 gas concentration in the measurement gas cell, was extended to the experimental data representing other reference gas cell pressures. Here a is the modulation index reached at 100% CO_2 measurement gas cell concentration and b describes the shape of the response (see Section 6.3.3).

Figure 6.11 shows the fitted response curves to the experimental data at increasing reference gas cell CO_2 pressures. The results of the equivalent simulations, again using the recorded LED-20 emission spectrum, are shown in Figure 6.12.

The least-squares fitted values for a and b, their associated standard errors and the difference between the simulated and experimentally determined improvement factors, as a proportion of the experimental values, are shown in Table 6.5. It was found that the maximum difference between the experimental and simulated values of a was 14.82%, which occurred at a reference gas cell pressure of 6 bar. The maximum difference in the value b was 9.70%, which occurred at a reference gas cell pressure of 5 bar. Thus these results imply that the magnitude of the modulation index was less than was found by simulation of the Hitran data and the responses were on average more non-linear than was found by simulation.

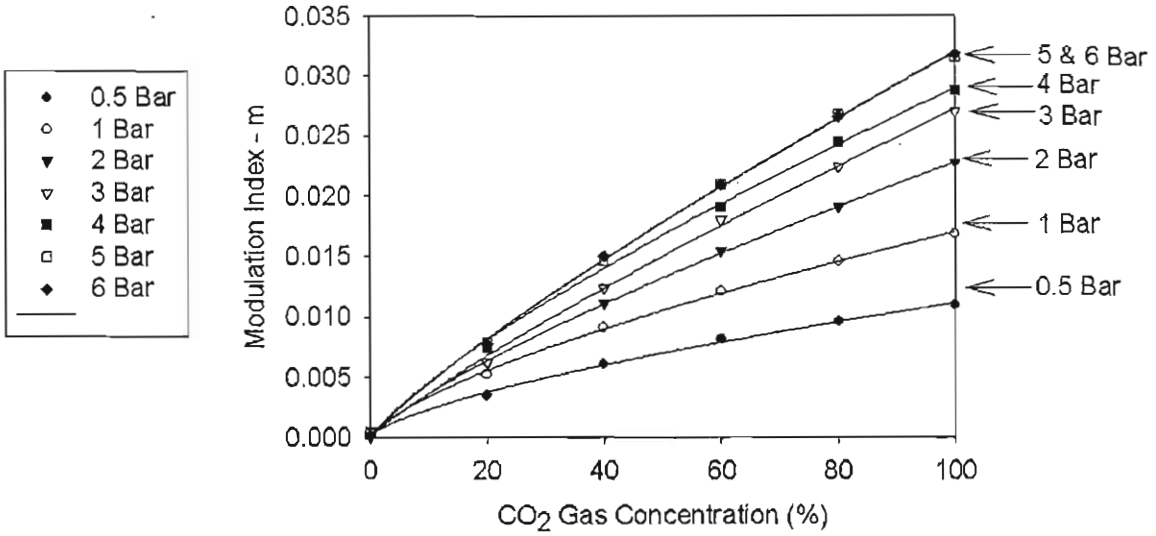

FIGURE 6.11: Experimental results describing the effect of varying CO_2 concentration in the measurement gas cell on the modulation index at different CO_2 gas pressures in the reference gas cell. The CO_2 gas pressures of the reference gas cell are shown by the labels on the graph.

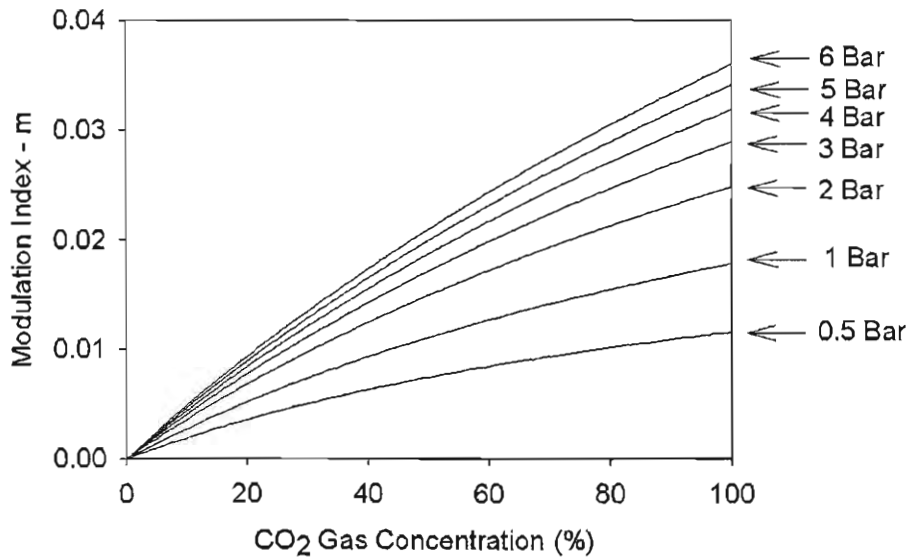

FIGURE 6.12: Simulated results describing the effect of varying CO_2 concentration in the measurement gas cell on the modulation index at different CO_2 gas pressures in the reference gas cell. The CO_2 gas pressures of the reference gas cell are shown by the labels on the graph.

Data Fit Function: $m(x) = ax^b$												
Pressure	Experimental Data Fit Parameters					Simulation Data Fit Parameters					% Difference between exp. and sim. $\left(\frac{Sim-Exp}{Exp}\right)$	
	a	Std. Error	b	Std. Error	r^2	a	Std. Error	b	Std. Error	r^2	a	b
0.5 bar	0.0111	±0.0002	0.6704	±0.0279	0.9990	0.0120	±0.0000	0.7224	±0.0065	0.9962	+9.09%	+7.76%
1 bar	0.0170	±0.0002	0.6953	±0.0236	0.9959	0.0183	±0.0001	0.7567	±0.0057	0.9974	+7.65%	+8.83%
2 bar	0.0228	±0.0002	0.7905	±0.0143	0.9998	0.0254	±0.0001	0.7905	±0.0047	0.9984	+11.40%	0.00%
3 bar	0.0272	±0.0003	0.8631	±0.0248	0.9990	0.0295	±0.0001	0.8068	±0.0043	0.9987	+8.46%	−6.52%
4 bar	0.0289	±0.0005	0.7930	±0.0340	0.9977	0.0324	±0.0001	0.8160	±0.0041	0.9989	+12.11%	+2.90%
5 bar	0.0319	±0.0003	0.8472	±0.0199	0.9993	0.0347	±0.0001	0.8218	±0.0039	0.9990	+8.78%	+9.70%
6 bar	0.0320	±0.0003	0.8464	±0.0182	0.9994	0.0366	±0.0001	0.8258	±0.0038	0.9990	+14.38%	−2.43%

TABLE 6.5: The fitted least squares data-fit parameters to the experimental and simulated results for the variation of CO_2 gas concentration in the measurement gas cell at set reference gas cell CO_2 pressures. The percentage disagreement between the parameters extracted for the experimental and simulated results are also shown as a proportion of the extracted values for the experimental data.

6.4.2.1 Analysis of the Dependence of the Improvement Factor on Reference Gas Cell Pressure

The improvement in the modulation index that results from the pressurisation of the reference gas cell to a given CO_2 pressure was termed the improvement factor (see Section 5.10, Chapter 5). Using the values of a for the different reference gas cell CO_2 pressures, the improvement factors due to the increasing reference gas cell pressures investigated may be calculated. Table 6.6 shows the experimental improvement factors relating to the reference gas cell pressures studied and the improvement factors obtained by simulation.

Reference Gas Cell CO_2 Pressure	Experimental Improvement Factor	Simulated Improvement Factor	% Difference $\left(\frac{Sim-Exp}{Exp}\right)$
0.5 bar	0.65	0.66	−0.43%
1 bar	1.00	1.00	0.00%
2 bar	1.34	1.39	+3.40%
3 bar	1.60	1.61	+7.51%
4 bar	1.70	1.77	+4.15%
5 bar	1.88	1.90	+1.05%
6 bar	1.88	2.00	+6.25%

TABLE 6.6: The comparison of the derived improvement factors from experimental and simulated data relating to changing reference gas cell pressure. The experimental data were extracted from the experiment described in Section 6.3.2. Both the experimental and simulated data relate to the use of reference and measurement gas cells of 26 cm length, a temperature of 20°C and a measurement gas cell pressure of 1 bar. These data were obtained from the data-fits shown in Table 6.5.

It was found by experiment that the improvement factor varied between 0.65 and 1.88 due to pressures applied to the reference gas cell of between 0.5 bar and 6 bar. The difference between the experimentally determined improvement factors, as a proportion of the experimental data, was found to vary between −0.43% and +7.51% for reference gas cell pressures of between 0.5 bar and 6 bar. The good agreement between the data-fits presented in this section means that the improvement factors at other gas cell pressures may be accurately estimated.

6.4.3 Analysis of Grouping by Measurement Gas Cell CO_2 Concentration at Varying Reference Gas Cell CO_2 Pressures

In Chapter 5, Section 5.10.1 it was shown using simulated results that with decreasing measurement gas cell CO_2 concentration, there was also a resulting decrease in the improvement factor. In order to assess this from the experimental results, the data displayed in Figure 6.10 were grouped by measurement gas cell concentration at the reference gas cell total pressures that were investigated. Figure 6.13 shows the data

grouped at these measurement gas cell concentrations and also, the least squares line fits to the function $m(x) = cx^d$, where $m(x)$ is the modulation index as a function of x, the measurement gas cell CO_2 concentration, c is the value fitted at a reference gas cell total pressure of 1 bar and d describes the linearity of the response with increasing measurement gas cell CO_2 concentration (see discussion of equations 6.1 and 6.2).

Figure 6.14 shows the data that resulted from simulations carried out in order to model the dependence of the modulation index on increasing the total pressure of CO_2 in the reference gas cell. These simulations incorporated the recorded emission spectrum of the LED20-LED. The values of c and d extracted from the data fits to the experimental and simulated data at the selected measurement gas cell CO_2 concentrations, and the percentage difference between the experimental and simulated values are shown in Table 6.7. This table also shows the values of r^2 describing the accuracy of the data fit to both the experimental and simulated data.

The data in Table 6.7 show that, while all the values of r^2 exceed 0.94 (excluding the 0% measurement gas cell CO_2 concentration readings), the data-fit to the statistical model is not as good as was the case for the results grouped by reference gas cell CO_2 pressure.

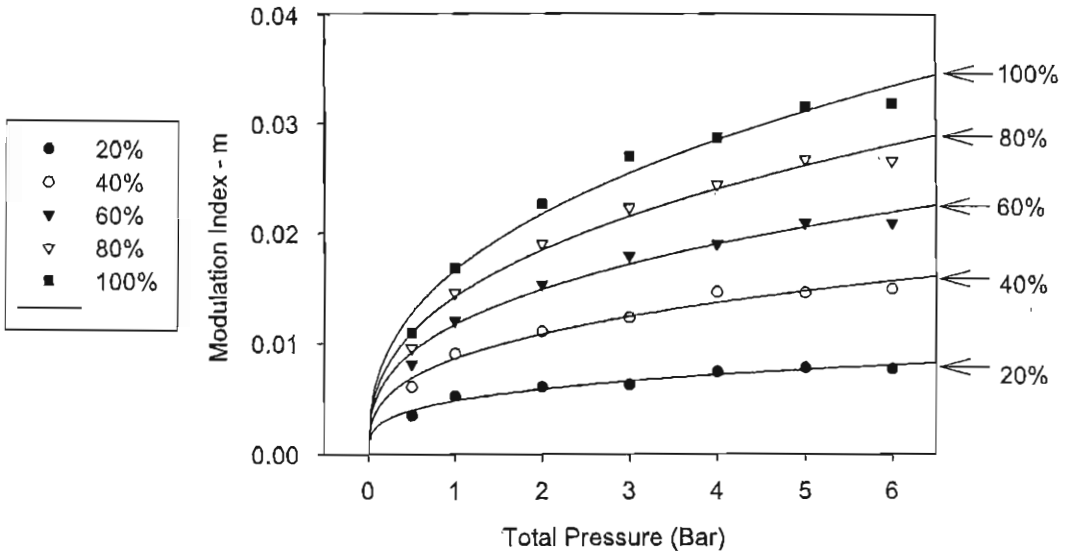

FIGURE 6.13: Experimental results showing the effect on the modulation index of increasing CO_2 pressure in the reference gas cell at different concentrations of CO_2 gas in the measurement gas cell. The total pressure of CO_2 gas in the reference gas cell and the concentration of CO_2 gas in the measurement gas cell are shown by the x axis and the labels on the graph respectively. The least-squares-fits to the function $m(x) = cx^d$, where the terms are defined in the text, are shown.
The reference and measurement gas cells were 26 cm long and at a temperature of 20°C.

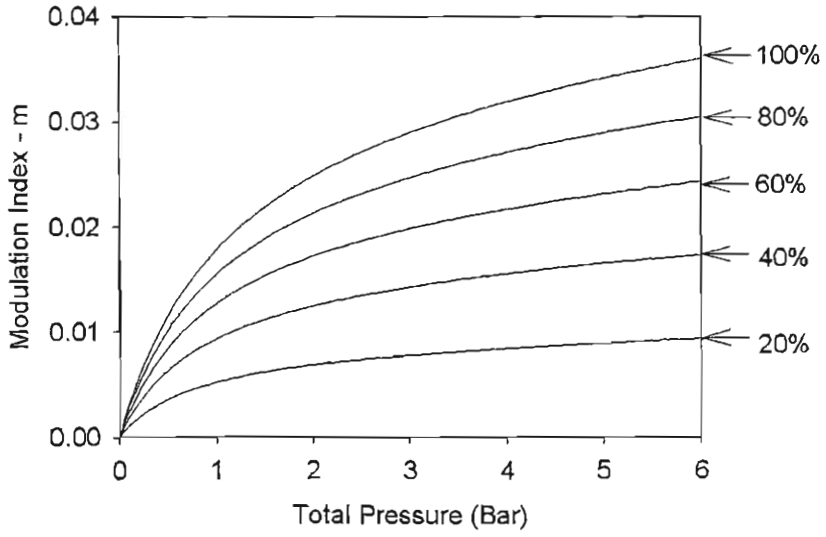

FIGURE 6.14: Simulated results results describing the effect of increasing CO_2 pressure in the reference gas cell at set concentrations of CO_2 gas in the measurement gas cell. The simulated total pressure of CO_2 gas in the reference gas cell and the concentration of CO_2 gas in the measurement gas cell are shown by the x axis and the labels on the graph, respectively. The reference and measurement gas cells were modelled as being 26 cm long and at a temperature of 20°C.

Data Fit Function: $m(x) = cx^d$												
Pressure	Experimental Data Fit Parameters					Simulation Data Fit Parameters					% Difference between exp. and sim. $\left(\frac{Sim-Exp}{Exp}\right)$	
	c	Std. Error	d	Std. Error	r^2	c	Std. Error	d	Std. Error	r^2	c	d
0% Begin	0.0001	±0.0001	–	–	–	0.0000	±0.0000	–	–	–	−100%	–
20%	0.0049	±0.0002	0.2838	±0.0336	0.9481	0.0051	±0.0000	0.3622	±0.0067	0.9759	+4.08%	+27.63%
40%	0.0087	±0.0004	0.3308	±0.0324	0.9656	0.0092	±0.0001	0.3774	±0.0068	0.9887	+5.75%	+14.09%
60%	0.0117	±0.0005	0.3493	±0.0280	0.9771	0.0126	±0.0001	0.3914	±0.0069	0.9789	+7.69%	+12.05%
80%	0.0142	±0.0006	0.3788	±0.0300	0.9783	0.0154	±0.0001	0.4044	±0.0069	0.9783	+8.45%	+6.76%
100%	0.0166	±0.0008	0.3894	±0.0327	0.9760	0.0179	±0.0002	0.4163	±0.0070	0.9810	+7.83%	+6.91%
0% End	0.0004	±0.0003	–	–	–	0.0000	±0.0000	–	–	–	−100%	–

TABLE 6.7: The least squares line fit parameters to the experimental and simulated results for the variation of the total pressure of the reference gas cell containing only CO_2 gas. The measurement gas cell contained a mixture of CO_2 and N_2 gas. The percentage difference between the simulated and experimental values for c and d are shown as a proportion of the experimentally derived value. The table shows the results from the 0% measurements at the beginning and end of each measurement cycle (the value of d is not shown for the 0% measurements because it is undefined).

6.4.3.1 Analysis of the Dependence of the Improvement Factor on Reference Gas Cell Pressure at Selected Measurement Gas Cell CO_2 Concentrations

The derived improvement factors from experiment and simulation that are associated with each of the measurement gas cell concentrations investigated are shown in Table 6.8. While the improvement factor at 100% CO_2 measurement gas cell concentration is as was previously shown in Table 6.6, at lower measurement gas cell CO_2 concentrations the improvement factor successively decreases.

It may also be observed that there is an increasing disagreement between the experimental and simulated results that starts at 6.78% at 100% measurement gas cell CO_2 concentration and increases to 23.10% at 20% measurement gas cell CO_2 concentration.

Measurement Gas Cell CO_2 Concentration	Experimental Improvement Factor	Simulated Improvement Factor	% Difference $\left(\frac{Sim-Exp}{Exp}\right)$
100%	1.89	2.02	6.78%
80%	1.82	1.97	8.84%
60%	1.73	1.91	10.32%
40%	1.64	1.86	13.02%
20%	1.46	1.80	23.10%

TABLE 6.8: The comparison of the derived improvement factors from experimental and simulated data relating to changing measurement gas cell CO_2 concentration. Both the experimental and simulated data relate to the use of reference and measurement gas cells of 26 cm length, at a temperature of 20°C. The reference gas cell, contained 100% CO_2 gas, at a pressure of 6 bar and the measurement gas cell was at a pressure of 1 bar.

6.4.4 The Increasing Sensitivity to a Contaminant Gas with Increasing Reference Gas Cell CO_2 Pressure

A consequence of increasing reference gas cell pressure is that a correlation spectroscopy system becomes increasingly sensitive to H_2O vapour (a contaminant gas), as was described in Chapter 5, Section 5.10.2. In order to demonstrate and quantify this effect experimentally, a water bubbler was attached to the gas inlet of the measurement gas cell and the relative humidity of the measurement gas cell was measured by inserting the detector head of a Testo 625 humidity sensor at its outflow.

In order to show the effect on the modulation index of the pressurisation of the reference gas cell with H_2O saturated N_2 gas in the measurement gas cell, measurements were taken at 1 bar and 6 bar. At both these reference gas cell pressures dry N_2 gas followed by H_2O saturated N_2, followed by dry N_2 gas were introduced into the measurement gas

cell. A 15 minute time slot was allocated to the investigation of each gas mixture. The time schedule of the experiments at each reference gas cell pressure is shown in Table 6.9.

Time at which gas mixture was applied.	(%) Composition of gas mixture.	Gas Flow rates used.	
		Dry N_2	H_2O saturated N_2
0 min(0 s)	0%	1000	0
15 min(900 s)	100%	0	1000
30 min(1800 s)	0%	1000	0
45 min(2700 s)	End		

TABLE 6.9: The relative gas flow rates used to obtain measurement gas cell samples. The gas flow rates that were applied to the Tylan MFC are also shown.

So that the relative humidity could attain a level in excess of 95%, a longer measurement gas cell filling time of 5 minutes was allowed. Idle times were allocated before and after the 5 minute active measurement times to allow the modulation index to stabilise. An idle period of 5 minutes was allocated after the active measurement time to allow the gas bubbler to be switched in/out of the gas flow circuit. The composition of each block of 15 mins is shown in Table 6.10.

Time (min)	Time (s)	Action
0-5 min	0-180 s	Gas cells with gas supply flowing through them
5-6 min	180-240 s	Gas valves closed and system idle
6-11 min	240-540 s	Active Measurement
11-15 min	540-600 s	System idle

TABLE 6.10: Breakdown of the 15 minute time-slots allocated to each CO_2 gas concentration used during the experiments to determine the variation of modulation index with measurement gas cell H_2O content.

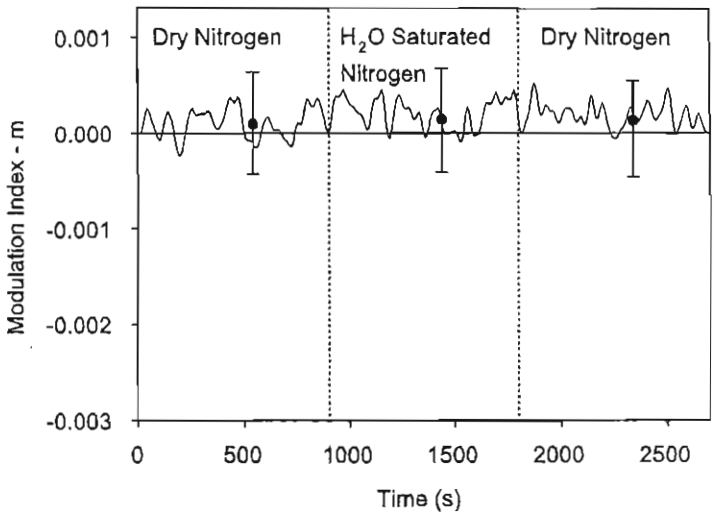

FIGURE 6.15: Water vapour cross talk in measurement cell with the reference cell at a pressure of 1 bar. Saturated air holds about 2.3% H_2O at 20°C.

The "smoothed" results of the two experiments carried out at 1 bar and 6 bar are shown in figures 6.15 and 6.16, respectively.

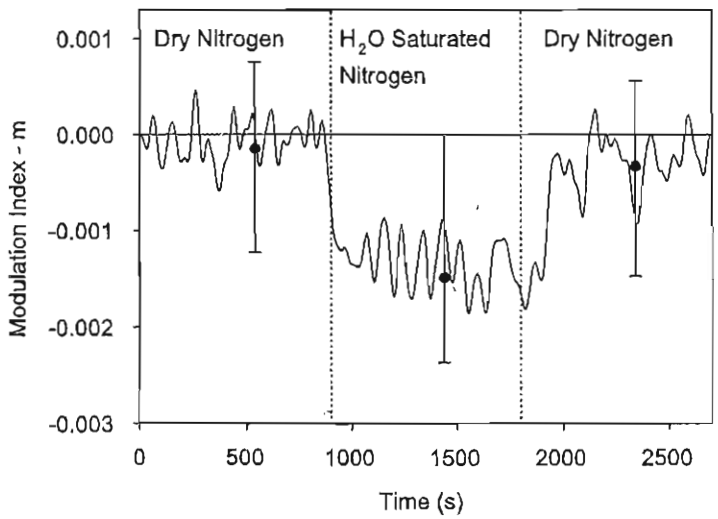

FIGURE 6.16: Water vapour cross talk in measurement cell with the reference cell pressurised to 6 bar (abs). Saturated air holds approximately 2.3% H_2O at 20°C.

The average value of the modulation index, together with its maximum and minimum values, are shown in Figure 6.17. The figure also shows the linear line linking these two points as well as the equivalent simulated results. The sensitivity that may be extracted from the experimental data is -2.97×10^{-4} bar^{-1}, whereas the slope associated with the simulated data is -7.51×10^{-5} bar^{-1}, a factor of 4 times less than the experimental data. This difference is discussed further in the conclusion of this chapter and, as an area of possible future investigation, in Chapter 9.

These experimental results have suggested that at a reference gas cell pressure of 1 bar and at low measurement gas cell CO_2 concentrations, 2.3% H_2O vapour present in the measurement gas cell would be equivalent to 1% CO_2. However, if the reference gas cell is raised to a pressure of 6 bar, the equivalent CO_2 sensitivity increases to 6% CO_2.

Correlation spectroscopy is a wide bandwidth technique and includes a range of spectral absorption features that may not be well characterised in the literature. Inadequacies in the Hitran database's absorption data relating to CO_2 or H_2O may have contributed to this result. Some of the limitations of the Hitran CO_2 data are outlined in the following section. This is a topic that is further discussed in the conclusion and as a possible area of future work in Chapter 9.

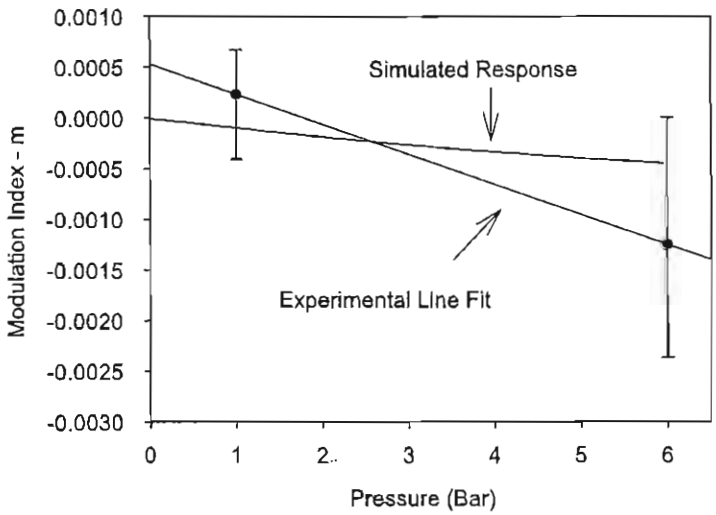

FIGURE 6.17: The comparison of experimental and simulated results relating to the cross-sensitivity of a CO_2 correlation spectroscopy gas detection system to N_2 gas saturated with H_2O vapour in the measurement gas cell as the pressure of CO_2 in the reference gas cell was increased. The error bars represent the peak to peak variation of the raw data. The reference and measurement gas cells were both of 26 cm length and were at a temperature of 20°C. The simulation incorporated the recorded emission spectrum of the LED20 LED.

6.5 The Dependency of Modulation Index on Measurement Gas Cell Temperature

In order to assess experimentally the dependence of the modulation index on measurement gas CO_2 temperature, a series of experiments was carried out at measurement gas cell temperatures between 10°C and 30°C, in increments of 5°C, while the reference gas cell temperature was held at 20°C. For each of these experiments CO_2 concentrations of 0%, 100% and 0% were sequentially applied to the measurement gas cell. The individual measurement times were subdivided into time-slots of 10 minutes. This time schedule is summarised by Table 6.11. The composition of the 10 minute experimental investigation was as defined in Table 6.3, page 78.

Time at which CO_2 gas concentration was applied.	Percentage of CO_2 present in the Measurement Gas Cell diluted in N_2 gas.	Gas Flow rates used	
		N_2	CO_2
0 min(0 s)	0%	1000	0
10 min(600 s)	100%	0	1000
20 min(1200 s)	0%	1000	0
30 min(1800 s)	End		

TABLE 6.11: The time schedule of the experiment to find the dependence of modulation index on measurement gas cell temperature. The gas flow rates used to obtain measurement gas cell samples are shown.

In Figure 6.18 the "smoothed" results are shown from each of the experiments that were carried out at various measurement gas cell concentrations.

Using the averaged data points from the results shown in Figure 6.18 a linear least squares fit was applied. This least squares fit showed a $1.6\%°C^{-1}$ dependence of the modulation index on the temperature of a measurement gas cell containing 100% CO_2. A simulation was also carried out, using the recorded emission spectrum of the LED20, and a $0.26\%°C^{-1}$ dependence of modulation index on measurement gas cell temperature resulted. The experiment and the simulation have thus differed by a factor of 6. The simulation and experimental data are graphically shown in Figure 6.19.

The result from experiment was a factor of 6 times larger than the result from simulation. The principal factors that were likely to have caused this disagreement are inaccuracies in the Hitran data or a temperature dependence of the measurement signal detector, as this was directly attached to the measurement gas cell and experienced the same temperature. The Hitran data representing the absorption of CO_2 gas around 2 μm may also be considered incomplete. This is because investigations have shown that

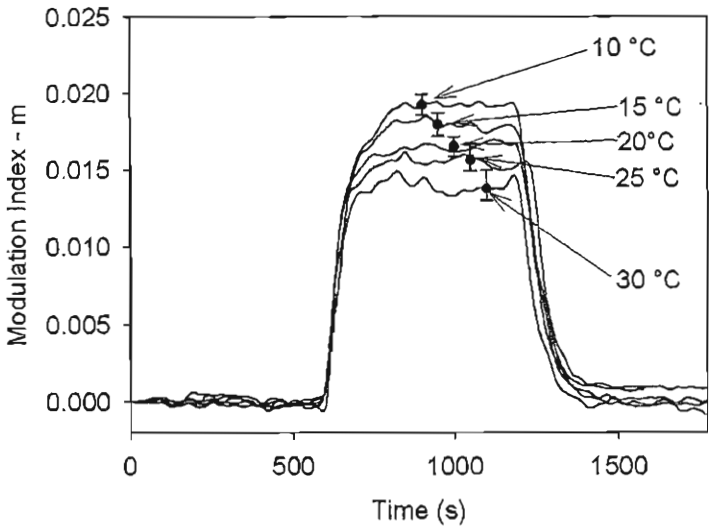

FIGURE 6.18: "Smoothed" Data for the experimental determination of the variation of modulation index with the temperature of the measurement gas cell. The temperature of the measurement gas cell for each experiment are those shown on the labels on the graph. The error bars show the peak-to-peak variation of the modulation index during the active measurement time. The temperature of the measurement gas cell was held to within ±0.5°C of the values stated in the labels in the graph. The reference gas cell temperature was 20°C ± 0.5°C. The gas total pressures of the reference and measurement gas cells were 1 bar.

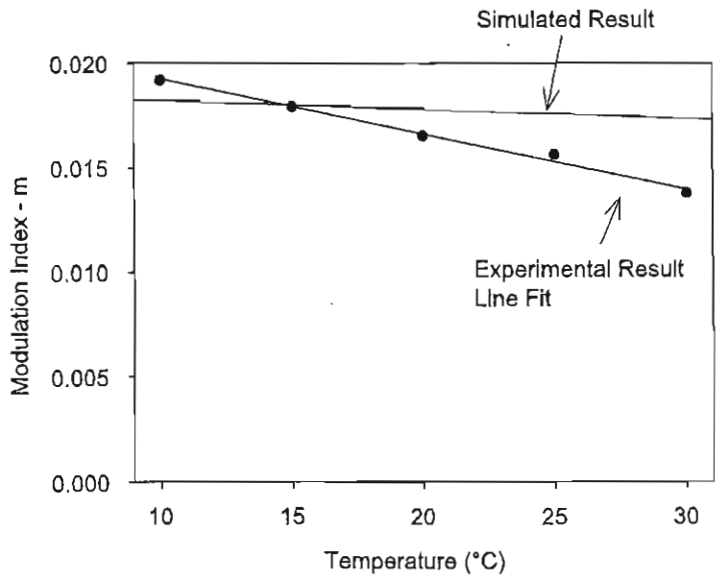

FIGURE 6.19: The comparison of experimental and simulated results relating to the temperature dependence of the modulation index on the measurement cell gas temperature of a CO_2 correlation spectroscopy gas detection system. The reference and measurement gas cells were both of 26 cm length and the reference gas cell was at a temperature of 20°C. The recorded emission spectrum of the LED20 was used for the simulation.

the data originally included in the Hitran 2000 database, which were obtained by a numerical technique named DND (Direct Numerical Diagonalisation) are in error by significantly more than the quoted error of 2%. For example, Aguir *et al.* [34] have shown that the spectral positions of some of the absorption lines are in error by up to 36 cm^{-1}, which may translate into an error of the resultant line strengths. It was also acknowledged by the authors who reported the DND results that the data may lack some unidentified transitions over this wavelength interval. The measurement may also have been affected by a temperature sensitivity of the measurement signal detector, as it was directly attached to the measurement gas cell. The reported theory by Eppeldauer and Hardis [38] suggested that this would affect the noise observed in the measurement, but should not affect the linearity of the sensitivity of the photodiode, which would be required to cause an error in the modulation index.

6.6 Conclusions

This chapter has detailed experiments that had the objective of characterising a CO_2 correlation spectroscopy gas detection system.

The initial experiment described had the objective of showing the dependence of the modulation index on measurement gas cell CO_2 concentration at laboratory temperature and pressure (20°C and 1 bar, respectively). It was shown that the modulation index at 100% measurement gas cell concentration was 0.017, and that the shape of the response of the modulation index to lowering measurement gas cell concentrations was accurately described by the function $m(x) = ax^b$, where x is the measurement gas cell CO_2 concentration. It was found that the value of r^2 describing the accuracy of experimental data-fit was 0.9959. It was found that the experimental and simulated data agreed to within 15% of the values obtained from the experimental data-fit.

The method of increasing the magnitude of the modulation index by the pressurisation of the reference gas cell was also investigated. It was found experimentally that with a measurement gas cell containing 100% CO_2, an improvement factor of 1.88 for the modulation index response was obtained by the pressurisation of the reference gas cell to 6 bar. However, the experiments also found that the improvement factor would decrease with decreasing measurement gas cell concentration. At 20% measurement gas cell CO_2 concentration it was found that the improvement factor would decrease to 1.46. Due to the noise inherent in the experimental apparatus it was not possible to show the levelling off of this improvement factor at lower measurement gas cell CO_2 concentrations that was predicted by simulation.

Results from experiments that had the objective of showing the increased sensitivity of the modulation index to H_2O vapour in the measurement gas cell, with increasing reference gas cell pressure, were also presented. The effect of the introduction of N_2

gas, saturated with H_2O vapour, into the measurement gas cell was analysed at an elevated reference gas cell pressure. A dependence of -2.97×10^{-4} bar^{-1} was found experimentally. The result obtained for this by simulation was $-7.51x10^{-5}$ bar^{-1}, which is smaller than the experimentally observed value by a factor of 4. The experimental results also showed that whereas an improvement by, at most, a factor of 1.88 would be obtained in CO_2 measurement at a reference gas cell pressure of 6 bar, the crosstalk with H_2O saturated N_2 would deteriorate by a factor of 6.

Finally, results from an experimental investigation of the dependence of the modulation index on the temperature of the measurement gas cell were presented. The experiment showed a sensitivity of modulation index on measurement gas cell temperature of $1.6\%°C^{-1}$, whereas the simulation suggested a sensitivity of $0.26\%°C^{-1}$. Thus the result from experiment was a factor of 6 times larger than the result from simulation. The principal factors which were likely to cause this disagreement were outlined and are discussed further in Chapter 9.

Chapter 7

System Performance Analysis

7.1 Introduction

In this chapter the factors that affect system performance are analysed from both a theoretical and experimental viewpoint. The system analysis comprises a system power budget, an analysis of the feedback system employed and a noise evaluation of the system.

Additionally, a method of constructing a multi-pass gas cell is described and some results, taken using this multi-pass gas cell, are presented. The reasons why it was decided to revert to a single pass gas cell are then discussed.

7.2 System Power Budget

In this section the system power budget is analysed from both a theoretical and an experimental standpoint, and then the results are compared and the differences discussed.

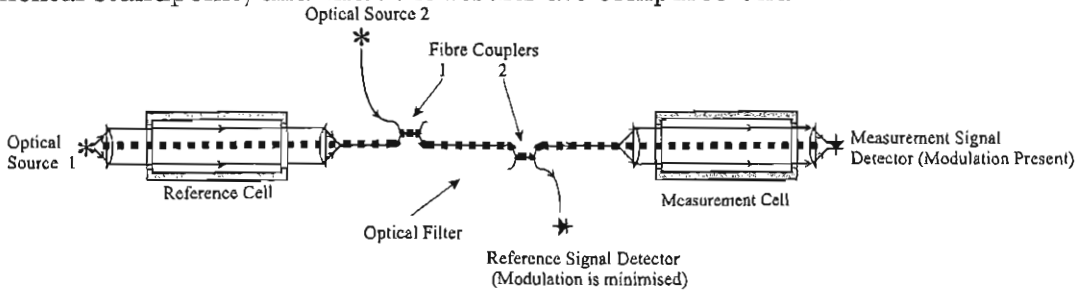

FIGURE 7.1: Schematic of a fibre optic implementation of a correlation spectroscopy system. The optical path, over which the greatest attenuation is considered to occur, is shown by the dotted line.

7.2.1 Theoretical Power Losses

From Figure 7.1, which shows the topology of the correlation spectroscopy system used, it may be observed that the greatest loss will occur on the path from optical source 1 to the measurement signal detector, which sequentially traverses most of the system components, ie. the reference gas cell, the two optical couplers and the measurement gas cell. The principal loss mechanisms are considered to be the coupling of light in and out of the reference and measurement gas cells, and through the two optical couplers. The losses that would occur on this optical path are now individually analysed.

7.2.1.1 Optical Power Losses associated with the Reference Gas Cell

The first stage of the optical path from optical source 1 is the coupling of light into the reference gas cell from the "LED20" LED. Owing to the design of the reference gas cell that constrained where the LED could be positioned, and in order to enable the LED to be directly coupled to the reference gas cell, two Edmund optics aspheric lenses with 6 mm diameter and 9 mm focal length, were used to focus the optical power from the LED to the 9 mm diameter input lens of the reference gas cell. However, in order to simplify the analysis, the LED is modelled as being located at the focal distance of the input lens, with the expectation that this approximation would lead to a higher predicted power than would be found with the experimental apparatus, as shown by Figure 7.2.

The LED was modelled as being 9 mm behind the input lens to the gas cell. The LED may be approximated as having uniformly distributed emission with the observation angle and as the maximum viewing angle being is of the order of 90°, the total emitted power from the LED may then be assumed to possess a hemispherical emission profile. The optical power coupled into the circular 9 mm lens may be modelled as possessing a disc-shaped profile. Therefore the ratio of the optical power generated to the optical power coupled into the 9 mm diameter lens may be calculated as the ratio of the area of the 9 mm diameter lens to the area of the surface of the hemisphere, with a 9 mm radius. This equates to 12.5% of the optical power being transmitted, or a power loss of -9.0 dB.

The Numerical Aperture (NA), which is the sine of the angle subtended to the perpendicular plane by the extreme meridional optical rays, of the light coupled into the lens, may be described by the optical rays shown in Section A of Figure 7.2, and was calculated as being 0.5.

The relationship between the numerical aperture and diameter of the input fibre, and the beam diameter and divergence of the output beam, may be mathematically described. These relationships have been reviewed in reference [44], and are used in the following

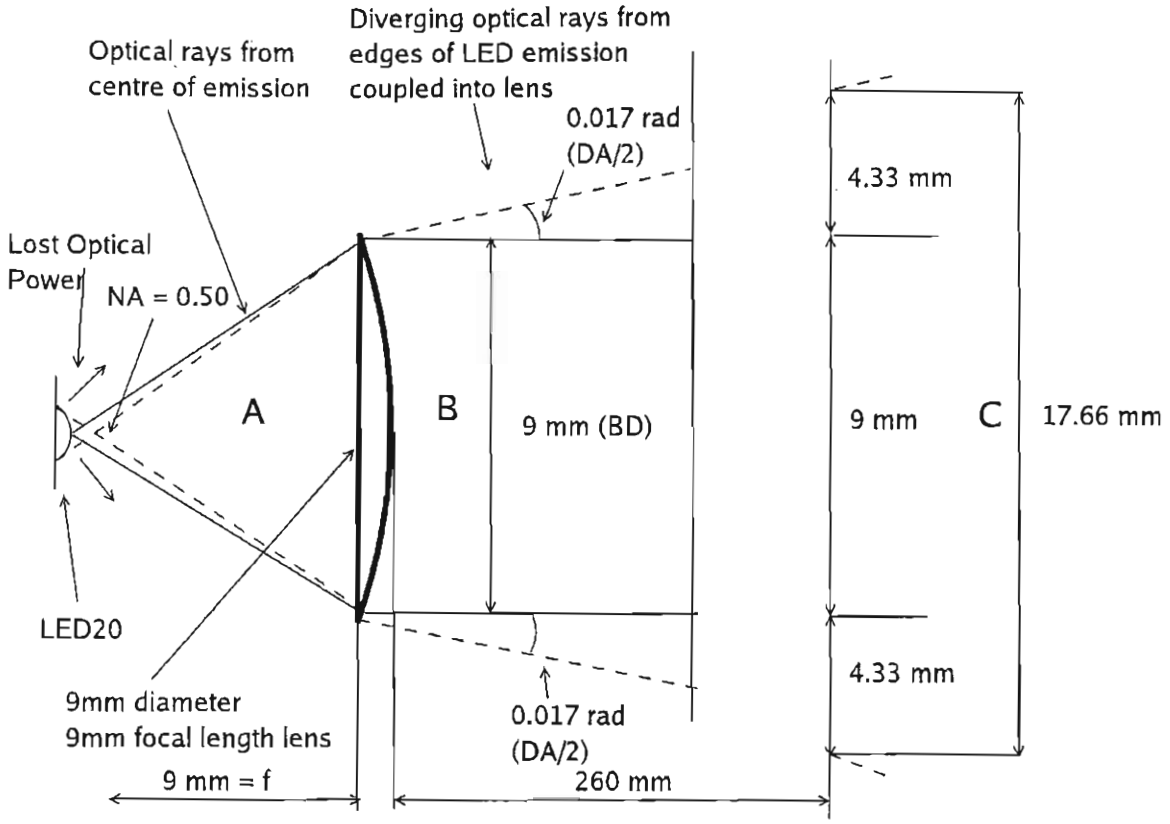

FIGURE 7.2: Diagram of the optical arrangement used to couple light from the LED20 LED into the reference gas cell. The theoretically derived beam NA and the theoretical beam dimensions at the end of the 26 cm long reference gas cell are shown (diagram is not shown to scale).
A: The loss due to light from the LED not hitting the input optical lens.
B: The angles of divergence that will occur after the input lens.
C: The beam dimensions at the end of the reference gas cell.

analysis. The pseudo collimated optical beam, after the 9 mm focussing lens, may be shown to have a beam diameter (BD) described by the equation $BD = 2 \times f(mm) \times NA$ and a Divergence Angle described by $DA(rad) = \frac{a(mm)}{f(mm)}$, where f is the focal length of the lens, NA is the Numerical Aperture of light originating from the source and a is the diameter of the emitting surface.

At Section B of Figure 7.2, the expected divergence of the now pseudo collimated beam is indicated. The Beam Diameter (BD) of this optical beam is 9 mm. However, as the beam progresses across the reference gas cell it will expand at an angle of 34 mrad. This results in a beam diameter, after the traversal of the 26 cm reference gas cell, of 17.66 mm, as shown at Section C of Figure 7.2.

The acceptance angle of the lens-optical fibre arrangement at the end of the reference gas cell is shown in Figure 7.3. This is effectively the reverse of the launching criteria described above, except that the NA of the optical fibre, which is 0.37, governs the size of the diameter of the beam that will be coupled into the optical fibre. The beam diameter of the acceptance cone and the beam at the end of the reference gas cell are 6.66 mm and 24 mm respectively. Consequently, the optical power launched into the exit optical

fibre of the reference gas cell will be the ratio of the areas of the two optical beams, which corresponds to an optical transmission of 7.7%, or a power loss of -11.1 dB.

Thus the total power loss of the reference gas cell will be the addition of the power loss, in dB, from the LED and the power loss of the optical coupling into the optical exit fibre. The power loss of the optical power generated by the LED, to that transmitted from the reference gas cell, is consequently -20.2 dB.

7.2.1.2 Optical Power Losses Associated the Optical Couplers

The optical couplers were assumed, for this power budget analysis, to split the incoming light into 50% in each exit arm. Hence reducing the available power by -3 dB in each coupler.

As was shown in Section 6.2.1, of Chapter 6, by assuming that the power transmission at 1.5 μm is lossless, an additional power power loss by a factor of 4, or -6 dB, may be assigned to each of the two optical fibre couplers. Therefore, the total loss that is experienced through the two optical couplers in series is -18 dB.

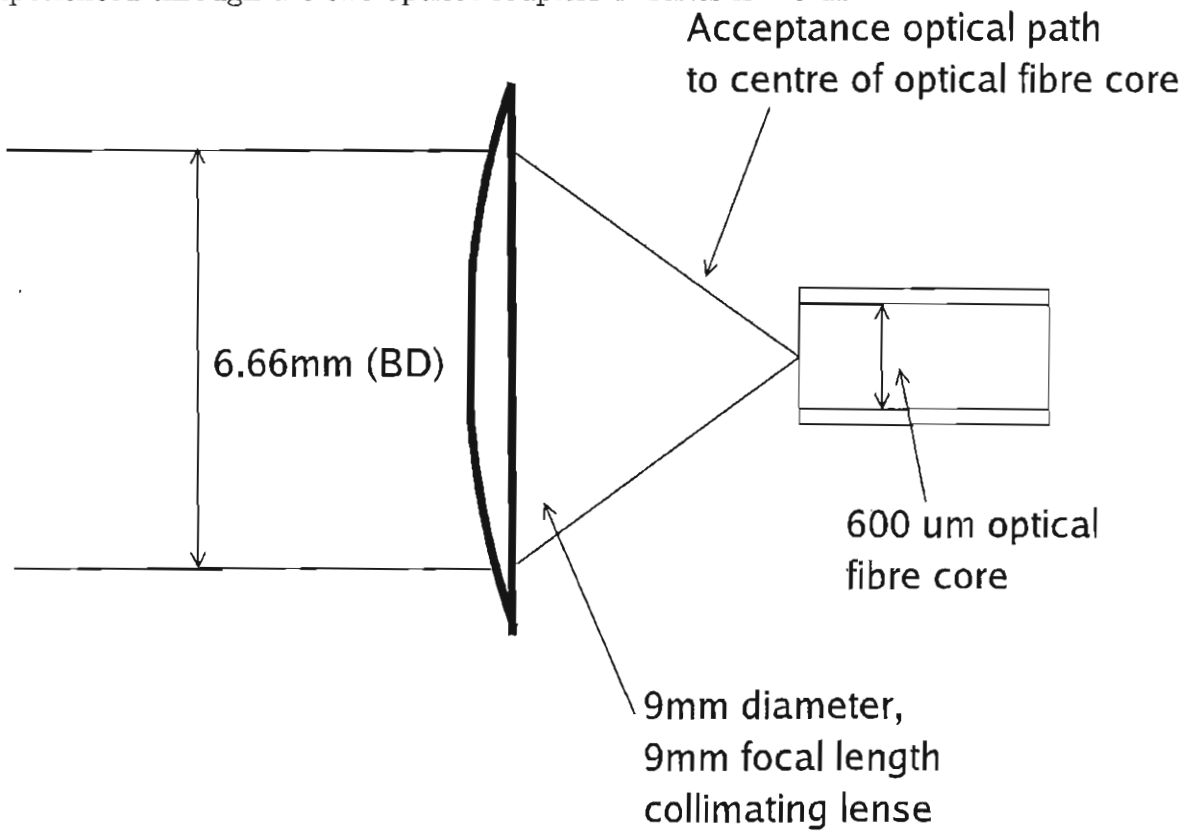

FIGURE 7.3: The expected acceptance beam diameter of the optical lens/Newport Sensor Grade 600 μm diameter fibre coupling arrangement.

7.2.1.3 Optical Power Losses associated the Measurement Gas Cell

The measurement gas cell, a schematic of which was shown in Figure 6.5 in Chapter 6, consisted of a launch optical fibre, a collimating optical lens, a focusing optical lens and an optical detector.

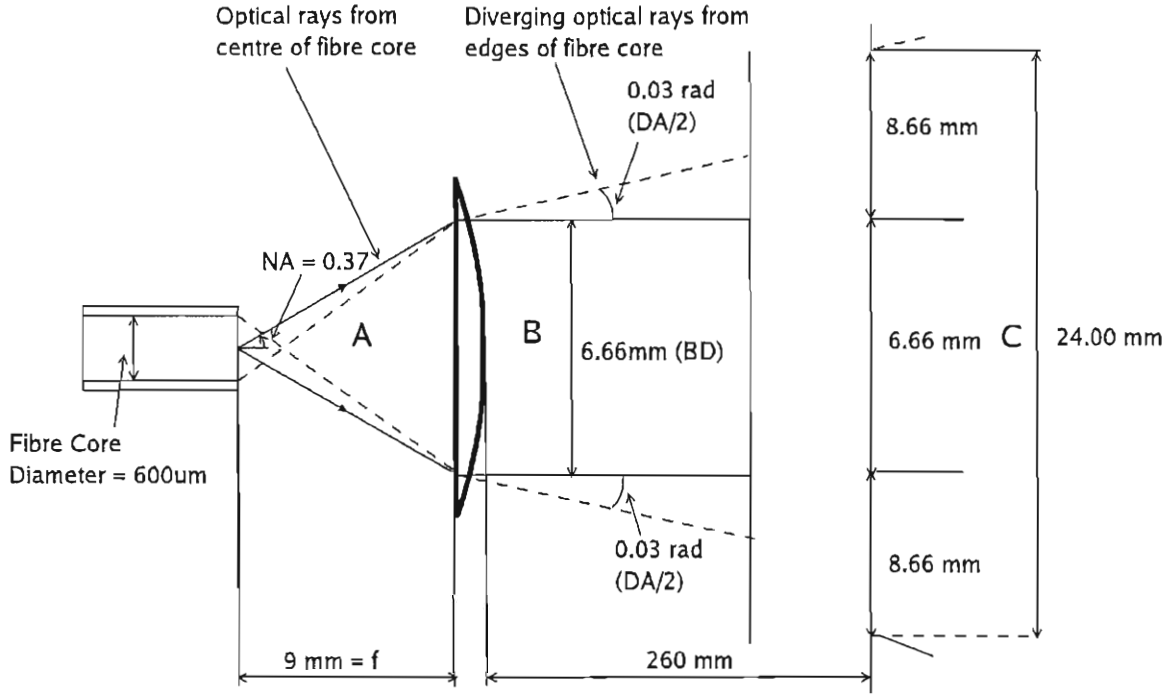

FIGURE 7.4: Theoretical beam divergence angles and dimensions of the fibre/lens launch arrangement used in the measurement gas cell.

The optical coupling from the optical fibre into the measurement gas cell is shown in Figure 7.4; this is the reverse process of the coupling into the optical fibre shown in Figure 7.3. Using the same analysis as above, it may be shown that an optical beam of diameter 6.66 mm will be launched into the measurement gas cell. The angle of divergence is 0.06 rad. This will result in a total beam diameter of 24 mm at the end of the measurement gas cell.

The final stage is the coupling of the optical beam, which has traversed the measurement gas cell, to the optical detector photodiode. In Figure 7.5 the focussing lens is assumed to collect all the optical power across its 9 mm diameter. The means that at this stage 14% of the power contained within the optical disc is collected and passed to the optical detector photodiode, ie. the power loss caused by the measurement gas cell is -8.5 dB.

7.2.1.4 Total Theoretical Optical Power Loss

The losses attributed to the reference gas cell, the optical couplers and the measurement gas cell are shown in Table 7.1. It was shown that the total theoretical power loss,

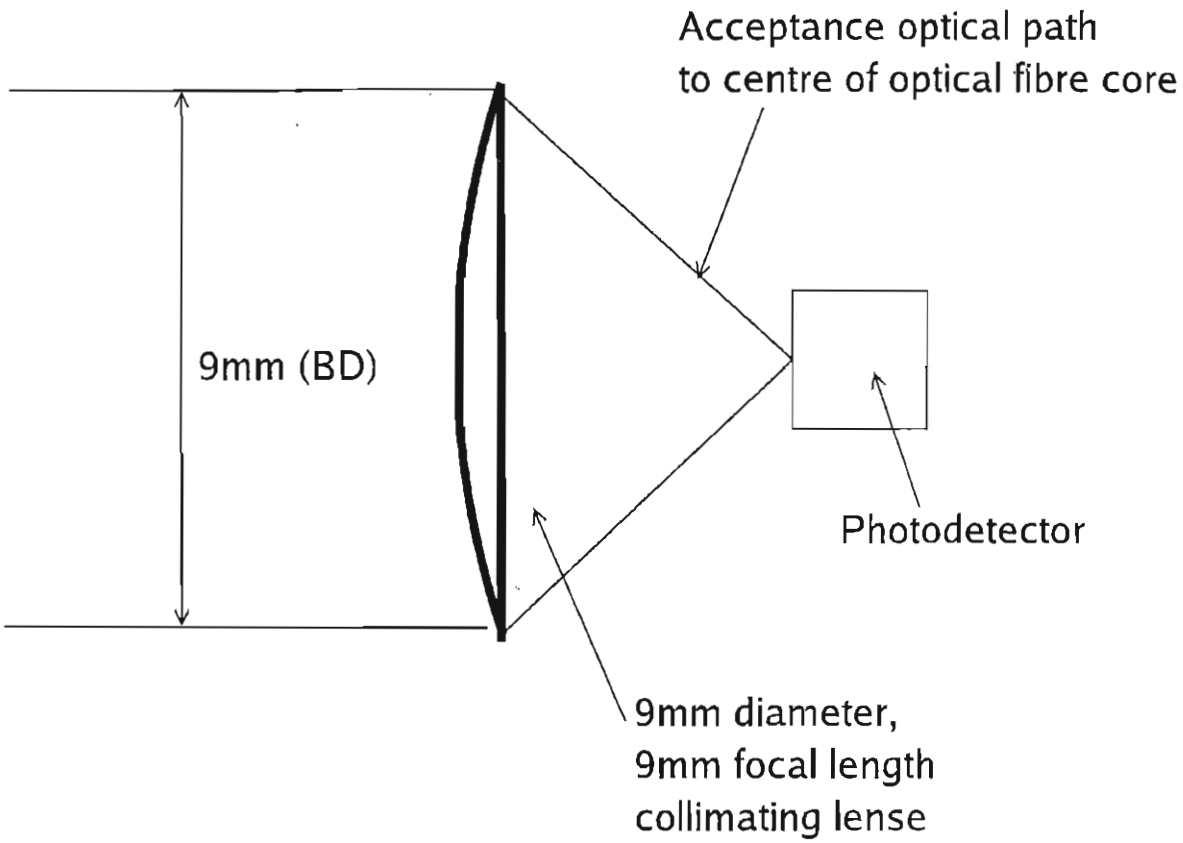

FIGURE 7.5: Theoretical acceptance of optical beam to the measurement detector at the end of the measurement gas cell.

accounted for from optical source 1 to the reference detector, was -38.3dB and to the measurement signal detector was -46.8 dB.

System Component	System Component Loss Factor	Total Loss Factor
Reference Gas Cell Loss Factor	-20.2 dB	
Loss factor through the 2 Optical Couplers	-18.1 dB	
Loss Factor at Reference Detector		-38.3 dB
Measurement Gas Cell Loss Factor	-8.5 dB	
Loss factor from Ref. Det. to Measurement Det.		-8.5 dB
Total Loss Factor at Measurement Detector		-46.8 dB

TABLE 7.1: Theoretical loss factors at reference and measurement detectors.

7.2.2 Optical Power Losses Observed by Experiment

The power losses, that were observed by experiment are shown in Table 7.2. It may be observed that, assuming the "LED20" LED was emitting 1 mW of power, as specified on the data-sheet, the loss factor experienced at the reference detector was 3333 (calculated from 0.7 V from a Hamamatsu extended InGaAs G8373-01 detector,with a sensitivity of 1.1 A W^{-1} and a transimpedance amplifier with a feedback resistance of 10 MΩ, giving a resultant power level of 70 nW) . The power level received at the measurement detector was 2.2 nW (calculated from 195 mV from a Hamamatsu extended InGaAs G8373-01 detector, with a transimpedance amplifier with a feedback resistance of 100 MΩ), which corresponds to a loss factor of -56.6 dB. The reasons for the differences between the experimental figures and the figures obtained by theoretical approximation are discussed in the following section.

System Measurement Point	Loss Factor
Loss Factor at Reference Detector	-41.5 dB
Loss factor at Measurement Detector	-56.6 dB
Loss Factor from Reference Detector Loss to Measurement Detector	-15.0 dB

TABLE 7.2: Experimentally observed loss factors at reference and measurement detectors.

7.2.3 Comparison of Theoretical and Experimentally Observed Optical Power Losses

The comparison of the theoretical loss factors and the experimentally observed loss factors are shown in Table 7.3. The table shows the loss factors at each stage for the system and those theoretically derived, leading to the cumulative loss factor of the complete system. The difference factors between those obtained by experiment and those obtained from theory are also shown.

System Measurement Point	Theoretical Loss Factor	Experimental Loss Factor	Difference ($\frac{Experiment}{Simulation}$)
Loss Factor at Reference Detector	-38.2 dB	-41.5 dB	-3.3 dB
Loss Factor Between Reference Det. and Measurement Det.	-8.5 dB	-15.1 dB	-6.6 dB
Loss factor at Measurement Detector	-46.7 dB	-56.6 dB	-9.9 dB

TABLE 7.3: Comparison of theoretical and experimentally observed loss factors at the reference and measurement detectors.

The disagreement factors shown in the above equations may be attributable to the following considerations:

- Experimental error in the alignment of the apparatus.
- Reflections/Alignment at optical interfaces (fibre-air, air-lens, lens-air, air-fibre, FC-fibre connector couplers).
- Approximations used in the above analysis, as described in Section 7.2.1.1.
- Attenuation of Newport, sensor grade, F-MBD optical fibres.
- Attenuation of and unequal splitting of the optical couplers.

7.3 Design of Feedback Control Loop

A block diagram of the feedback control mechanism is shown in Figure 7.6, which was designed and constructed by Dr. E. A. D. Austin. The figure shows that the difference of the optical powers received from optical sources 1 and 2 is fed into a buffer and then fed back as an intensity modulation for optical source 2, in order to reestablish an equal received intensity at the reference detector.

The feedback control mechanism, consisted of a averaging filter which collected 100 data-points (the first 20 values recorded were neglected in order to minimise any switching effects) and the averaging filter returned values at the rate of 500 Hz. The data was then passed to a DSP biquad controller, which is described later in this section.

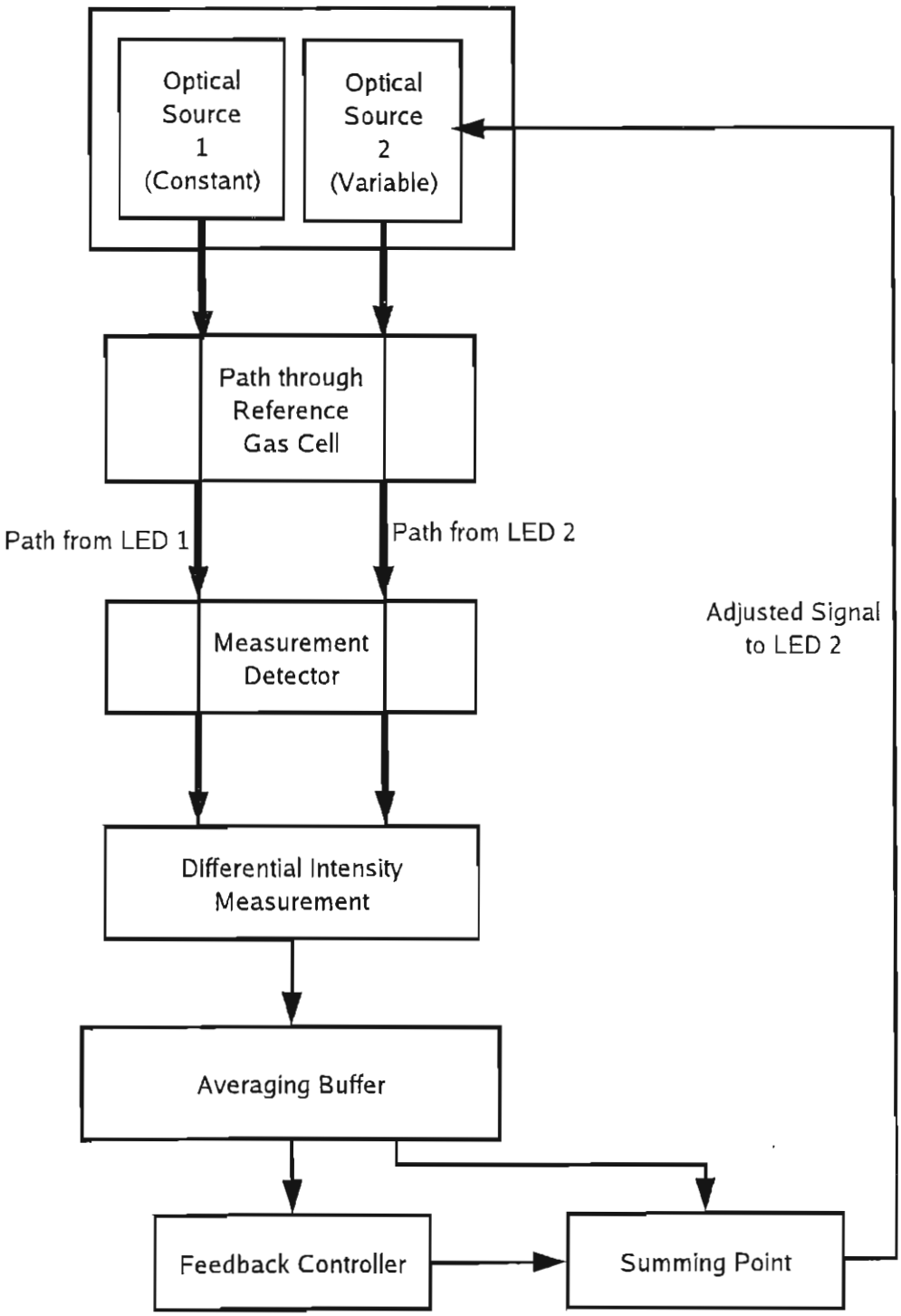

FIGURE 7.6: The schematic of the feedback system design.

The measurement signal was fed into a 100 point data averager, which again returned values at the rate of 500 Hz. The time constant of the averaging filter was 250 s ($\frac{1}{2\tau}$, where τ is the 2 ms integration time). The data were multiplied by the switching square wave in order to form a lock-in amplifier. The values returned were then passed to a single pole low pass filter with a time constant of 10 s. The post detection bandwidth of this single pole low pass filter may be shown to be 0.025 Hz($\frac{1}{4\tau}$, where τ is 10 s). The explanation of the time constants is shown in Appendix A of the paper by Eppeldauer and Hardis [38]. The averaging filter will result in a frequency response roll-off at higher frequencies, while the low pass single pole filter will dictate the system response at lower frequencies, which are visible in the traces shown. The 0.025 Hz bandwidth given by the low pass filter is considered to dominate the low-mid frequency system noise characteristics.

In an attempt to minimise the noise from the feedback controller, an implementation based on a DSP biquad filter, designed by this author, was used. A schematic of the controller is shown in Figure 7.6. The background theory of digital signal processing is covered in several text books such as [45]. Experiments with varied pole/zero locations of a biquad filter were carried out, and it was found that the filter shown in Figure 7.7 yielded an optimal response.

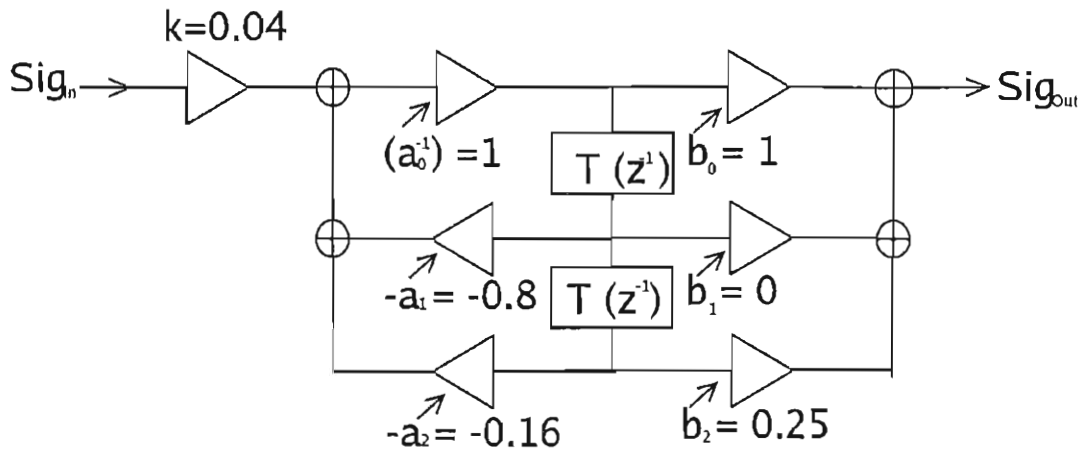

FIGURE 7.7: The DSP biquad filter that was found to yield an optimal response for the feedback control of the correlation spectroscopy system used. The blocks labelled T represent a unit time delay and the variables k,a_0,a_1,a_2,b_1,b_1 and b_2 represent the multiplication scalars of the values at the points in the filter shown.

The transfer function, $H(z)$, of the filter shown in Figure 7.7, may be expressed in terms of z, the equivalent of the Laplacian unit (s) in the discrete time sampled data domain, by the equation:

$$H(z) = k\frac{a_0 + a_1 z^{-1} + a_2 z^{-2}}{b_0 + b_1 z^{-1} + b_2 z^{-2}} \tag{7.1}$$

With the substitution of the scalar values for k,a_0,a_1,a_2,b_1,b_1 and b_2, the transfer function may be shown to be:

$$H(z) = 0.04\left(\frac{1 + 0z^{-1} + 0.25z^{-2}}{1 + 0.8z^{-1} + 0.16z^{-2}}\right) \tag{7.2}$$

This equation may be factorised to reveal the location of the zeros and poles associated with the filter:

$$H(z) = 0.04\left(\frac{(z + \frac{j}{2})(z - \frac{j}{2})}{(z + 0.4)(z - 0.4)}\right), \tag{7.3}$$

where $j = \sqrt{-1}$. Thus there are two zeros associated with this filter located at $z = \pm\frac{j}{2}$ and two poles associated with this filter located at $z = \pm 0.4$.

This result suggests that the two poles located towards the DC level (at $z = 1$) and the Nyquist frequency, the highest frequency that the filter can access, were responded to in a proportional integral fashion. The fact that the two zeros were located in the central band of the filter frequency response suggests that the feedback system's response at these mid-band frequency locations was damped down.

7.4 Sources of Noise

In this section the fundamental sources of noise are considered and the relative magnitude of their contribution to the total noise of the system is estimated. The arrangement of the transimpedance amplifier used at the measurement detector is shown in Figure 7.8, where the OPAMP, photodiode and feedback resistor, which are envisaged as causing the majority of the system noise, are shown. Also, the source noise in the optical source makes a contribution. The noise sources mentioned are individually considered in the following sections.

7.4.1 Resistor Noise

The thermal resistor noise, from the resistance seen by the input terminals (V_{RN}) of the OPAMP, forms a noise voltage at the inverting input. The input resistance is formed by the parallel resistance of the feedback resistance ($R_{Feedback}$) and the photodiode shunt resistance (R_{Shunt}), and is termed R_{SO} for this analysis. The Hamamatsu extended InGaAs G8373-01 photodiode has a quoted shunt resistance of 10 kΩ and the value of the feedback resistance of the transimpedance amplifier is 100 MΩ, therefore

$$R_{SO} = 10\ k\Omega \| 100\ M\Omega = 10\ k\Omega. \tag{7.4}$$

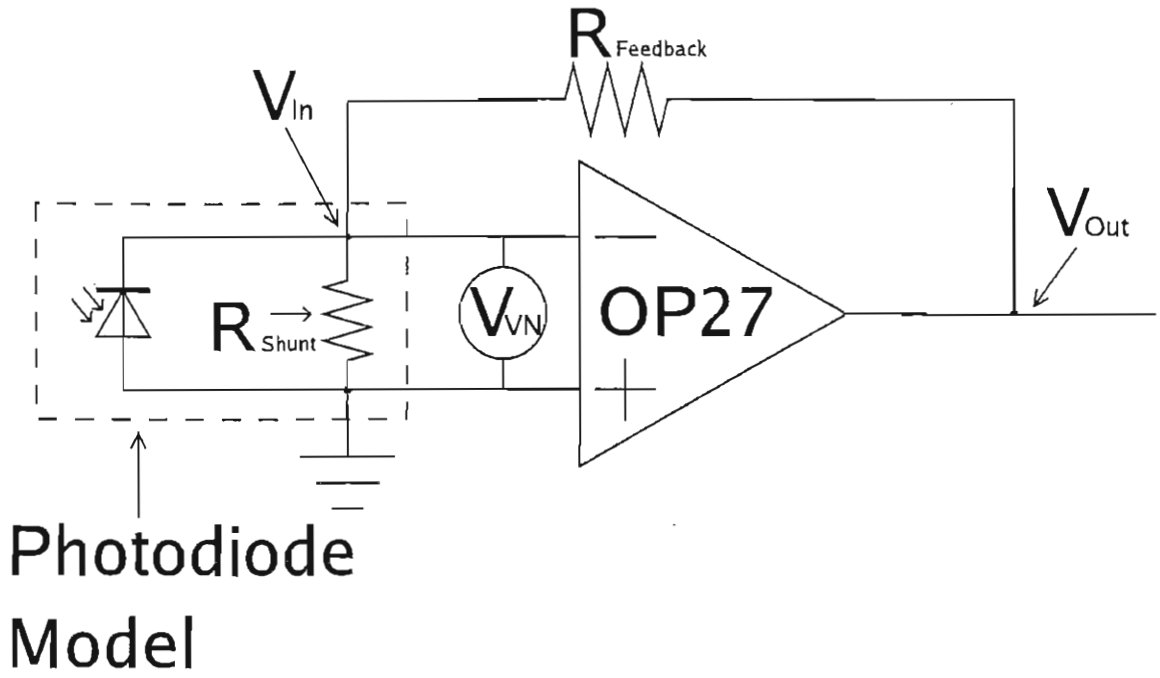

FIGURE 7.8: A schematic diagram of the transimpedance amplifier arrangement used with the measurement detector. The shunt resistance R_{Shunt} attached to the measurement detector, the feedback resistance $R_{Feedback}$ and the OPAMP voltage noise source V_{VN} are shown.

Consequently, using the thermal noise equation

$$\sqrt{4kTR_{SO}B}, \tag{7.5}$$

the RMS value of this noise source may be arrived at as being 13 nV $Hz^{-0.5}$.

7.4.2 Shot Noise

The shot noise (photon noise) describes the random arrival of photons at a detector and is described by the equation:

$$I_{Shot\ Noise} = \sqrt{2qI_{Sig}B},$$

where q is the electronic charge, I_{Sig} is the photocurrent generated and B is the post-detection noise bandwidth. The Analog devices OP27 operational amplifier has a quoted input bias current of 20 nA. Thus, the noise voltage appearing across R_{SO} is:

$$V_{Shot\ Noise} = \sqrt{4qIB(R_{SO})^2}$$

This results in a value for the RMS shot noise contribution of 336 pV $Hz^{-0.5}$.

7.4.3 Source Noise

The noise from an optical source is due to source related intensity or phase fluctuations. These variations have been analytically quantified and described by Tur *et al.* [46]. They derived a method for calculating the relative intensity noise from an optical source. The result from the calculations, shown in this section, describes the contribution of source noise from the "LED20" LED used in the experimental apparatus for the experiments described in this thesis.

$$S_{in}(f) = \frac{0.66 I_0^2}{\Delta v} \tag{7.6}$$

Tur *et al.* [46] showed that the optical source noise may be described by Equation 7.6, where Δv is the FWHM bandwidth (in Hertz) of the emission from the source, and the optical power from the source is I_0. The result, shown in Equation 7.6, assumes that the emitted light spectrum is Gaussian shaped. The FWHM bandwidth from the LED20 LED is 13 T Hz (175 nm bandwidth at 2.0 μm) and the received power from the LED at the measurement detector was 2.8 nW. With these parameters inserted, the result shown in Equation 7.7 is reached.

$$S_{in}(f) = \frac{0.66(1\ mW)^2}{13\ T\ Hz} = 5.076 \times 10^{-23}\ W^2\ Hz^{-1} \tag{7.7}$$

This leads to an expected contribution to the total noise of the system of 7.12×10^{-12} A Hz^{-1}, assuming the detector responsivity of the Hamamatsu G8373-01 is 1.1 A W^{-1}. In order to convert this noise current into a noise voltage, the result can be multiplied by R_{SO}, yielding a result of 7.84 pV Hz^{-1}. Also, from this result, the value of the Relative Intensity Noise (RIN), which gives the RMS magnitude of the source noise in the final measurement. The RIN may be evaluated from the equation $\frac{S_{in}}{I_0^2}$, which with the parameters stated above, equates to 1×10^{-3}.

7.4.4 Switching Noise from LEDs

The switching of the LED was achieved by placing a switching transistor in parallel with the "LED20" LED which was driven with the square wave switching signal. This signal was investigated by analysing the rise time of the switching signal and it was found that the rise time of the switching square wave was of the order of 30 ns.

From the "LED20" data-sheet, the LED was shown as capable of being driven with a frequency of the order of 200 kHz. Combined with the fact that the first 20 samples of

the 100 sample measurement, made for each measurement, were discarded, it is therefore assumed that the LED switching noise was not a significant contribution to the overall noise of the system.

7.4.5 Combined Noise Power

The magnitudes of the noise powers considered are listed in Table 7.4. As was described in Section 7.3, the post detection noise bandwidth for the system was assumed to result from the measurement single pole, low pass filter and to be 0.025 Hz ($\frac{1}{4\tau}$, where τ =10 s).

Noise Type	Magnitude	
Resistor Thermal Noise	13 nV $Hz^{-0.5}$	2.02 nV
Shot Noise	335 pV $Hz^{-0.5}$	53.0 pV
Source Noise	3.31 pV $Hz^{-0.5}$	523 fV
Total Noise		2.1 nV

TABLE 7.4: The magnitudes of the considered voltage noises at the inverting input of the OPAMP. The noise voltages shown assume a post-detection bandwidth of 0.025 Hz (corresponding to an integration time of 10 s).

Table 7.4 shows that the dominant noise source was the thermal noise associated with the shunt resistance of the photodiode. The OPAMP voltage noise, shot noise at the detector and the source noise were of successively less importance.

In order to obtain an expression for the noise component of Vo, the above noise sources are subject to the gain of the inverting amplifier, formed by $R_{Feedback}$ and R_{Shunt}, which has a gain of $10^4(\frac{100M\Omega}{10k\Omega})$. This results in a total RMS noise voltage, at the output of the transimpedance amplifier, of 21 μV.

The measurement photo-current, derived from the measurement, is considered to be amplified by the transimpedance amplifier in its normal mode of operation ($V_O = I_{Sig}R_{Feedback}$). With a detected signal power of 1.95 nW, this leads to a detected photovoltage 195 mV. The magnitude of the AC signal variation may be expressed as the DC signal level multiplied by the modulation index.

It was shown by simulation and experiment, in chapters 5 and 6, that a correlation spectroscopy system, with the reference and measurement gas cells containing 100% CO_2 at 20°C and 1 bar, would yield a modulation index of 0.017. Therefore, the AC modulation, of the mean received DC level of 195 mV at the measurement detector, is 3.4 mV. The comparison of this AC signal modulation to the RMS noise voltage is considered to be the SNR of the system. Therefore the SNR, with 100% CO_2 in the measurement gas cell at 1 bar, is,

$$\frac{Mean\ DC\ Voltage\ Level \times Modulation\ Index}{RMS\ Noise\ Voltage} = \frac{195\ mV \times 0.017}{21\ \mu V} = 158. \tag{7.8}$$

7.4.6 Experimentally Observed Noise

In Section 6.3.4 of Chapter 6, it was shown that the RMS SNR observed during the active time segments was 65. The RMS SNR predicted by theory was 158. Consequently, the experimentally observed value was 41% of that predicted by theory. Potential reasons to account for the difference would be the variations in the shunt impedance of the photodiode, due to manufacturing constraints, or drifts occurring within the experimental apparatus. The feedback system would also be an additional source of systematic noise.

7.5 3-Pass Gas Cell

A design of a compact gas cell was investigated. This implemented a method of using two concave mirrors to form a three-pass gas cell. However, it was decided to convert the gas cell to a single-pass arrangement in order to clarify some of the experimental results. The design of the gas cell, the experimental results obtained and the reasons why it was decided to revert to single-pass gas cells are presented in this section.

7.5.1 The Gas Cells

The schematic of the gas cell in its three-pass configuration is shown in Figure 7.9. The gas cell consisted of two concave mirrors, each with a focal length of 52 cm, positioned facing each other 26 cm apart. It was assumed that, with appropriate adjustment of the position of the optical fibre ferrules and the concave mirrors, the majority of the optical power would travel via a three-pass and the remainder would travel via a single-pass. This was envisaged as yielding an effective path-length of approximately 80 cm. The adjustment of the position of the concave mirrors and the fibre ferrules was allowed for by the compressibility of the neoprene O-rings.

7.5.2 Discussion

The optimal results that were obtained from a measurement sensitivity perspective, are shown in Figure 7.10. The time scales described in Table 6.2, in Chapter 6, were observed for the experiment. For the measurements shown, the received optical power

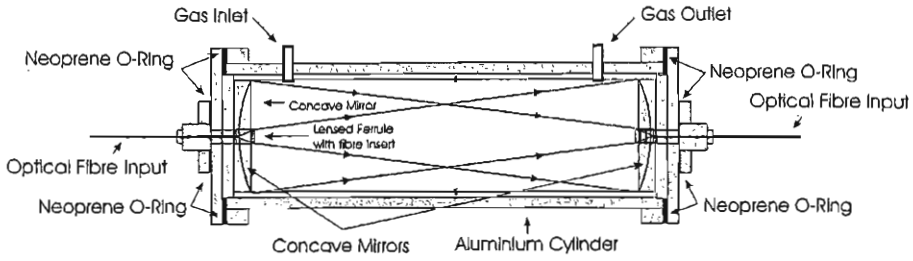

FIGURE 7.9: A schematic diagram of the gas cells, of length 26 cm, used during these experimental investigations. The effective length of the gas cells in this configuration was assumed to be approximately 80 cm. It was envisaged that the light would principally travel via the path shown on the schematic.

Optical Path	Modulation Index	% of received optical power % that traversed optical path
3 pass (80 cm)	0.0573	57%
1 pass (26 cm)	0.0176	43%
Observed Measurement (55 cm)	0.043	

TABLE 7.5: The relative magnitudes of the optical powers that have traversed the 3-pass and single pass optical paths.

at the measurement detector was 1100 nW (derived from 1 V falling on a Hamamatsu extended InGaAs G8373-01 detector, with a transimpedance amplifier with a 100 MΩ feedback resistor). The RMS noise of the modulation index during the active measurement time-slots (as previously defined in Table 6.3, of Chapter 6) was 0.25 mV. Using the modulation index, observed with a measurement gas cell concentration of 100% of 0.043, a SNR of 155 may be arrived at from the measured results, corresponding to an approximate CO_2 sensitivity of 0.6%. This result was obtained using a single-pole low-pass filter as the feedback controller and the measurement low-pass filter with time constants of 1 s.

However, as it was found that the modulation index observed, 0.043, was approximately 70% of the modulation index predicted by simulation, it was decided to revert to a single path configuration, so that the experimental results obtained could be compared to the results obtained by simulations based on Hitran data with no ambiguity as to the pathlength of the gas cells.

If the optical power that arrives at the measurement detector is considered to consist of components that have traversed the 26 cm single pass, and the 80 cm 3 pass optical paths of each of the gas cells, the ratio of the received optical power that has traversed each path may be derived. The result of the calculation, based on simulations using the Hitran data, to calculate this ratio is shown in Table 7.5.

The result suggests that approximately 57% of the optical power received had traversed the 3 pass optical paths, while the remaining 43% had traversed the single pass optical

paths.

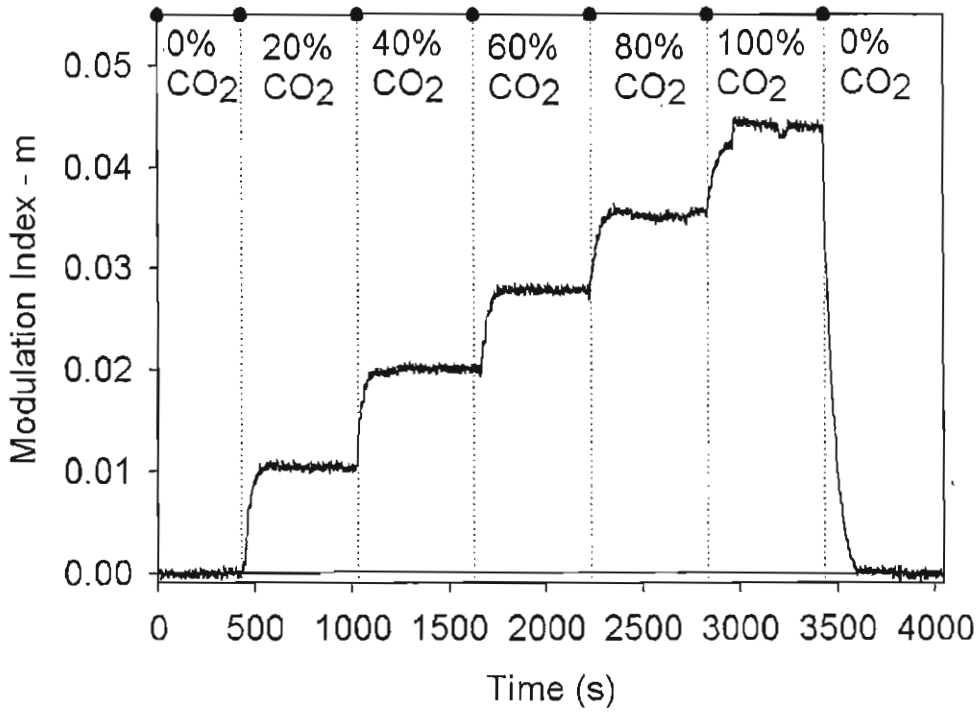

FIGURE 7.10: 3-pass experimental results describing the effect of varying CO_2 concentration in the measurement gas cell on the modulation index. The reference and measurement gas cells were both held at a total pressure of 1 bar and a temperature of 20°C.

7.6 Conclusions

In this chapter the power budget of the correlation spectroscopy system has been analysed theoretically and experimentally. It was found that, by theory, a power loss for the system of -46.7dB would result. The theoretical loss was attributed to the optical coupling through the reference gas cell, the loss associated with the optical couplers and the loss associated with the measurement gas cell. However, from experimental measurements it was found that the experimental power loss was -56.6 dB. Thus, showing a difference of 9.9 dB. This difference is assumed to be due to a combination of the error associated with aligning the apparatus, the optical absorption and reflection of the optical components (optical fibres, lenses and fibre-couplers) in the system.

The feedback system used was described. This included a description of the feedback control algorithm and the procedure that was followed to optimise it. This optimisation was carried out to minimise the noise introduced by the feedback controller.

A noise analysis of the system was also shown. The OPAMP voltage noise at the inputs of the OPAMP was shown to be the dominant noise source. This resulted in an SNR in

the measurements that were obtained of 65, corresponding to a CO_2 detection sensitivity of approximately 1.5% (vol/vol). The sensitivity limit would be improved by increasing the optical power detected at the optical detectors. This could be achieved, for example, by using more spectrally intense optical sources or increasing the diameter of the input and output lenses of the optical system. With increasing detected optical power, the system would become resistor thermal noise, shot noise and eventually source noise limited.

A method of constructing a 3-pass gas cell was also described. Results taken using this gas cell were shown. The reasons why it was decided to revert to a single pass gas cell were outlined, which primarily were to enable simulation and experiment to be compared with the ambiguity of gas cell path-length removed.

Chapter 8

Conclusions

The aim of this thesis was to describe the operation of a correlation spectroscopy gas detection system and to show a comparison of simulations based on Hitran data and the experimental results obtained from a correlation spectroscopy gas detection system. The way in which this was achieved and the principal results obtained are reviewed in this chapter.

In order to introduce the background development of correlation spectroscopy, Chapter 2 contained a review commonly used gas detection systems, with an emphasis on optical gas detection systems related to correlation spectroscopy. Following a description of the basic principle of the correlation spectroscopy method, a mathematical derivation of the defining equation of the "modulation index" was presented in Chapter 3. Using this equation the operation of a correlation spectroscopy system was shown by use of an approximated gas absorption spectrum. This approximation allowed the fundamental responses that were found by simulation and experiment, as described in subsequent chapters, to be anticipated.

A description of the physical phenomena that cause the infrared absorption of gases in the infrared was given in Chapter 4, followed by a description of the Hitran database, since this was the source of the spectroscopic gas absorption data used in the simulations. The effects that temperature and pressure changes in the gas cells would have on their transmission spectra were presented in graphical form. In order to quantify the accuracy of the Hitran data for the CO_2 absorption at around 2 μm, an experimental observation experimental observation showed that the RMS difference between the Hitran data and experimental data was 0.4%. This "good" agreement justified the use of the Hitran data in simulations of the correlation spectroscopy CO_2 detection system, the results of which were shown, and compared with experiment, in subsequent chapters.

Results from simulations that were carried out to characterise correlation spectroscopy gas detection systems for CO_2, CH_4 and O_2 gases were shown in Chapter 5. The key

results related to the comparisons of results from simulations and experiments carried out with the objective of characterising a carbon dioxide (CO_2) correlation spectroscopy gas detection system. The operation of the system at room pressure and temperature was examined. The dependence of modulation index on the measurement gas cell CO_2 concentration was analytically assessed. The method of increasing the modulation index to CO_2 target gas by the pressurisation of the reference gas cell was analysed. The experimental and simulated results showed that, by the pressurisation of the CO_2 containing reference gas cell, the modulation index could be increased by approximately a factor of 2. However, it was also shown that the cross-talk from a contaminant gas would also increase. The cross talk to H_2O saturated N_2 gas was found to increase at a greater rate than the increased response to CO_2 target gas.

The sensitivity of the demonstration system showed a peak to peak noise limited detection sensitivity of 3% CO_2 target gas. However, related Gas Filter Correlation type devices have attained CO_2 gas sensitivities of sub ppm levels with the use of a single mechanically chopped high intensity far infra-red optical source (See Teledyne data-sheet [28]). This indicates that with development a substantially lower gas detection limit could be obtained. Future work that could seek to reduce the minimum detectable gas level and the disagreements between the experimental data and the simulated data are discussed in the following chapter, Chapter 9.

In Chapter 7 a system performance analysis was included. This included an optical power budget, which analysed the optical losses that could be attributed to each component. Also a noise analysis was presented. It was found that the majority of the noise observed in the measurements was attributable to the OPAMP and the low shunt impedance of the photodiode used.

In conclusion this thesis has shown the responses of a CO_2 correlation spectroscopy gas detection system. The results presented in chapters 5 and 6 of this thesis will enable the accuracy of simulations of CO_2 correlation spectroscopy gas detection systems to be assessed. The quantification of the potential improvement by the pressurisation of the reference gas cell has also been shown in Section 5.10 of Chapter 5, and in sections 6.4.2 and 6.4.3 of Chapter 6. These results may be of use for industries and researchers in assessing the performance of correlation spectroscopy gas detection systems.

Chapter 9

Future Work

There are some possible topics for further research to extend the work presented in this thesis. These relate principally to the future use of improved spectral source data and the use of improved gas cells.

It is likely there will be updates to the gas absorption spectral databases (Hitran, GEISA, CDSD etc.). The data in these updated databases could be used as the input into simulations to remodel a correlation spectroscopy system. A comparison of these future data with experiment could be made, which might result in a greater agreement between the simulated and experimental results. In particular, the results relating to the dependence of the modulation index on the temperature of the CO_2 measurement gas that show the temperature dependence of the experimental data and the simulated data differed by approximately a factor of 6, could be further investigated. Such an investigation could concentrate on both the accuracy of the Hitran data and software, and the temperature response of the measurement signal optical detector. These are considered the factors in the experiments and the simulations that most likely contributed towards this disagreement.

The comparison in Chapter 6 of the experimental and simulated results describing the cross-sensitivity of a CO_2 correlation spectroscopy system to water vapour in the measurement gas cell, with pressurisation of the reference gas cell, showed a disagreement between experiment and simulation by a factor of 4. Again, this difference could have resulted from an error in the experiment, or the Hitran data representing the CO_2 absorption or the H_2O absorption.

In Chapter 7 a method of constructing a 3-pass gas cell was shown. However, it was also mentioned that there was a ambiguity in finding the effective path-length of the gas cell. An area of future work could be the design and development of multi-pass gas cells with the objective of enabling a longer path-length in order to enable a larger modulation index to be obtained. Accompanying this, methods to quantify the length

of these gas cells could be developed using, for example, a white-light interferometric optical approach or the time of flight of a laser pulse. The area of gas cell development using Photonic Crystal Fibres (PCF) with the target contained in the holes, resulting in compact gas sensing systems, could be investigated. This system could also make use of laser technology, in order to give higher source powers, and could result in substantially improved sensitivities to low target gas concentrations. The implementation of a correlation spectroscopy system with PCF reference cells would also aid the implementation of an optically switched system containing multiple reference gas cells, making the resulting system potentially sensitive to multiple gases. These gas cells could also enable the received optical spectral power of 0.01 nW nm^{-1} that was observed in the experiments described in this thesis to be increased, consequently improving the gas sensitivity.

Appendix A

Optimisation of Spectral Power Output from an LED Source for Sensor Applications

The potential spectral power improvements that may be obtained from a LED by cooling and pulsing at a specified wavelength is a topic that was initially pursued, but not included in the main body of this thesis, since it is not directly related to the operation of a correlation spectroscopy system. This work was published as a journal article in Measurement Science Technology. The text of this article is reproduced on the following pages.

INSTITUTE OF PHYSICS PUBLISHING MEASUREMENT SCIENCE AND TECHNOLOGY
Meas. Sci. Technol. 14 (2003) 2006–2014 PII: S0957-0233(03)62160-0

Investigation of the peak power enhancement available from a surface emitting GaAlAs near-infrared light emitting diode by cooling and pulsing

Paul Chambers, Ed A D Austin, Mark J Gunning and John P Dakin

Optoelectronics Research Centre, University of Southampton, Southampton SO17 1BJ, UK

Received 11 April 2003, in final form 4 August 2003, accepted for publication 26 August 2003
Published 26 September 2003
Online at stacks.iop.org/MST/14/2006

Abstract
Light emitting diode (LED) light sources are required for many illumination and optical sensing applications, due to their compact dimensions, low cost and low power consumption. The optimization of optical power output in a specific wavelength band is often of critical importance. We are interested in using LEDs for optical sensing systems, particularly for gas sensing. We have conducted a very comprehensive engineering study to show that, by packaging a commercial surface emitting LED in a cooled heat-sunk package and optimizing the drive current for this lower temperature, the power from the LED may be substantially improved, particularly when pulsed at low duty cycle. We have found that, even with moderate cooling using a Peltier heat pump, the intensity in our required spectral band was improved by a factor of 5 compared to that attainable under normal drive conditions. We have also verified that almost all spectral changes in the LED were due to temperature changes in the emitting chip, rather than from other effects related to injection current, such as internal optical gain.

Keywords: optical source output power, cooling, LED, optical sensing

1. Introduction

It has been known for many years that the power output of light emitting diodes (LEDs) can be substantially improved by cooling. Much of the improvement occurs due to increased optical output efficiency when cold, but a further significant improvement is then also possible by taking advantage of the much higher bias current that can be applied to a cooled device. When cooled, there is also less risk of thermally-induced destruction of the device.

The enhancement of output optical power from LEDs by cooling to extreme temperatures, and by driving at higher bias currents, has been previously demonstrated [1]. Currently, most LED packages are designed for low cost of production and efficient heat-sinking has been a secondary consideration. With the requirement for brighter LEDs there is an interest in improving their heat-sinking and optimizations of their design to achieve this have been discussed [2]. Prior to this, work typically focused on optimizing device structure and drive current was typically selected to optimize LED output power at room temperature [3]. The benefits of cooling LEDs are rarely made use of in 'real-world' instrumentation systems, despite the fact that compact cooling systems are readily available. We have therefore conducted a rigorous study of how performance might be enhanced in this manner. Taking a particular example of a near-infrared device, we have fully investigated the performance gains to be expected from cooling an LED to a fixed lower temperature (which in itself improves output stability), by driving it at higher bias currents in the cooled state, and we then examined the benefits of low duty cycle pulsed operation. Pulsed drive allows additional optical output power gains because self-heating, which depends on the time-averaged power that is dissipated, is then reduced.

This work includes what we believe is a first comprehensive study of how all these factors can be combined, in a manner relevant for use in real instrumentation.

0957-0233/03/112006+09$30.00

Below we have excellent experimental evidence to show that the emission spectrum of the surface emitting LED we tested proves to be dependent almost solely on the operating temperature of the light emitting region (it varies also with bias current, of course, but only insofar as this causes localized heating). Because of this, the output spectrum should provide an excellent indication of the junction temperature of the device. (Note: in edge-emitting LEDs (ELEDs) changing the injection current significantly affects the optical gain, which can cause dramatic spectral changes, such as line narrowing, and a super-linear increase in output intensity, as drive current is increased.)

Consequently, we expect that spectral monitoring can be used confidently to ensure that our selected surface emitting device is not internally overheating. This is important, because we wish to use a much higher bias current when the package is cooled, and expect to drive it with an even higher peak current when operating the device under low duty cycle pulsed conditions.

Considering the improvements that have been obtained, and despite the wide availability of compact low-cost Peltier coolers, surprisingly little practical system use appears to have been made of cooled LEDs. Other than cost, this is probably due to two reasons: firstly the high power consumption of Peltier coolers, and secondly the need to avoid 'misting up' or icing of optical surfaces by water condensation, when cooled below room temperature. Both of these problems could be reduced in production devices by compact co-packaging of the Peltier cooler, the LED and the attached output waveguide within a thermally insulated package, thereby ensuring in-package hermetic sealing of the emitting surface. A smaller Peltier cooler could then be used, as there would be a significant reduction in heat loss, particularly with vacuum packaging.

For this initial research, as an interim measure, we have directly bonded a polished polymer-encapsulated LED package to a fibre pigtail, hence avoiding an intervening air space, and we have reduced heat loss simply by thermally insulating the LED and the output fibre pigtail by encapsulating them in plastic foam.

Although our work, here, utilizes a specific type of near-infrared surface emitting LED, we believe the general conclusions are likely to be relevant to many other surface emitting LEDs. This has engineering significance for many application areas (e.g. sensors, displays, illumination systems). It is useful to emphasize that our initial aim was to optimize a specific LED source for use in our own correlation spectroscopic sensor for oxygen gas detection, of a type we reported earlier [4].

For this sensor, we require to maximize power in a 2 nm wide wavelength band centred at 761.5 nm. We therefore conducted a detailed study of the behaviour of a cooled Epitex L760-06AU near-infrared 760 nm LED, examining how not only its output power, but also its spectral emission, varies as a function of drive current, duty cycle and package temperature.

2. Light emitting diode theoretical overview

The principles of LED operation are covered in detail in many textbooks [5–7], so here we present a brief overview.

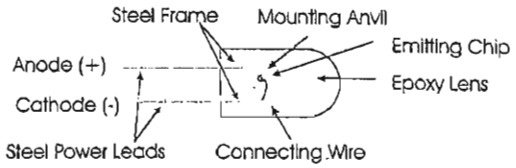

Figure 1. Diagram of the free-standing Epitex L760-06AU LED we research here, showing the long leads from the device and the epoxy lens.

LEDs emit light due to the recombination of holes and electrons within a semiconductor p–n junction region. This results partly in optical emission and partly in non-optical emission, where energy is principally lost due to phonon creation (i.e. heat). The percentage of optically emitted power, compared to the total power dissipated, is known as the optical efficiency of the LED. Optical efficiencies decrease significantly with increasing temperature, causing a reduction in emitted optical power. If the drive current of an LED is increased, this increases the heat dissipation, and hence the temperature, particularly in the junction region. The output intensity initially rises linearly with current at low drive levels. However, as the slope efficiency reduces, due to self-heating, the response eventually becomes sub-linear and frequently the intensity output even starts to decrease at higher drive currents. The effective band-gap and the junction barrier potentials also decrease with increasing drive current and temperature, causing a resultant increase in the peak emission wavelength. In order to achieve maximum spectral intensity at a required wavelength, it is therefore necessary to chose optimum values of current drive for a given temperature.

In surface emitting LEDs the major reason for the sub-linear behaviour (reduced slope efficiency with increasing current) is the very important mechanism of self-heating of the diode. This leads to a significant rise in chip and junction temperature at high bias currents, reducing the efficiency of the device. Typical data sheet values of optical energy efficiency (optical power out, divided by electrical power in), for this type of LED, are in the order of 20%. Our chosen LED is constructed within an epoxy lens package, which encapsulates not only the LED, but also its connecting leads and bond-wires (figure 1). The heat produced in the chip can normally only escape via thermal conduction through the thin metallic electrical leads, or via conduction through the epoxy, which is a poor thermal conductor, followed by external cooling by air convection. We will describe in detail below how we have improved the heat flow from the chip by remounting the LED, firstly, to improve conduction paths from the device and then to heat-sink the mounting assembly to conduct heat away more effectively. In addition, we have provided a Peltier cooler, with thermal insulation and a fibre pigtail, to couple out light. We also describe below our experimental arrangement and the extensive measurements we have conducted.

3. Experimental setup

As described above, it is of critical importance that the thermal conductance between the emitting area of the LED and the heat-sink is as high as possible, to reduce the effects of self-heating. With epoxy packaged devices, it is therefore of

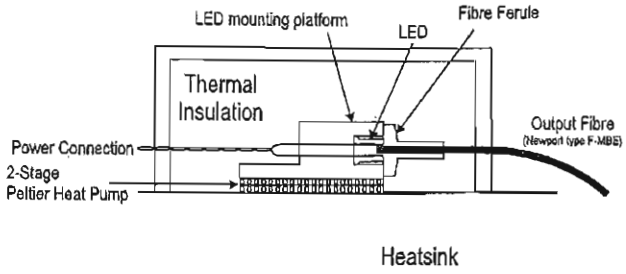

Figure 2. The thermally insulated experimental assembly, consisting of a cooled aluminium LED mounting platform, in close thermal contact with the LED, which was butt-coupled to a 1 mm diameter, 0.37 NA Newport fibre (type: F-MBE). A two-stage Peltier cooler, mounted upon a suitable heat-sink, allows device cooling via the mounting platform.

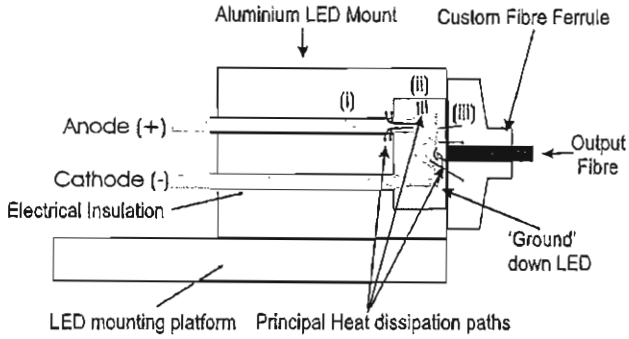

Figure 3. Enlarged version of figure 2, showing the principal conductive paths for heat from the LED. Route (i) is the main means of conducting heat, as this is a steel wire. Routes (ii) and (iii) also form paths for the conduction of heat, which are significantly less effective than (i), as the epoxy is a poor heat conductor.

particular importance to ensure good heat-sinking of the metal anode lead to the LED (on which the LED chip is mounted) since, as we will show, this is the principal heat-dissipation path. The devices used (Epitex L760-06AU, 760 nm LED) have clear moulded epoxy packages, formed into an integral front lensed surface.

To satisfy cooling requirements, a machined aluminium *LED mounting platform* was constructed, as shown in figure 2. The base of this was dimensioned to match the area (9 cm^2) of the top surface of the Peltier cooler. The anode lead of the LED, on which the chip is mounted, was directly bonded using thermally conductive silver-loaded epoxy, in a small bore (1 mm) hole into the heat-sink, being cemented as close as possible to the point where it enters the clear epoxy encapsulation. This silver-loaded epoxy was also electrically conductive, so the cathode lead (which has less effective thermal coupling to the LED chip) had to be electrically insulated from the mounting, this was achieved using small diameter (2 mm) heat-shrink tubing. Light from the LED was launched into a large core diameter fibre (1 mm core diameter, 0.37 NA Newport type: F-MBE) which was held in a ferrule with a 5 mm diameter and a 10 mm diameter flange to bond to the metal face of the LED mounting platform. In order to maximize optical coupling the lensed front of the epoxy LED package was polished away, providing close access to the emitting chip (1 mm spacing from chip) and allowing close butt-coupling to an optical fibre. A two-stage Peltier heat pump was used to provide a practical means of cooling the LED mounting platform.

The heat produced in our packaged LED can escape from the broadened 'anvil' on the small LED anode lead (inside the polymer LED package) through the paths shown by arrows in figure 3. The thermal conductances of these paths are briefly described, and evaluated, below. In order to approximately quantify the conductances of the principal heat-loss paths leading away from this (it is assumed that the LED chip and anvil are in close thermal contact and that the anvil itself is an isothermal body), we start by considering three distinct conductive paths. We first perform estimations of their thermal conductances, assuming simplified geometrical shapes for the component parts, and then add these to obtain an approximate idea of the total conductance. Because of our lack of accurate dimensional information for the internal parts of the LED, we have used various simplifications in our estimations detailed below.

(i) *Provision of close thermal coupling of the anode lead of the device to the metal LED mounting platform to ensure high thermal conductivity.* The steel anode lead to the LED was bonded to the aluminium LED heat-sink platform, close to the point where it enters the epoxy package. Assuming that, at this entry point, this metal lead is well coupled thermally to the LED mounting platform, the thermal impedance between the aluminium mounting platform and the chip is primarily that in a short (2 mm) length of (0.25 mm^2 cross section area) steel lead inside the epoxy package. This steel metal lead section extends inside the epoxy, from the well heat-sunk entry point, where the lead enters the epoxy LED package to the point where it expands into a very much wider, and hence lower thermal conductance, metal 'anvil' on which the LED chip is mounted (we assume that this anvil is isothermal and in good contact with the LED chip for this heat-flow analysis). This 2 mm section of lead is estimated to have a thermal conductance of 7.5×10^{-3} W °C^{-1}.

(ii) *Improvement of thermal contact to the outside of the epoxy LED package by bonding the outer cylindrical surface of the epoxy LED package in a close-fitting hole in the metal heat-sink assembly, using epoxy cement.* This component of the thermal conductance is difficult to analyse without extensive finite-element analysis. However, if we adopt a greatly simplified model, assuming a thermally perfectly conductive sphere, of radius 1 mm, to represent the LED mounting anvil, centred inside a sphere, of radius 3 mm, of epoxy polymer to represent the epoxy package, and assume the outside of this is a perfect heat-sink, we expect a thermal conductance component of approximately 4×10^{-4} W °C^{-1}.

(iii) *Provision of better thermal contact to the front of the package, via the metal ferrule used to mount the output fibre bonded in front of the emitting surface of the chip.* This component of the thermal conductance can again be most easily estimated using a greatly simplified geometry. A cylindrical (1 mm radius) perfectly conductive disc, representing the LED mounting anvil, embedded 2 mm away from an infinite perfectly conductive heat-sinking surface, representing the larger diameter metal ferrule, is assumed. Using this, we estimate a heat-sinking conductance component of 4×10^{-5} W °C^{-1}.

These approximate calculations show that, as we expected, the dominant heat-loss path is through the LED anode lead (i). The total heat-sink conductance has a value of approximately 8×10^{-3} W °C^{-1}. Our choice of greatly simplified models to represent the other conductance paths (ii) and (iii) is justified as even a 100% error in the calculation of these would affect the overall thermal conductance by less than 6%. We would expect that a change in the drive current of 100 mA would cause the thermal power dissipated to increase by approximately 180 mW, with a consequent rise in the temperature of the mounting anvil of approximately 22 °C. Clearly the internal temperature of the LED in the heat-generating junction region may be somewhat higher.

4. Experimental results

We now report on our experimental results. We start with those taken at continuous current and then describe pulsed measurements. As well as providing evidence of the improvements due to cooling, we also show considerable evidence to suggest that spectral changes are predominantly due to thermal changes in the LED, rather than other effects related to injection current level.

4.1. Results under constant continuous current drive (100% duty cycle) conditions

Here we measured the spectral output of the LED under three different heat-loss conditions.

(i) With the LED free-standing, where heat loss is only via leads and via air convection.
(ii) With the LED mounted on its heat-sink platform, as described above, and with the Peltier used to maintain the platform at 20 °C.
(iii) With the LED mounted on its heat-sink platform and where the Peltier device is used to cool and maintain the platform at various selected platform temperatures.

Results under these three conditions are described below.

4.1.1. Results for the 'free-standing' LED with epoxy package in air, without additional heat-sinking. The LED was first operated in its normal package in air, i.e. without any additional heat-sinking. Here, the only heat-loss paths are via the long (2 cm long) uncut anode and cathode leads and via air convection effects to cool the epoxy package itself. These measurements were performed at an ambient air temperature of 20 °C and at drive currents between 25 and 125 mA, in 25 mA increments. The output optical spectra, measured with an ANDO AQ6315A optical spectrum analyser (OSA), are shown in figure 4; these spectral intensities are shown in arbitrary units because the LED was not yet mounted in the heat-sink platform with the fibre pigtail. As may be observed, the peak emission wavelength increased substantially with increasing bias drive current, giving approximately 13 nm peak-wavelength shift when going from 25 to 100 mA. The total power (area under each curve) increased initially in a linear manner with bias current, but then, we believe due to self-heating effects, the slope efficiency reduced at currents above 75 mA and eventually 'rolled over' at 150 mA to give a negative slope efficiency. The specified wavelength, of 760 nm, was achieved at 50 mA drive current.

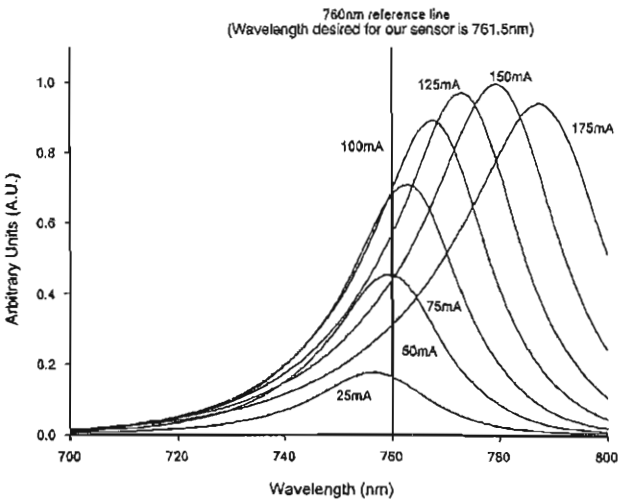

Figure 4. Spectral emission from the 'free-standing' LED, at a laboratory temperature of 20 °C, with continuous drive current of 25, 50, 75, 100, 125, 150 and 175 mA. For this particular configuration, a 760 nm peak emission is achieved at less than 50 mA drive current and a maximum peak spectral intensity output, before roll-off (peak at 770 nm), is achieved at 150 mA. The spectral intensities are shown in arbitrary units as the LED was not yet mounted in the heat-sink platform with the fibre pigtail, so the powers cannot be compared to the other results where the light is output into a fibre.

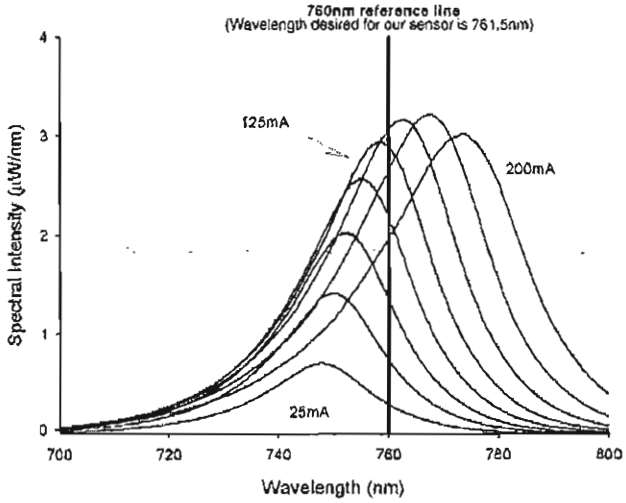

Figure 5. Spectral emission from the mounted LED at a mounting platform temperature of 20 °C, with continuous drive currents of 25, 50, 75, 100, 125, 150, 175 and 200 mA. For this particular configuration, peak emission is achieved at 760 nm with 125 mA drive current and a maximum peak spectral intensity output before roll-off is achieved at 175 mA (peak at 770 nm).

4.1.2. Results with the LED mounted on the heat-sink platform, but with the Peltier device only used to maintain the platform temperature at 20 °C. The performance of the heat-sunk packaged LED was first measured under continuous drive current conditions. The spectral response was measured at a number of different continuous drive current levels (25–200 mA, in 25 mA steps) and the resulting spectra (output fibre connected to the same Ando OSA) are shown in figure 5.

As expected, both the peak wavelength and the power output at this peak wavelength initially increased with drive current. The increase in power is again initially linear with bias current, but the current where the slope efficiency first reduces,

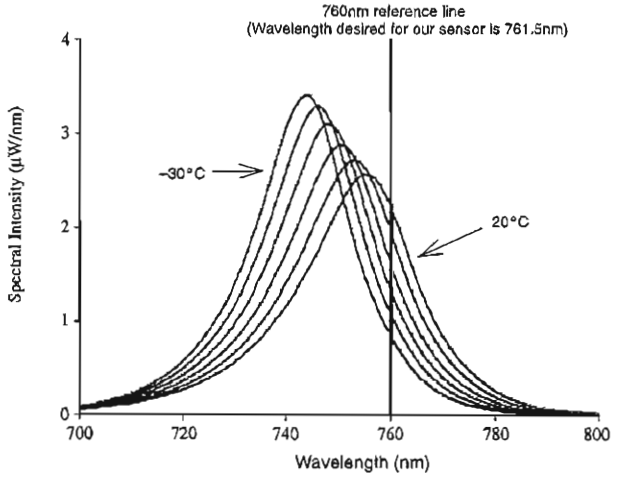

Figure 6. Spectral emission changes, from the mounted and cooled LED, as the mounting platform temperature is lowered from 20 to −30 °C in 10 °C steps, with a continuous drive current of 100 mA.

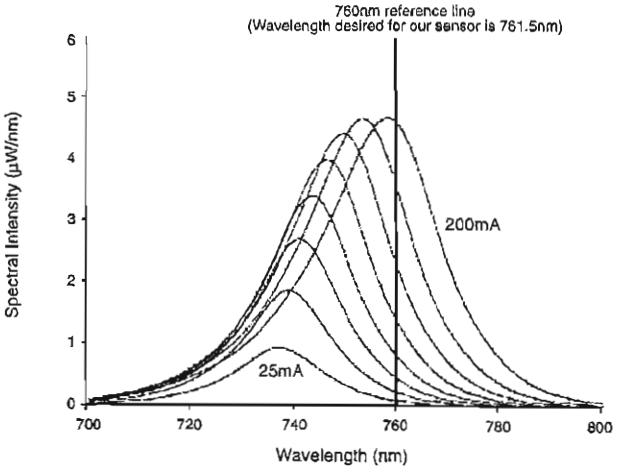

Figure 7. Spectral emission from the mounted and cooled LED at a mounting platform temperature of −30 °C with continuous drive currents of 25, 50, 75, 100, 125, 150, 175 and 200 mA. Now the spectral intensity from the source peaks below 760 nm, even when a continuous drive current as high as 200 mA is applied.

and then goes to zero at the roll over point, is substantially greater in the packaged LED than was the case earlier for the free-standing LED. Above a drive current level of 100 mA, there is clearly no longer a linear increase in power. The peak spectral power finally starts to roll over and then fall when the LED drive current is increased beyond 175 mA (this was 150 mA in the free-standing case).

This is the point where we believe self-heating causes increasing non-radiative transitions, as described above, causing the intensity verses drive current variation to become sub-linear. The specified operating condition for this LED to give a peak output wavelength of 760 nm, when free-standing in air, is with a drive current of 50 mA. We present evidence later to show that spectral changes are due to internal LED temperature changes. We expect that, when the peak spectral output increases beyond 760 nm, the chip temperature will have risen above the manufacturer's normal operating limit.

4.1.3. Spectral effects of mounting the LED on the heat-sink platform with active Peltier cooling. The mounting platform of the packaged LED was cooled to −30 °C, in steps of −10 °C, giving the spectral outputs shown in figure 6. When it was cooled from 20 to −30 °C, the output spectral intensity, at a drive current of 100 mA (the LEDs normal maximum rated current drive), increased from 2.6 to 3.4 μW nm^{-1}, a factor of 1.3. This decrease in temperature resulted in a decrease in peak spectral output wavelength, from 754 nm, at 20 °C, to 744 nm, at −30 °C. This result shows, as expected, that the peak wavelength of the spectral emission from the LED is strongly temperature dependent.

Figure 7 shows the effect of changing drive current when the LED mounting platform was held at −30 °C. Comparing the bias current/spectral characteristics at −30 °C to those at 20 °C, figure 5, shows the strong dependance of the spectrum upon LED platform temperature.

4.1.4. Cooled operation with substantially elevated drive currents. When cooled, the slope efficiency and absolute power output from the LED clearly increases. However, reduced temperature should also allow the LED to be driven at a much higher current without overheating the light emitting region. At a mounting platform temperature of −30 °C, a peak spectral intensity of 5 μW nm^{-1} was attained at 760 nm, using a drive current of 200 mA. Because 760 nm is the peak wavelength under normal operation at room temperature, we believe that, despite significant 'current overdriving', we will still not exceed the manufacturer's maximum active temperature of the LED, provided the spectral peak is still at, or below, 760 nm. Please note again that we will present more evidence below that the peak spectral output is primarily dependent on device temperature. Hence, we believe that it is safe, when cooled, to increase the drive current until the normal peak output wavelength observed at normal room temperature is re-attained.

At a mounting platform temperature of 20 °C, with the LED driven at 125 mA, the peak power obtained was only 2.9 μW nm^{-1} at the peak output wavelength of 760 nm. When the LED mounting platform was cooled to −30 °C, a drive current of above 200 mA was required to shift the peak output to 760 nm. At 200 mA we achieved a peak spectral power output in excess of 5 μW nm^{-1}. The combined action of cooling and then substantially increasing the drive current to re-attain the previous peak spectral wavelength resulted in the power increasing, by a factor of 1.7, at 760 nm. Because we had no fibre pigtail coupling to the LED before it was mounted in the heat-sink platform, we could not compare free-standing and heat-sunk output powers. However, because of the greater current at the power roll-off point when packaged we would expect the LED power output when heat-sunk, to be significantly higher than would be likely for the free-standing device, if it were similarly pigtailed.

4.1.5. Corroboration of the simplified thermal conductance model in section 3. In section 3, we described a simple thermal heat dissipation model to describe loss of heat from the Epitex L760-06AU LED chip and found that a 100 mA rise in drive current would be expected to give a 22 °C rise

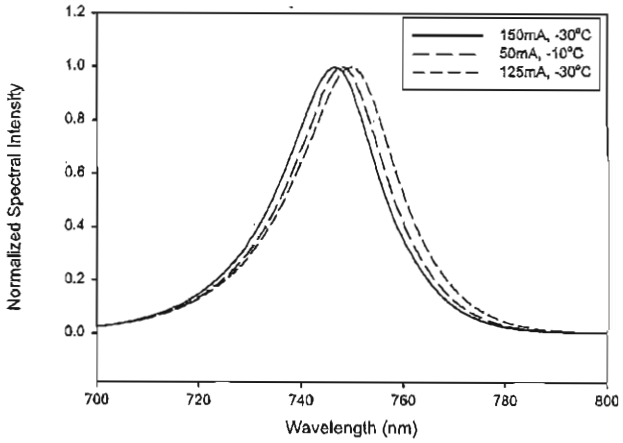

Figure 8. Graph showing normalized (adjusted to give same peak height) optical spectra, at a set of drive currents and platform temperatures chosen to verify the thermal impedance model in section 3. The normalized curve, with a mounting platform temperature of −10 °C and at 50 mA drive current, is shown to give a spectrum lying between curves taken at a mounting platform temperature of −30 °C, with drive currents at 125 and 150 mA. This indicates that our simplified thermal impedance model appears to be predicting approximately the correct temperature rise for the LED mounting anvil.

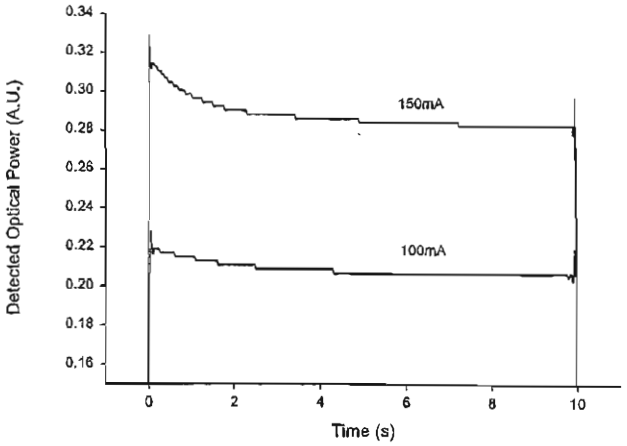

Figure 9. Graph showing the intensity droop with time after an Epitex L760-06AU LED is switched on, at time = 0 s, with peak bias currents of 100 and 150 mA, at an LED mounting platform temperature of 20 °C. This confirms our assertion that a switching frequency of 1 kHz gives a cycle period well below the time constant of this decay.

in the temperature of the LED mounting 'anvil' in the epoxy package. As we wish to show that the output emission spectra is primarily a function of device temperature, we might therefore expect that the spectrum for the LED at 50 mA drive and held at −10 °C might be similar to the same LED being held at −32 °C (22° lower) and being driven at 150 mA (100 mA higher). We had not taken readings at exactly −32 °C, but if we use our results at −30 °C, we should be able to get a rough confirmation of our expected thermal conductance model.

Figure 8 shows that, if we use normalized spectra (multiplied by suitable scalars to give the same peak level), we can compare the curve at a bias current of 50 mA and a mounting platform temperature of −10 °C, with the other measurements taken with the mounting platform temperature at −30 °C and a set of bias currents chosen to be close to 150 mA. We find that the curve at 50 mA and mounting platform temperature −10 °C, lies approximately half way between those at 125 and 150 mA with the mounting platform temperature at −30 °C. This indicates that our simplified thermal impedance model appears to be predicting approximately the correct temperature rise for the LED mounting anvil.

4.2. Room temperature measurements of the pulsed LED, showing the effect of duty cycle

We now investigate how we can reduce effects of self-heating further, using pulsed operation of the LED. This not only allows us to increase the peak current, and hence the peak output power (particularly, see later, if Peltier cooling is also used), but also provides the most convincing evidence that the spectral changes of our LED are primarily due to thermal changes, rather than to any other bias current related effects. We have performed tests at various peak bias currents and operating duty cycles, while monitoring the LED spectral emission throughout. The thermally dissipated power, for a given peak drive current, was reduced to an extent approximately proportional to the fractional duty cycle. The mean electrical input energy, and hence the degree of LED self-heating, was therefore reduced, and the lower operating temperature resulted in increased peak source power. We show there is a dramatic increase in output power possible using optimized cooled LEDs as pulsed light sources.

Before evaluating the effect of driving the LED with a low-duty-cycle pulse train, it was important to evaluate the thermal response time of the LED, to ensure there would be no transient intra-pulse thermal variation that might effect the results. That is, we wished to choose a pulse repetition rate that was sufficiently high to ensure that the temperature of the chip stayed essentially constant during the repetition period of the pulses. The thermal time constant cannot easily be measured directly, but the indirect effects of transient thermal changes could be most readily observed from the optical output when the LED is driven by a step current waveform. As bias current was first applied, self-heating of the LED chip occurred, and its temperature rose, reducing the slope efficiency, but it eventually reached a relatively constant equilibrium state. Figure 9 shows the measured optical output from the LED, when mounted in the heat-sink platform at 20 °C, and driven with current steps of either 0–100 mA, or 0–150 mA, at a switching rate of 50 mHz. It can be seen that the exponential decay to equilibrium has a time constant of approximately 2 s. When, in our sensing system, we eventually drove the LED with a train of short duration pulses, the pulse repetition period of this train was arranged to be much less than the thermal time constant we observed at the start of the longer duration rectangular pulse, hence, ensuring there would be negligible intra-pulse thermal variation when using this faster pulse train. The pulse repetition periods we eventually used were of order 1 ms (1 kHz), keeping the period well below this thermal time constant.

4.2.1. Effect of pulse duty cycle on peak output power, at fixed peak bias current. We now show the effects of reducing duty cycle, while keeping the peak bias current constant. The

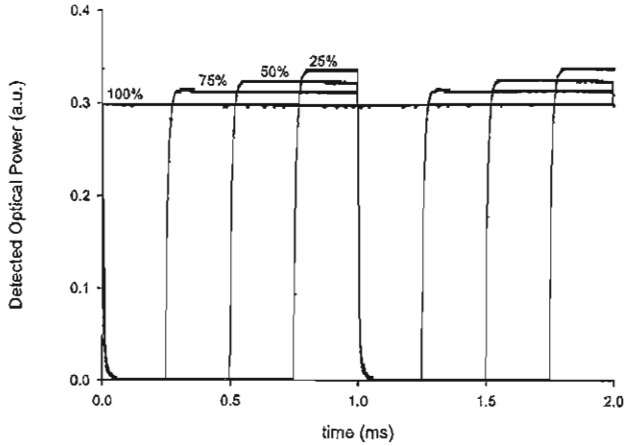

Figure 10. Total power output, from the LED fibre pigtail, with the mounting platform at 20 °C and at a pulse repetition frequency of 1 kHz, measured using a silicon detector. The results are shown as a function of pulse duty cycle. Though the peak drive current was constant at 150 mA, the peak detected power increased with decreasing duty cycle due to a reduction in self-heating.

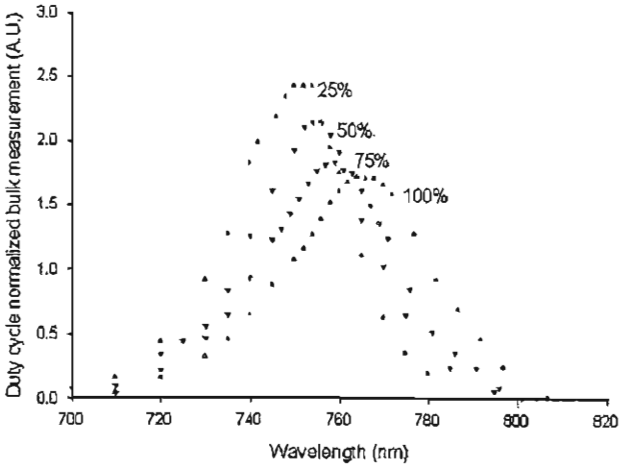

Figure 11. Spectrum of the 1 kHz pulsed LED at 25%, 50%, 75% and 100% duty cycle, measured at 20 °C, with a 150 mA peak bias current. These results show the change in wavelength is solely due to duty cycle changes and therefore is almost certainly as a direct result of falling LED chip temperature.

fibre output of the heat-sink packaged LED source was butt-coupled to a standard lensed silicon diode detector (Centronic BPX65RT), in parallel with a 1 kΩ load, which gave a detection bandwidth of 12 MHz when coupled to an oscilloscope. As the resistor has a low value and the detected voltages are less than 350 mV, this is effectively a photoamperic detection configuration, where the signal voltage is proportional to the optical power on the detector. In figure 10, the detected voltage traces are shown for duty cycles of 25%, 50%, 75% and 100% at a constant peak bias current of 150 mA and at a repetition frequency of 1 kHz. The mounting platform temperature was held at 20 °C for these measurements. It can be clearly seen that the peak power increased as the duty cycle was reduced, even though the peak bias current was unchanged. This shows that the slope efficiency increased at low duty cycles, solely, as a result of lower heat dissipation in the device.

4.2.2. Spectral changes as a result of driving under pulsed conditions. We initially tried to investigate the spectral behaviour under pulsed behaviour using an ANDO type AQ6315A OSA in continuous wave (CW) acquisition mode and appropriately scaling the intensities to compensate for the reduced duty cycle. However, despite the operating manual suggesting this type of OSA should operate acceptably with pulsed sources, we found problems in practice obtaining accurate results. We were unable to ascertain the reason for this, but to avoid the problem our own simpler laboratory OSA arrangement was set up. The light diverging from our fibre-'pigtailed' LED source was coupled to the 1 mm input slit of a Spex dual stage grating monochromator. The resulting near-monochromatic output light was coupled, via a 1 mm output slit, to a silicon-detector optical power meter (Newport 540 optical power meter). The spectral resolution of the spectrometer system was measured using a 633 nm HeNe laser source and found to be 2 nm. As the power meter was calibrated to allow for the responsivity of the silicon-detector head, an absolute output power reading at each wavelength selected on the monochromator could then be logged, to provide spectra. This simplified OSA provided reliable spectral plots under pulsed operation.

A number of spectra have been plotted in figure 11, with the LED package set to 20 °C and with a peak LED drive current of 150 mA. The rise in peak spectral output and fall in peak spectral wavelength with diminishing duty cycle is clearly evident, and this was clearly due to decreasing chip temperature, as the peak current was the same throughout.

4.2.3. Pulsed operation under conditions of approximately constant mean power dissipation, but varying duty cycle. This section compares spectra taken under three very different peak current conditions, but where the duty cycle has been changed to keep the thermal dissipation in the device relatively constant. The three conditions were: 200 mA drive with 25% duty cycle, 100 mA drive with 50% duty cycle, and 50 mA drive with 100% duty cycle, all at 20 °C (i.e. the product of pulse duty cycle and peak bias current was held at a constant value). If the spectrum from the LED were to have a significant dependance on injection current level (as ELEDs often do, due to internal optical gain) then the output spectra would be expected to be very different in these three cases. Conversely, if the spectra were to be solely dependent upon self-heating of the emissive area, and not on the drive current used, then the three spectra should be almost identical. The results from this experiment are shown in figure 12 and, as expected from our hypothesis that spectra are primarily dependent on the temperature of the light emitting region, the spectra are indeed almost identical. Note: the tiny difference that does occur may be because the LED forward voltage increases a little at higher bias currents, hence increasing the heat dissipation. The results shown in figure 12 give the strongest evidence to suggest that the effects of wavelength shift are almost entirely due to chip temperature changes, rather than the possible alternative causes of changes in injection current or internal optical gain.

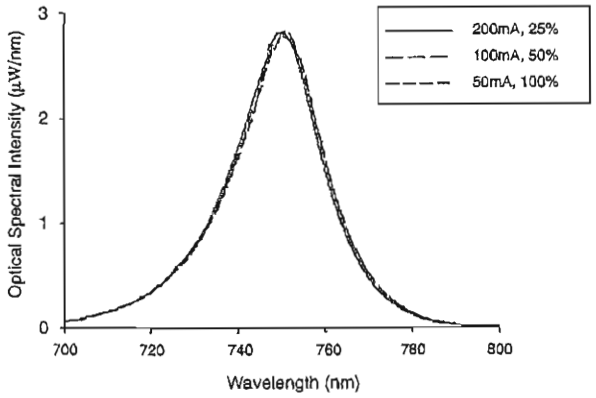

Figure 12. LED output spectra, taken under very different peak current and duty cycle conditions, yet at approximately equivalent mean electrical drive powers. The LED mounting platform temperature was 20 °C and the pulse repetition frequency was 1 kHz.

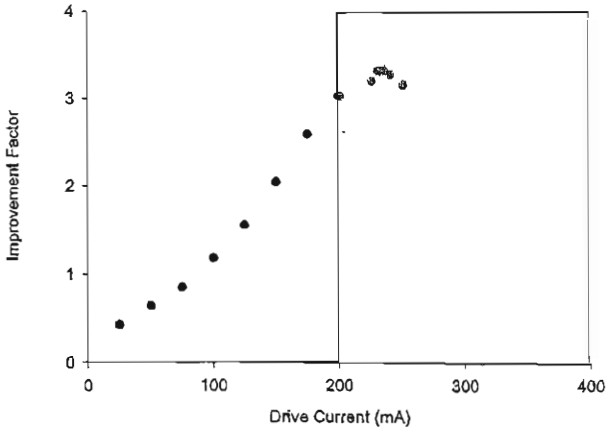

Figure 13. Plot of spectral power at 761.5 nm verses LED drive current, allowing us to determine the optimal 1 kHz pulsed (50% duty cycle) drive current with the LED mounting platform at 20 °C. The shaded area shows where the LED peak spectral wavelength exceeds 760 nm and, consequently, the point at which we believe the LED is being overdriven.

4.3. Brief feasibility investigation of an electrical method for estimating the temperature of an LED junction.

As a possible check on the device chip temperature, obtained by other means, we also briefly attempted to monitor the electrical behaviour of our LEDs, to attempt to derive a measure of the internal junction temperature merely from electrical measurements of the current versus voltage characteristics. To do this, we started by assuming a simple electrical network model for the LED, consisting of an ideal diode with an unknown series resistor, and then found the best-match theoretical curve to our measured V/I curve. Unfortunately, although initially appearing an attractive idea, results from this yielded rather strange and inconsistent values for the junction temperature (often predicting very high temperatures even at low bias currents). In addition, there is the problem that the effects of dynamic thermal changes during the current cycle would also probably be very complex to model in this way. Because of the problems in both the measurement and the analysis, we present no experimental results here, but merely report that the results were not as expected. The reason for this is not fully understood at present, but we report our findings anyway, firstly to maintain good scientific principles, by reporting even negative results, and secondly because of the engineering potential. We hope to carry out more work to investigate this later.

4.4. Practical optimization of LED spectral power output at a wavelength of 761.5 nm, for use in an optical oxygen gas measurement system based on correlation spectroscopy

We now describe the optimization of the heat-sunk packaged LED source for maximization of the spectral output in the band required for measurement of oxygen gas. To accomplish this, the simple laboratory OSA arrangement, as described before, was used to measure power in the spectral region of interest, by setting the monochromator to transmit a 2 nm wide band centred at 761.5 nm. The LED was driven at 1 kHz with 50% duty cycle pulsed drive current. We scaled the resulting spectral powers present at the optical power meter in 'improvement factor' units, i.e. relative to that attained when the LED was driven with normal data sheet values: 100 mA continuous drive current at a mounting platform temperature of 20 °C. This enables a graphical interpretation of our results.

First, we set the LED mounting platform temperature to 20 °C and plotted the output power improvement factor as a function of peak drive current (see figure 13). Initially, as the current was increased, the improvement factor increased super-linearly, primarily due to spectral changes bringing the peak output of the LED towards our required wavelength. However eventually, for currents above 230 mA, the effects of further, now undesirable, wavelength shifts, took the peak spectral output beyond the 761.5 nm wavelength we required, and a final roll-off in slope efficiency also reduced the available spectral intensity at 761.5 nm.

As previously stated, we believe the LED junction area was overheating only when its peak spectral output exceeded 760 nm. We performed spectral measurements to determine that, using our pulsed drive waveform, peak currents above 200 mA would overheat the LED when the LED heat-sink package was held at 20 °C. Therefore, for points falling in the shaded area on figure 13, the peak output wavelength indicates that the temperature of the emitting chip was elevated above that specified in the normal data sheet condition. The maximum 'safe' improvement factor at 20 °C was therefore found to be 3.0 and occurred at a peak drive current of 200 mA.

The highest LED output power was achieved by cooling the device as much as possible. (If we apparently 'over cooled', thereby moving the peak spectral output to much lower wavelengths, we could always increase the bias current yet more, bringing the peak output wavelength higher again to optimize output at this lower heat-sink temperature.) We cooled the LED mounting platform to our practical limit of −30 °C with the Peltier, and again measured the improvement factor at a number of peak drive currents, as plotted in figure 14. This time the maximum improvement factor before overheating (which at −30 °C occurs at a peak drive current of 275 mA) was 4.9. This means, compared to uncooled unpulsed operation, a 4.9 times increase in spectral power within our band of interest is possible using our simple combination of improved heat-sinking and cooling of the LED.

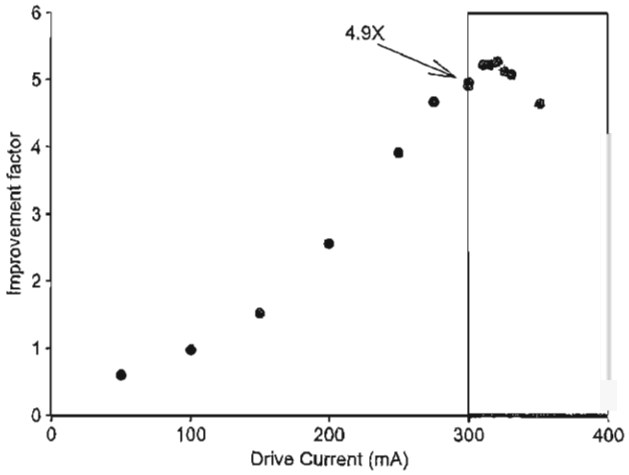

Figure 14. Results showing optimum 1 kHz pulsed (50% duty cycle) drive current for best output at 761.5 nm with the LED mounting platform held at −30 °C. A 4.9 fold increase is possible in comparison to operation at 20 °C and 100 mA pulsed (50% duty cycle). The shaded area shows where the LED peak spectral wavelength exceeds 760 nm and where we believe the LED is first starting to be overdriven.

5. Conclusions

We have proposed and evaluated in detail a simple method for increasing the spectral power intensity available from a near-infrared LED. The power increases that may be obtained from cooling the LED, pulsing it, increasing bias current, and from combinations of all these factors, have been investigated. We have also shown that by reducing pulse duty cycle the peak output wavelength reduces significantly as a result of reducing chip drive current and temperature. We have found considerable evidence to show that, for our selected surface emitting LED, these spectral changes are related solely to chip temperature, rather than to other effects such as absolute bias current level or possible related effects, such as optical gain in the device. The most convincing evidence for this is obtained from our pulsed measurements, where we have reduced the duty cycle and increased the drive current, yet kept the time-averaged total power approximately constant. Although the peak current changed in this measurement by a factor of 4, the spectrum remained essentially the same. We have shown the potential improvements available for use with various spectroscopic gas detection systems, including our own system for oxygen sensing based on correlation spectroscopy. The useful power improvement factors we have achieved are by

(i) improving the heat-sinking of the device,
(ii) pulsing it at a lower duty cycle (we actually used a 50% duty cycle, as required for our sensor application),
(iii) cooling to low temperatures,
(iv) increasing the drive current, taking advantage of the lower initial chip temperature.

By taking all these factors into account, overall peak power was increased by a factor of 4.9, by improving the heat-sinking, using a convenient package, pulsing at the 50% duty cycle required for our sensor application, cooling the LED mounting platform to −30 °C with the Peltier cooler, and then increasing the peak bias current to the optimum level under these new conditions, without overheating the light emitting region of the chip. To ensure no overheating, a limit on the level of current was set to the level where the peak output spectral wavelength matched that at the normal data sheet operating limit. A factor of nearly 5 times for the improvement in output power is very significant, and might take many years of component advances to achieve by improving the LED device structure. We expect that even better improvements could be achieved by packaging the device in an evacuated heat-sink can, closely coupled thermally to an integral Peltier cooler, and then providing a hermetically sealed fibre pigtail for light output.

We are now setting up lifetime tests on cooled current-overdriven LEDs, to show the devices survive well in practice (as we would expect from prior background knowledge that LED degradation tends to generally occur due to overheating effects). Initial tests so far have shown no significant degradation over medium periods, even when we deliberately overdrove an uncooled device to try to observe degradation, so perhaps the devices we selected are too conservatively specified anyway. However, just overdriving without cooling does not result in significant power gain in any case, so all our experiments to increase power still yield valuable benefits.

Although this detailed work was done on a specific type of near-infrared LED, the results obtained are likely to be applicable to a wide range of similar devices. Factors such as these should enable optical sensing and other systems to achieve substantially higher sensitivity by virtue of significantly increasing the optical drive signal and hence improving the signal to noise ratio.

Acknowledgments

The authors wish to express their appreciation to the Engineering and Physical Sciences Research Council (EPSRC) for funding the research undertaken in this project, as well as the following industrial sponsors involved in the EPSRC's Faraday/INTErSECT research initiative: Accurate Controls Ltd, BOC Edwards, Corus, Health and Safety Laboratories, Kidde plc, National Grid and National Physical Laboratories. In addition, the provision of complimentary 760 nm LEDs from Epitex Inc. is gratefully acknowledged. One of the authors (PC) wishes to thank EPSRC for a PhD student research grant.

References

[1] Mueller E K, Lee S M, Van de Workeen B C and Mueller O M 2001 *Proc. SPIE* **4285** 23–32
[2] Petroski J 2002 Thermal challenges facing new generation light emitting diodes (LEDs) for lighting applications *Solid State Lighting II* (*Proc. SPIE* vol 4776) (Bellingham, WA: SPIE Optical Engineering Press) pp 215–22
[3] Burrus C A and Miller B I 1971 Small-area, double-heterostructure aluminium–gallium arsenide electroluminescent diode sources for optical-fiber transmission lines *Opt. Commun.* **4** 307–9
[4] Dakin J P, Gunning M J, Chambers P and Xin Z J 2003 Detection of gases by correlation spectroscopy *Sensors Actuators* B **90** 124–31
[5] Senior J 1992 *Optical Fiber Communications* (Englewood Cliffs, NJ: Prentice Hall)
[6] Streubel K 2004 LED sources *Handbook of Optoelectronics* ed J P Dakin (Bristol: Institute of Physics Publishing)
[7] Bergh A A and Dean P J 1976 *Light-Emitting Diodes* (Oxford: Clarendon)

Appendix B

Publications that have Resulted from this Work

B.1 Journal Papers

1. P. Chambers, E. A. D. Austin and J. P. Dakin, Theoretical analysis of a methane gas detection system, using the complementary source modulation method of correlation spectroscopy, Measurement Science Technology, 15(8), 1629-1636, 2004.

2. P. Chambers, E. A. D. Austin, M. J. Gunning and J. P. Dakin, Investigation of the peak power enhancement available from a surface emitting GaAlAs near-infrared light emitting diode by cooling and pulsing, Measurement Science Technology, 14(11):2006-2014, 2003.

3. J.P. Dakin, M.J. Gunning, P. Chambers and Z. J. Xin, Detection of gases by correlation spectroscopy, Sensors & Actuators B, 90:124-131, 2003.

B.2 Book Chapters

1. J. P. Dakin and P. Chambers, Review of methods of optical gas detection by direct optical spectroscopy with emphasis on correlation spectroscopy, to be published as a chapter in the proceedings of the ASCOS 2004 summer school.

B.3 Conference Papers

1. P. Chambers, E. A. D. Austin and J. P. Dakin, Predictions of the response of optical gas sensing systems using correlation spectroscopy, Photon 04, Glasgow, Sep 2004.

2. P. Chambers, E. A. D. Austin and J. P. Dakin, Theoretical analysis of a CO_2 gas detection system using correlation spectroscopy, Second European Workshop on Optical Fiber Sensors (EWOFS 04), Santander, 9-11 Jun 2004.

3. E. A. D. Austin, P. Chambers and J. P. Dakin, Experimental sensing of CO_2 and CH_4 gases using the CoSM correlation spectroscopy method and comparison with simulated predictions from the Hitran database, Europt(R)ode VII, Madrid, 4-7 April 2004.

4. P. Chambers, E. A. D. Austin and J. P. Dakin, Predicted response of optical gas sensing systems using correlation spectroscopy for combustion monitoring, On-line Measurements for Quality in the Metals Industries, London, 7-8 Oct 2003.

5. P. Chambers, E. A. D. Austin and J. P. Dakin, Theoretical modelling studies of gas sensing systems using correlation spectroscopy, Photonics East 2003, Rhode Island, 27-31 Oct 2003.

6. P. Chambers, E. A. D. Austin and J. P. Dakin, Model to predict the response of correlation spectroscopy gas detection systems for CH_4, OFS-16, Nara, Japan, 13-17 Oct 2003.

7. P. Chambers, E. A. D. Austin and J. P. Dakin, Model to predict the response of a correlation spectroscopy system for the detection of oxygen gas, Sensors and Their Applications XII, Limerick, 2-4 Sept 2003.

8. J. P. Dakin, M. J. Gunning, P. Chambers, and E. A. D. Austin, Fibre optic LED-based correlation spectroscopy for O_2 detection, OFS 2002 Portland, Oregon 6-10 May 2002. (Postdeadline)

9. J. P. Dakin, M. J. Gunning and P. Chambers, Detection of gases and gas mixtures by correlation spectroscopy, Europt(R)ode VI Manchester, 7-10 Apr 2002.

Bibliography

[1] D. Kohl. Function and applications of gas sensors. *Journal of Physics D: Applied Physics*, 34:R125–R149, 2001.

[2] P. T. Mosely. Solid state gas sensors. *Measurement Science Technology*, 8(3):223–237, 1997.

[3] M. G. Allen. Diode laser absorption sensors for gas-dynamic and combustion flows. *Measurement Science Technology*, 9(4):545–562, 1998.

[4] T. Iseki, H. Tai, and K. Kimura. A portable remote methane sensor using a tunable diode laser. *Measurement Science Technology*, 11(6):594–602, 2000.

[5] S. Svanberg. Geophysical gas monitoring using optical techniques: volcanoes, geothermal fields and mines. *Optics and Lasers in Engineering*, 37(2–3):245–266, 2002.

[6] D. W. Hill and T. Powell. *Non-Dispersive Infra-Red Gas Analysis in Science, Medicine and Industry.* Adam Hilget Ltd., 1968.

[7] M. L. Veingerov. Eine methode der gasanalyze beruhend auf dem optisch-akustischen Tyndall-Röntgeneffekt. *Dokl. Akad. Nauk SSSR.*, 19:687, 1938.

[8] K. F. Luft. Anwendung des ultraroten spektrums in der chemischen industrie. *Angew. Chem.*, 19(B):2, 1947.

[9] R. Goody. Cross-correlating spectrometer. *Journal of the Optical Society of America*, 58(7):900–908, 1968.

[10] F. W. Taylor, J. T. Haughton, G. D. Peskett, C. D. Rogers, and E. J. Williamson. Radiometer for remote sounding of the upper atmosphere. *Applied Optics*, 11(1):135–141, 1972.

[11] H. O. Edwards and J. P. Dakin. Gas sensors using correlation spectroscopy compatible with fibre-optic operation. *Sensors & actuators B: Chemical*, 11:9, 1993.

[12] P. C. Hills, P. J. Samson, and I. Webster. Optical fibres are intrinsically safe: reviewing the myth. *Australian Journal of Electrical and Electronics Engineering*, 10(3):207–220, 1993. ISSN:0725-2986.

[13] D. K. Zhang, P. C. Hills, C. Zheng, T. F. Wall, and P. Samson. Fibre optic ignition of combustible gas mixtures by the radiative heating of small particles. In *Proceedings of the 24th International Symposium on Combustion (code 19626)*, pages 1761–1767, Pittsburgh, PA, USA, 1992. ISSN:0082-0784.

[14] H. Inaba, T. Kobayasi, M. Hirama, and M. Hamza. Optical-fibre network system for air polution monitoring over a wide area by optical absorption method. *Electronics Letters*, 15(23):749–751, 1979.

[15] B. Culshaw, G. Stewart, F. Dong, C. Tandy, and D. Moodie. Fibre optic techniques for remote spectroscopic methane detection from concept to system realisation. *Sensors & Actuators B: Chemical*, 51:25–37, 1998.

[16] G. Stewart, P. Shields, and B. Culshaw. Development of fibre laser systems for ring-down and intracavity gas spectroscopy in the near-IR. *Measurement Science Technology*, 15:16211628, 2004.

[17] G. Whitenett, G. Stewart, H. Yu, and B. Culshaw. Investigation of a tuneable mode-locked fiber laser for application to multipoint gas spectroscopy. *Journal of Lightwave Technology*, 22(3):813–819, 2004.

[18] T. Kobayashi, M. Hirana, and H. Inaba. Remote monitoring of NO_2 molecules by differential absorption using optical fibre link. *Applied Optics*, 20(19):3279, 1981.

[19] A. Hordvik, A. Berg, and D. Thingbø. A fibre optic gas detection system. In *proceedings 9th international conference on Optical Communications, 'ECOC 83'*, page 317, 1983.

[20] S. Stueflotten, T. Christensen, S. Iversen, J. O. Hellvik, K. Almås, T. Wien, and A. Graav. An infrared fibre optic gas detection system. In *proceedings OFS-2 international conference*, pages 87–90, 1982.

[21] P. J. Samson and A. D. Stuart. Fibre optic gas sensing using Raman spectroscopy. In *Proceedings of 14th Australian conference on optical fibre technology*, pages 145–148, 1989.

[22] J. P. Dakin, C. A. Wade, D. Pinchbeck, and J. S. Wykes. A novel optical fibre methane system. In *SPIE volume: 734 Fibre Optics '87: Fifth Internation Conference on Fibre Optics and Optoelectronics*, 1987.

[23] A. Mohebati and T. A. King. Remote detection of gases by diode laser spectroscopy. *Journal of Modern Optics*, 35(3):319–324, 1988.

[24] M. B. Sinclair, M. A. Butler, S. H. Kravitz, W. J. Zubrzycki, and A. J. Ricco. Synthetic infrared spectra. *Optics Letters*, 22(13):1036–1038, 1997.

[25] M. B. Sinclair, M. A. Butler, A. J. Ricco, and S. D. Senturia. Synthetic spectra: A tool for correlation spectroscopy. *Applied Optics*, 36(15):3342–3348, 1997.

[26] W. F. Herget, J. A. Jahnke, D. E. Burch, and D. A. Gryvnak. Infrared gas-filter correlation instrument for in situ measurement of gaseous pollutant concentrations. *Applied Optics*, 5:1222–1228, 1976.

[27] A. Cheung, W. Johnstone, and D. Moodie. Detection of acetylene gas using optical correlation spectroscopy. In *Proceedings OFS-17 international conference*, 2005.

[28] Tml-20 datasheet, CO_2 gas filter correlation instrument. *http://www.teledyne-ml.com/pdf/co2.pdf.*

[29] C. N. Banwell and E. M. McCash. *Fundamentals of Molecular Spectroscopy: 4th Ed.* McGraw-Hill, London. ISBN:0-07-707976-0.

[30] J. M. Hollas. *High Resolution Spectroscopy: 2nd Ed.* Wiley, England. ISBN:0-471-97421-8.

[31] L. S. Rothman, A. Barbe, D. C. Benner, L. R. Brown, C. Camy-Peyret, M. R. Carleer, K. Chance, C. Clerbaux, V. Dana, V. M. Devi, A. Fayt, J.-M. Flaud, R. R. Gamache, A. Goldman, D. Jacquemart, K. W. Jucks, W. J. Lafferty, J.-Y. Mandin, S. T. Massie, V. Nemtchinov, D. A. Newnham, A. Perrin, C. P. Rinsland, J. Schroeder, K. M. Smith, M. A. H. Smith, K. Tang, R. A. Toth, J. V. Auwera, P. Varanasi, and K. Yoshino. The HITRAN molecular spectroscopic database: edition of 2000 including updates through 2001. *Journal of Quantitative Spectroscopy and Radiative Transfer*, 82, 2003.

[32] J. Y. Mandin. Interpretation of the CO_2 absorption bands observed in the venus infrared spectrum between 1 and 2.5 μm. *Journal of Molecular Spectroscopy*, 67:304–321, 1977.

[33] L. S. Rothman, R. L. Hawkins, R. B. Wattson, and R. R. Gamache. Energy levels, intensities, and linewidths of atmospheric carbon dioxide bands. *Journal of Quantitative Spectroscopy and Radiative Transfer*, 48:537–566, 1992.

[34] M. B. E. Aguir, M. Y. Perrin, and J. Taine. Variational calculation of energies of highly excited rovibrational states of $^{12}C_{16}O_2$. *Journal of Molecular Spectroscopy*, 215:234–243, 2002.

[35] S. A. Tashkun, V. I. Perevalov, J. L. Teffo, A. D. Bykov, and N. N. Lavrentieva. CDSD-296, The carbon dioxide spectroscopic databank: version for atmospheric applications. In *XIV Symposium on High Resolution Molecular Spectroscopy*, 2003. Information at: ftp://ftp.iao.ru/pub/CDSD-296/.

[36] L. S. Rothman, D. Jacquemart, A. Barbe, D. Chris Benner, M. Birk, L. R. Brown, M. R. Carleer, C. Chackerian (Jr.), K. Chance, V. Dana, V. M. Devi, J.-M. Flaud, R. R. Gamache, A. Goldman, J.-M. Hartmann, K. W. Jucks, A. G. Maki, J.-Y. Mandin, S. T. Massie, J. Orphal, A. Perrin, C. P. Rinsland, M. A. H. Smith,

J. Tennyson, R. N. Tolchenov, R. A. Toth, J. Vander Auwera, P. Varanasi, and G. Wagner. The HITRAN 2004 molecular spectroscopic database. *Journal of Quantitative Spectroscopy and Radiative Transfer*, in press, 2005.

[37] S. Weart. *The Carbon Dioxide Greenhouse Effect.* 2004. http://www.aip.org/history/climate/co2.htm.

[38] G. Eppeldauer and J. E. Hardis. Fourteen-decade photocurrent measurements with large-area silicon photodiodes at room temperature. *Applied Optics*, 30(22):3091–3099, 1991.

[39] Definitions, formulae and constants relating to the humidity of the air. *British Standard 1339*, 1965.

[40] D. E. Burch and D. A. Gryvnak. *Cross-stack measurement of pollutant concentrations using gas-cell correlation spectroscopy*, pages 193–231. 1974.

[41] L. R. Brown, J. S. Margolis, J. P. Champion, J. C. Hilico, J. M. Jouvard, M. Loete, C. Chackerian, G. Tarrago, and D. C. Benner. Methane and its isotopescurrent status and prospects for improvement. *Journal of Quantitative Spectroscopy and Radiative Transfer*, 48:617–628, 1992.

[42] L. R. Brown, D. C. Benner, J.-P. Champion, V. M. Devi, L. Fejard, R. R. Gamache, T. Gabard, J. C. Hilico, B. Lavorel, M. Loëte, G. Ch. Mellau, A. Nikitin, A. S. Pine, A. Predoi-Cross, C. P. Rinsland, O. Robert, R. L. Sams, M. A. H. Smith, S. A. Tashkun, and Vl. G. Tyuterev. Methane line parameters in HITRAN. *Journal of Quantitative Spectroscopy and Radiative Transfer*, 82:219–238, 2003.

[43] L. R. Brown and C. Plymate. Experimental line parameters of the oxygen A band at 760nm. *Journal of Quantitative Spectroscopy and Radiative Transfer*, 199:166–179, 2000.

[44] G. Best and O. M. Sezerman. Shedding light on hybrid optics: A tutorial in coupling. *Optics & Photonics News*, pages 32–34, February 1999.

[45] A. V. Oppenheim, R. W. Schafer, and J. R. Back. *Discrete-time Digital Signal Processing.* Prentice Hall International, England, 1999.

[46] M. Tur, E. Shafir, and K. Blotekjaer. Source-induced noise in optical systems driven by low coherence sources. *Journal of Lightwave Technology*, 8:183–189, 1990.